University of Alberta

Ground State Properties of Pure and Doped Quantum Clusters

by

Javier Cuervo

A thesis submitted to the Faculty of Graduate Studies and Research in partial fulfillment of the requirements for the degree of **Doctor of Philosophy**.

Department of Chemistry

Edmonton, Alberta
Fall 2008

Library and
Archives Canada

Published Heritage
Branch

395 Wellington Street
Ottawa ON K1A 0N4
Canada

Bibliothèque et
Archives Canada

Direction du
Patrimoine de l'édition

395, rue Wellington
Ottawa ON K1A 0N4
Canada

Your file Votre référence
ISBN: 978-0-494-46302-4
Our file Notre référence
ISBN: 978-0-494-46302-4

NOTICE:
The author has granted a non-exclusive license allowing Library and Archives Canada to reproduce, publish, archive, preserve, conserve, communicate to the public by telecommunication or on the Internet, loan, distribute and sell theses worldwide, for commercial or non-commercial purposes, in microform, paper, electronic and/or any other formats.

The author retains copyright ownership and moral rights in this thesis. Neither the thesis nor substantial extracts from it may be printed or otherwise reproduced without the author's permission.

AVIS:
L'auteur a accordé une licence non exclusive permettant à la Bibliothèque et Archives Canada de reproduire, publier, archiver, sauvegarder, conserver, transmettre au public par télécommunication ou par l'Internet, prêter, distribuer et vendre des thèses partout dans le monde, à des fins commerciales ou autres, sur support microforme, papier, électronique et/ou autres formats.

L'auteur conserve la propriété du droit d'auteur et des droits moraux qui protège cette thèse. Ni la thèse ni des extraits substantiels de celle-ci ne doivent être imprimés ou autrement reproduits sans son autorisation.

In compliance with the Canadian Privacy Act some supporting forms may have been removed from this thesis.

While these forms may be included in the document page count, their removal does not represent any loss of content from the thesis.

Conformément à la loi canadienne sur la protection de la vie privée, quelques formulaires secondaires ont été enlevés de cette thèse.

Bien que ces formulaires aient inclus dans la pagination, il n'y aura aucun contenu manquant.

Canada

Abstract

This thesis presents the study of pristine and binary mixtures of clusters composed of *para*H_2 and *ortho*D_2. We have characterized these systems in terms of their energetics, structure and imaginary time dynamics by means of the path integral ground state Monte Carlo method. We have found that the chemical potential of these systems display a rich behaviour as a function of their size. This clusters also display a shell structure loosely based on Mackay and anti-Mackay moieties, along with size-driven structural transitions and coexistence of structures even in their ground state. The solid- and/or liquid-like character of these systems was scrutinized and it was determined that at certain sizes, clusters change from a liquid-like phase to a more rigid phase based on the so-called Lindemann criterion. We observed that different environments can promote different structures in weakly bound systems embedded in hydrogen clusters. In the particular case of $(ortho\mathrm{D}_2)_3$, depending on the number of hydrogen molecules surrounding the heavy isotope, two different structural configurations can be observed: for most of the clusters, the equilateral conformation is preferred, while in the case of N=29,37, the isosceles structure is favoured. The imaginary time dynamics of these systems was probed using imaginary-time correlation functions. We explore approaches to obtain rate constants through the multiexponential fit of the side-side imaginary time correlation function along a suitable reaction coordinate. In particular we studied the structural transformation of $(ortho\mathrm{D}_2)_3$ embedded in a small *para*H_2 cluster. This work has enhanced our knowledge of the size evolution of different physical properties of weakly bound quantum clusters.

Acknowledgements

I want to express my enormous gratitude to my supervisor, Prof. Pierre-Nicholas Roy, who with his guidance, help, patience and enthusiasm has made research for me as exciting as it could ever be. I am also very grateful to my co-supervisor Prof. Massimo Boninsegni. Thank to his timely advice and support I have had the opportunity to pursue my Doctoral degree at the University of Alberta. Special thanks go to Dr. Nicholas Blinov for his help and many stimulating discussions. I also wish to thank Dr. Anna Jordan for her support and mentoring as my teaching supervisor. I would also like to thank all the past and present members of the Roy and Boninsegni groups: (in alphabetical order) Dr. Norberto Castillo, Dr. Robert Ganzynkowicz, Kyle Green, Yoonjung Huh, Dr. Bilkiss Issack, Long Dinh Dang, Dr. Yong Dong Liu, Yuan Ma, Paul Moffat, Dr. Fabio Mezzacapo, Mikyung Seo, Joseph Turnbull, Yalina Tritzant and Stephanie Wong. They have made work an enjoyable experience. I wish to thank all my friends in Edmonton. Life outside, and inside, the lab has been so much fun and rewarding thanks to them. I am deeply grateful to my family for all their support and encouragement: Papá, Mamá, Jorge, Marié, José, Abuela Mary y Abuelo Jorge (RIP). Finally, I would like to thank Vanessa for her daily support and caring in every enterprise that we have embraced together.

Table of Contents

1 Introduction **1**

1.1 Context 1

1.2 Some Quantum Mechanical Concepts 9

1.2.1 The Schrödinger equation and the Born-Oppenheimer approximation 10

1.3 Path Integrals and Monte Carlo Methods 14

1.3.1 Path Integral Ground State (PIGS) 14

1.3.2 Imaginary-time Propagator 16

1.3.3 Monte Carlo Integration 17

1.4 Overview and organization of the thesis 18

2 Path integral ground state: Applications to small hydrogen clusters **19**

2.1 Introduction 20

2.2 paraHydrogen clusters 21

2.3 Results and discussion 22

2.3.1 Energetics 22

2.3.2 Structural properties 27

2.4 Conclusions 34

3 Rigid-liquid behavior of pure quantum clusters **35**

3.1 Introduction 36

3.2 Methodology 37

3.3 Results and Discussion 37

3.3.1 Energetics 37
3.3.2 Structure 43
3.4 Conclusions 58

4 Structure, energetics, and isomer coexistence in mixed quantum clusters **59**
4.1 Introduction 59
4.2 Methodology 61
4.3 Results and Discussion 62
4.3.1 Structure 64
4.3.2 Stabilization of isomers 77
4.4 Conclusions 80

5 Imaginary-time dynamics of quantum clusters **82**
5.1 Introduction 82
5.2 Theory and methodology 85
5.2.1 Reaction rates 85
5.3 Results and discussion 86
5.3.1 Reaction rates 89
5.4 Conclusions 94

6 Conclusions **95**
6.1 Future Directions 97
6.1.1 Mixed Helium-Hydrogen Clusters 97
6.1.2 Ammonia embedded in Helium clusters 99

List of Figures

1.1 Icosahedral structures: 13 particles icosahedron (a), 19 particles anti-Mackay icosaheron (b), 55 particles Mackay icosahedron (c), 23 particles anti-Mackay icosahedron (d). 4

2.1 (Upper panel) Total energy per H_2 molecule ($e(\tau)$) (in K) as a function time step τ (in K^{-1}). The total projection time is $\beta = 1$ K^{-1} . The calculations were carried out for four particles using the Silvera-Goldman potential (Ref. [75]) . The dashed line is the quartic fit to the PIGS data. (Bottom panel)Total energy per H_2 molecule ($e(\beta)$) (in K) as a function of projection time β (in K^{-1}). The time step used in all calculations is $\tau = 0.0066$ K^{-1} . The calculations are for the same system as in (a). The dashed line is a fit to the PIGS data based on the expression: $e(\beta) = a + b\exp(-c\beta)$. Error bars are within the size of the symbols. 24

2.2 Chemical potential (μ) as a function of N using Silvera-Goldman potential (Ref. [75]) (diamonds) and Buck potential (Ref. [76]) (filled circles). Error bars are within the size of the symbols. 26

2.3 Density profiles of various $(para H_2)_N$ clusters obtained from PIGS and the Silvera-Goldman potential (Ref. [75]). The solid, dotted, and dashed lines correspond respectively to: N = 3, 4, 5 (a); N= 6, 7, 8 (b); N= 9, 10, 11 (c); N= 12, 13, 14 (d); N=15, 16, 17 (e); N=18, 19, 20 (f). 30

2.4 Pair distribution function of *para*H_2 clusters calculated using PIGS and the Silvera-Goldman potential (Ref. [75]). The solid, dotted, dashed and dotted-dashed lines correspond respectively to N= 3,7,13,20. The normalization is $4\pi \int_0^\infty g(r)r^2 dr = (N-1)$. 31

2.5 One particle distribution function in Pekeris coordinates of *para*H_2 clusters calculated using DVR and PIGS. DVR: filled circles denotes N=3. PIGS: Solid, dotted, dashed and dotted-dashed lines correspond respectively to N= 3,7,10,20. 33

3.1 Difference in the energy per particle of *para*Hydrogen clusters (Δe) (in K) defined as the results of this work minus those of Ref. [47] as a function of N using Buck potential (filled circles) (Ref. [76]) and Silvera-Goldman potential (squares) (Ref. [75]). When not shown, error bars are within the size of the symbols. Solid lines are only guides to the eye. 40

3.2 Chemical potential (μ) as a function of N of *para*Hydrogen clusters (filled circles) using Buck potential (a) (Ref. [76]) and Silvera-Goldman potential (b) (Ref. [75]). Results from Guardiola and Navarro (Ref. [47]) (squares) are also shown. When not shown, error bars are within the size of the symbols. Solid lines are only guides to the eye. 41

3.3 Chemical potential (μ) as a function of N of *ortho*Deuterium clusters using Buck potential (Ref. [76]) (filled circles) and Silvera-Goldman potential (Ref. [75]) (squares). When not shown, error bars are within the size of the symbols. Solid lines are only guides to the eye. 42

3.4 Density profile of (*para*H_2)$_N$ (solid line) and (*ortho*D_2)$_N$ (dotted line), N =13 (a), 19 (b), 23 (c), 26 (d), 28 (e), 29 (f), 33 (g), 34 (h), 38 (i), 39(j) 41(k), 55(l). 51

3.5 Specific (δ_L) (filled circles) and generic (δ_{L^2}) (squares) relative root mean square bond-length fluctuations as a function of N for (*para*H_2)$_N$ (a) and (*ortho*D_2)$_N$ (b). 53

3.6 Specific (δ_{rcm}) (filled circles) and generic (δ_{rcm^g}) (squares) relative root mean square distance to the centre-of-mass fluctuations as a function of N for $(para\mathrm{H}_2)_N$ (a) and $(ortho\mathrm{D}_2)_N$ (b). 54

3.7 Bond order parameters Q_4 (a) and Q_6 (b) as a function of the number of particles N for $para\mathrm{H}_2$ (filled circles) and $ortho\mathrm{D}_2$ (squares). . . . 57

4.1 Chemical potential (μ) as a function of cluster size of $(para\mathrm{H}_2)_N(ortho\mathrm{D}_2)_3$ clusters using Buck potential (filled circles) (Ref. [76]) and Silvera-Goldman potential (squares) (Ref. [75]). When not shown, error bars are within the size of the symbols. Solid lines are only guides to the eye. 64

4.2 Density profile of $(ortho\mathrm{D}_2)$ (solid line) and $(para\mathrm{H}_2)$ (dotted line), in $(para\mathrm{H}_2)_N(ortho\mathrm{D}_2)_3$ clusters N+3=13 (a), 19 (b), 23 (c), 25 (d), 29 (e), 34 (f), 37 (g), 39 (h). 69

4.3 Deuterium-fixed frame. 71

4.4 Pekeris distribution function of $(ortho\mathrm{D}_2)_3$ in some $(para\mathrm{H}_2)_N(ortho\mathrm{D}_2)_3$ clusters. 73

4.5 Density isosurfaces of $(para\mathrm{H}_2)_N(ortho\mathrm{D}_2)_3$ clusters of $N+3=13$ (a), 19 (b), 23 (c), 25 (d), 29 (e) and 37 (f). Pictures generated with VMD.[114] 76

4.6 Negative of the natural logarithm of the reaction coordinate distribution function for some $(para\mathrm{H}_2)_N(ortho\mathrm{D}_2)_3$ clusters. 79

5.1 Average pair distance imaginary-time autocorrelation function of $(para\mathrm{H}_2)_3$. 88

5.2 Linearization of the long time tail of the imaginary-time correlation function. Statistical errors of the data are within the size of the symbol 90

5.3 Pekeris distribution functions of $(ortho\mathrm{D}_2)_3(para\mathrm{H}_2)_8$ (PIGS) and the bound states of $(ortho\mathrm{D}_2)_3$ (DVR). 91

5.4 Side-Side imaginary-time correlation function along the asymmetry factor of $(ortho\mathrm{D}_2)_3(para\mathrm{H}_2)_8$ 93

6.1 Umbrella inversion of ammonia. 99

List of Tables

2.1 Ground state energies per molecule ($e(N)$) (in K) of small *para*H_2 clusters obtained for the Silvera-Goldman potential (*a*) (Ref. [75]) and Buck potential (*b*) (Reference [76]) using PIGS. DVR results for the dimer and trimer are also shown. VMC results for n=2,3,4,5 are taken from Ref. [26], VMC and DMC results for n=6,7,13 are taken from Ref. [68]. Uncertainties appear in parentheses. 25

3.1 Ground state energies per molecule ($e(N)$) (in K) of *para*H_2 and *ortho*D_2 clusters obtained for the Silvera-Goldman potential (*a*) (Ref. [75]) and Buck potential (*b*) (Ref. [76]) using PIGS (N=11-35). Uncertainties appear in parentheses. 38

3.2 Ground state energies per molecule ($e(N)$) (in K) of *para*H_2 and *ortho*D_2 clusters obtained for the Silvera-Goldman potential (*a*) (Ref. [75]) and Buck potential (*b*) (Ref. [76]) using PIGS (N=36-55). Uncertainties appear in parentheses. 39

4.1 Ground state energies per molecule ($e(N)$) (in K) of $(para H_2)_N(ortho D_2)_3$ clusters obtained for the Silvera-Goldman potential (Ref. [75]) and Buck potential (Ref. [76]) using PIGS. Uncertainties appear in parentheses. 63

5.1 Exact ($J = 0$) bound states of the *para*H_2 and *ortho*D_2 trimers (using the potential of Ref. [75]) 87

List of Abbreviations

BO	*Born-Oppenheimer*
BOP	*Bond Order Parameter*
CMD	*Centroid Molecular Dynamics*
DI	*Double Icosahedra*
DMC	*Diffusion Monte Carlo*
DVR	*Discrete Variable Representation*
GFMC	*Green Function Monte Carlo*
GS	*Ground State*
HENDI	*Helium Nanodroplet Isolation*
IC	*Icosahedron*
ISS	*Icosahedral Shell Sttructure*
ITCF	*Imaginary-time Correlation Function*
LJ	*Lennard-Jones*
MC	*Monte Carlo*
MD	*Molecular Dynamics*
PES	*Potential Energy Surface*
PIGS	*Path Integral Ground State*

PIMC	*Path Integral Monte Carlo*
PIMD	*Path Integral Molecular Dynamics*
POITSE	*Projection Imaginary-time Spectral Evolution*
QMC	*Quantum Monte Carlo*
RDIS	*Return Distance of Inherent Structure*
RMS	*Root Mean Square*
RPMD	*Ring Polymer Molecular Dynamics*
SC-IVR	*Semiclassical Initial Value Representation*
SG	*Silvera-Goldman*
TCF	*Time Correlation Function*
VMC	*Variational Monte Carlo*
VPI	*Variational Path Integral*
ZPM	*Zero Point Motion*

Chapter 1

Introduction

1.1 Context

Clusters are aggregates of particles (atoms or molecules), in a number much smaller than Avogadro's number ($\sim 10^{23}$), i.e. from tens to thousands of particles. From an experimental point of view, clusters present interesting challenges. To produce these systems, sophisticated machinery is necessary. In general, molecular beams are used to perform free jet expansions of the gases of interest into the vacuum. During this process, the gas is cooled well below its condensation point. It is then possible to interrupt the condensation process at any point by adjusting the pressure of the expansion. This yields clusters of different sizes [1]. In terms of the characterization, the conditions under which these systems are synthesized (low temperature and pressure) are ideal for high resolution spectroscopy and numerous methods have been developed for this purpose [2].

Clusters are different from bulk matter in many respects and are regarded as finite size systems. In these systems, the surface plays a very important role in determining physical properties. For example, the surface has the geometrical effect of breaking the translational invariance and isotropy that is present in bulk matter. Additionally, the number of particles that belong to the surface of the system is large when compared to the total number of its constituents. This fact has an important consequence: a small system is not truly extensive, i.e., if we were to divide the small system into pieces, the sum of the partial entropies would not be equal to the entropy of the whole

system. To illustrate this point, let us consider a d-dimensional system containing N particles. In such a system, assuming a spherical shape, approximately $N^{(d-1)/d}$ constituents will be on the surface. It follows that for large N, the relative fraction $N^{-1/d}$ is very small and therefore the surface effects on the bulk properties of the system can be neglected [3]. On the other hand, in a cluster, a high proportion of particles are at the surface. For example, one can estimate that in a cluster containing 500 particles, about one half of them are on the surface. This makes the surface as important for many cluster properties as the interior part itself. Since particles at the surface are more prone to configurational rearrangements, they have a larger impact on the total entropy of the systems compared to those in the interior of the cluster. The latter observation explains the non-extensiveness of finite size systems.

In bulk matter there is an enormous difference in free energy between phases (i.e. gas, liquid, solid, glass, crystalline polymorphism, etc.). As a consequence, only the most favoured phase is observed, and transitions between phases are sharp, characterized by the appearance of nonanalyticity in the free energy. On the other hand, this is no longer true in clusters. Due to the small differences between local minima on a (complicated) free energy landscape [4] that is characteristic of clusters, less favoured "phases" are nearly as observable as more favoured or most favoured "phases", and transitions are rather rounded-off [3].

Formally, true phase transitions require that the system be composed of a large number of particles, strictly speaking, an infinite number of particles in the thermodynamic limit. Thus, it is fair to ask why do real systems exhibit phases despite the fact that they contain a finite number of constituents? One finds the answer in the thermodynamic fluctuations of real systems. Far from a phase transition, fluctuations are not dominant. As the system approaches a phase transition, fluctuations begin to grow in size (i.e. spatial extent). At the transition point, the size of the fluctuations would be infinite, but before this can happen, fluctuations are already as large as the system itself. At this point, "finite-size" effects come into play, and one loses the ability to predict accurately the behaviour of the system. Hence, phases in a real system are well-defined away from phase transitions, and this distance from the

phase transition depends on the size of the system compared to its fluctuations. It follows that one can safely use an infinite model to study bulk matter in equilibrium. On the other hand it also becomes clear that fluctuations dominate the behaviour of small systems such as molecular and atomic clusters and that phase coexistence is very likely to be observed in these systems [5].

An interesting characteristic of clusters is that they may have structures that are not possible for bulk materials. The main example is the icosahedral structure exhibited by many kinds of clusters of a few hundred atoms or fewer. While it is possible to have a bulk solid composed of an assembly of polyhedra, for some clusters, polyhedral structures are unequivocally the structure with the lowest energy. At this point it is worth referring to the work of Alan L. Mackay [6]. In a short paper written over 45 years ago, Mackay introduced two important concepts that have had a tremendous impact in crystallography, particle, cluster, intermetallics and quasi-crystal research. Both of these concepts are related to the growth of non-crystallographic structures. The first idea Mackay introduced was that of icosahedral shell structures (ISS). This type of structure consists of concentric icosahedra displaying fivefold rotational symmetry (see Fig. 1.1 (c)). Structures compatible with this layering are called Mackay icosahedra. It has been observed that the number of particles contained within the icosahedral shells proposed by Mackay agrees very well with the magic numbers observed in rare gas clusters, $(C_{60})_N$ molecular clusters, and some metal clusters [7]. The second concept introduced by Mackay is the hierarchic icosahedral structures. This type of layering is caused by a stacking fault in the fcc packing of the successive triangular faces in the ISS, in other words an icosahedron of interpenetrated icosahedra (DI), giving rise to the so called anti-Mackay shell structure (see Fig. 1.1 (d)).

In the past, several studies [8, 9, 10, 11, 12, 13, 14, 15, 16] were aimed at determining the equilibrium (global minimum) structures of clusters composed of up to a few hundreds particles that interact through a Lennard-Jones (LJ) potential. More recently Mandelshtam and co-workers [17, 18, 19] have looked again at the structures of LJ clusters, in particular $(Ne)_N$, in order to study structural transitions as a func-

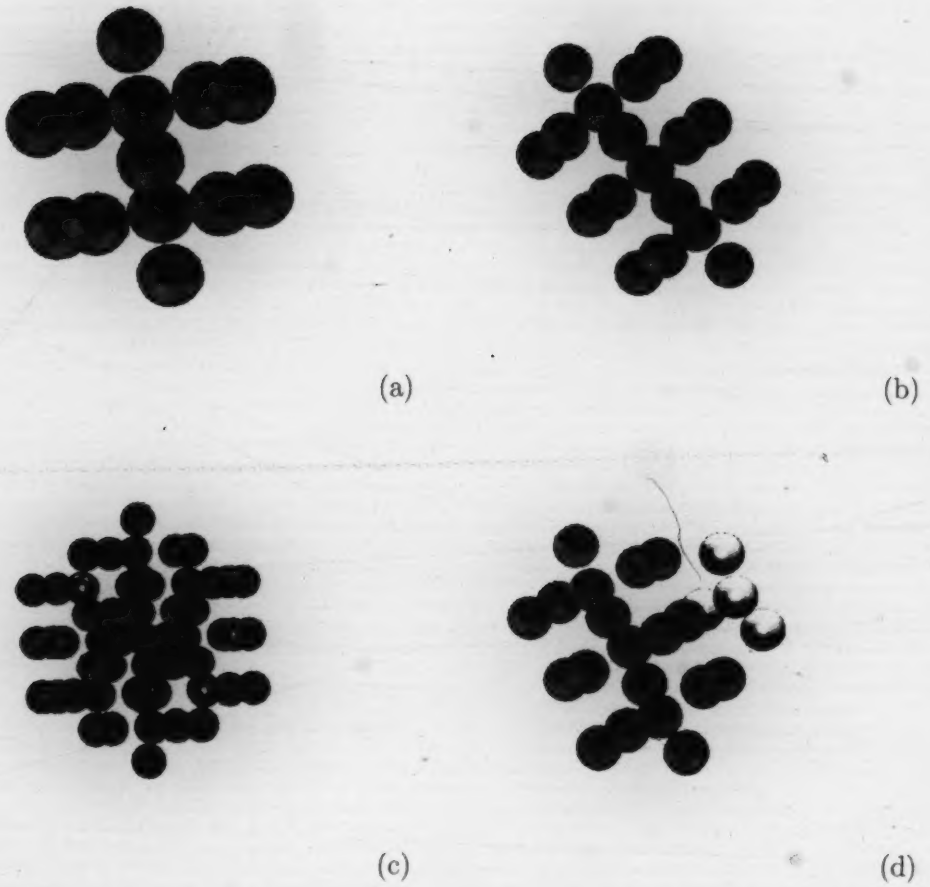

Figure 1.1: Icosahedral structures: 13 particles icosahedron (a), 19 particles anti-Mackay icosaheron (b), 55 particles Mackay icosahedron (c), 23 particles anti-Mackay icosahedron (d).

tion of both temperature and size of the clusters. In these studies the authors found that Ne clusters have an anti-Mackay shell structure in the size ranges of N = 19–30, 56–81. All other clusters studied had an ISS with the exceptions of N = 38 that is an octahedron, N = 98 that has tetrahedral symmetry and N = 75–77,102–104, that display dodecahedral structures. In the latest of these works, the inclusion of quantum effects was studied. It was found that a quantum treatment of these systems favoured in many cases an anti-Mackay shell structure that is less compact and more liquid-like [19]. Only clusters in the ranges of N=39–55,89–92 and $N \geq 96$ were consistent with a Mackay layering.

At this point it becomes clear that not only finite-size but also quantum effects are important at this scale. Spatial delocalization, indistinguishability and particle exchange are responsible for many interesting phenomena. In bulk matter, one of the most striking manifestations of quantum behaviour is the observation of superfluidity in liquid helium. This phenomenon is beautifully illustrated in the following experiment: if a torsional oscillator is immersed in a macroscopic sample of ^{4}He and cooled down, it can be observed that the moment of inertia of the disk decreases sharply below a temperature of 2.12 K. This behaviour is quite opposite to that expected of a viscous classical liquid. This observation is interpreted as if a fraction of the liquid helium is decoupled from the rotation of the oscillator, i.e. zero viscosity, confirming the Tisza [20] and Landau [21] two fluids model of superfluidity. This experiment is known as the Andronikashivili [22] experiment. Nowadays, the phenomenon of superfluidity in the bulk is very well understood, and it is predicted that helium isotopes and hydrogen, under certain conditions [23], are the only candidates to display superfluid behaviour. However, there are still fundamental questions concerning superfluidity in small, finite-sized systems such as clusters. In the past, this inquiry prompted numerous theoretical studies around both helium [24], and in particular hydrogen [25, 26, 27, 28, 29] clusters. The special interest in hydrogen clusters rests on the fact that the superfluid transition in hydrogen is expected at a temperature below its triple point (13.8 K) at which it solidifies. Therefore, clusters have been seen as an alternative to keep hydrogen liquid at very low temperatures.

Most of the theoretical work done on these systems has been based on some kind of quantum Monte Carlo (MC) technique. Finite temperature studies make use of path integral Monte Carlo (PIMC) [30] simulations, while ground state simulations use either variational Monte Carlo (VMC) or Diffusion Monte Carlo (DMC) [31]. Monte Carlo based methods have emerged as the only practical alternative to accurately study many-body quantum systems. The main finding of these investigations revolve around the same observations: pure helium clusters are liquid-like, structureless and superfluid over a certain range of temperatures. On the other hand, pristine small ($N \leq 20$) hydrogen clusters were found to display superfluidity below 2 K, while larger clusters were found to be solid-like and insulators. Finally, the superfluid behaviour of all of these systems is suppressed at higher temperatures where clusters melt into a quantum liquid-like phase.

Despite all the theoretical work done in the past, many questions about these systems remained unanswered for a long time. For example, the fine details of the size evolution of physical properties, including superfluidity, was unknown. Similarly, there was uncertainty in the ground state energies of the smallest hydrogen clusters due to inconsistent results obtained by VMC and DMC calculations [26, 28]

The experimental observation of what can be interpreted as superfluid behaviour at the microscopy level in ^{4}He [32, 33] and *para*H_2 [34] promoted a second generation of theoretical and experimental work. From the experimental point of view, the setup is a microscopic version of the Andronikashivili experiment. In this setup, a nanodroplet of helium is produced by a cryogenic jet expansion. During this procedure, a spectroscopic probe, usually a linear molecule such as OCS, is embedded in the droplet. The rovibrational spectrum of the probe in the ^{4}He environment shows characteristics of a free molecule in a vacuum, which is interpreted as the decoupling of the surrounding ^{4}He atoms from the rotation of the chromophore. It was suggested that this is a manifestation of superfluidity at the microscopic level. These experiments have led to a whole new spectroscopic technique called helium nanodroplet isolation (HENDI) [35]. Soon after the development of HENDI spectroscopy, various theoretical studies on ^{4}He and *para*H_2 clusters doped with chromophores appeared in

the literature [36, 37]. To date, HENDI continues to be an very active research field [38, 39, 40, 41, 42] that aims to better understand superfluidity at microscopic scales.

Some of the knowledge gained is that the evolution of the superfluid behaviour of these clusters as a function of size is non-monotonic. In the case of pristine ^{4}He and *para*H_2 clusters, many of the above questions regarding the size evolution of physical properties have been at least partially answered. Systematic studies of these clusters as a function of size, including the contributions made in this work, have been recently achieved [43, 44, 45, 46, 47, 48, 49]. These works have shed some light on the details of the energetics and structures of a wide range of cluster sizes ranging from $N = 2$ to 55 molecules. In particular, a study by Guardiola and co-workers [46] confirmed the lack of structure of helium clusters. The authors explained the experimentally observed magic numbers in terms of an enhanced growth of the clusters due to sharp peaks in the equilibrium concentrations in the early stage of the cryogenic expansion. Similarly, in the case of hydrogen clusters, new insight is now available. For example, it was determined that in contrast to helium clusters, these systems display real magic numbers and shell structures [44, 45]. However, whether particles within these shells have a solid- or liquid-like character remains an open question, which will be addressed in this work.

More recently, an interesting debate has arisen regarding the nature of the superfluid character of small ($23 \leq N \leq 26$) *para*H_2 clusters. On one side of the controversy, one study [50] has suggested that these clusters have a rigid core with a liquid surface that is responsible for the superfluid response of the system. On the other side, a series of studies [51, 52, 53, 54] have shown that these clusters display phase coexistence between superfluid and insulator phases, and that particle exchange occurs along the whole spatial extent of the clusters, giving to the superfluid phase a non-local behaviour. It is hoped that experimental work in pure clusters, such as the recent work of G. Tejeda *et al.* [55] in Raman spectroscopy will give some definite answers to this intriguing question.

Last but not least, quantum clusters appear as exotic matrices for chemical reactions. Not only spectroscopy but also chemical reactions can be envisioned within

these systems. Possible superfluid behaviour accompanied by fast energy dissipation has awakened interest in what can be considered as a whole new realm: the field of ultra-cold chemistry.

The theoretical exploration of the scenarios described above and the development of methodologies well suited to tackle these problems are of great interest. The aim of this work is to contribute to this endeavour. To this end, we shall study the ground state properties of pristine and mixed clusters composed of hydrogen and deuterium molecules by means of the path integral ground state method (PIGS) [30, 56, 57]. In particular, we will address the details of the evolution of the energetics and structure as a function of the number of constituents of small hydrogen clusters. As the natural continuation of the aforementioned objective, we will investigate the nature of hydrogen and deuterium clusters in terms of their solid- or liquid-like behaviour, as well as their possible size-driven structural transitions. Similarly, we will study the structure and imaginary time dynamics of clusters composed of mixtures of deuterium and hydrogen molecules. In this regard, we will study the effect of quantum environments on the structure and dynamics of weakly bound clusters and the possibility of hydrogen as a suitable matrix for ultra-cold reactions. As a final scientific objective of this work, we will explore methodologies to study quantum dynamics using imaginary-time correlation functions obtained by PIGS simulations: more specifically, the calculation of excited states and rate constants in the framework of quantum clusters. From a technical point of view, we wish to establish the adequacy of the path integral ground state method in conjunction with a fourth order propagator to study quantum finite-size systems. It is our opinion that this method is far superior and much easier to implement than similar ground state methods such as Diffusion Monte Carlo.

As our subject of interest is clusters under conditions where quantum delocalization and exchange are present, we find it pertinent to discuss the basics of the theory of quantum mechanics. The following section presents an introduction to some concepts of quantum mechanics.

1.2 Some Quantum Mechanical Concepts

At the end of the nineteenth century the scientific community believed that all principles of physics had been discovered and that little remained to do in the field but to tune up the experiments in order to get more accuracy in their measurements. This general thinking was somewhat justified by the great advances in physics achieved prior to that time. To name a few, Newton's mechanics had been brought to a high degree of sophistication through the work of Hamilton and Lagrange (i.e. the theory of elasticity and hydrodynamics). Thermodynamics was at its cusp thanks to the collective work of people like Joule, Carnot and Gibbs. The kinetic theory of gases and statistical mechanics were at a great degree of refinement due to Maxwell, Boltzmann and Gibbs. To finish this summary of what is now known as *classical physics*, one cannot leave aside the contribution of Maxwell who unified the fields of optics, electricity and magnetism with his theory of electromagnetism. Little could have been predicted during this golden age of physics about the paradigm changes that were about to occur early in the following century: the theory of relativity and quantum mechanics.

The theory of relativity, due entirely to Einstein, changed the way we see space and time and is an extension of classical physics to the realm of high velocities and astronomical distances. On the other hand, quantum mechanics was developed over several decades by many people and is an extension of classical physics to subatomic, atomic and molecular scales. Although relativity theory has made possible everyday life changes such as nuclear energy, its importance in the field of chemistry is not as obvious as that of quantum mechanics. Quantum mechanics deals with systems in the atomic and molecular region. Under certain conditions, Newton's mechanics is unable to describe properly the behaviour of particles at the microscopic scale. To discern whether a system should be treated under the laws of classical or quantum mechanics, it is useful to invoke the thermal de Broglie wavelength (Λ) of the system. For an ideal gas of particles of mass m at a temperature T, it is defined as $\Lambda = \sqrt{h^2/2\pi m k_B T}$, where h is Planck's constant, and k_B is the Boltzmann constant. Similarly, the de

Boer wavelength, defined as $\lambda = h/(2\pi\sigma\sqrt{m\epsilon})$, where ϵ is the value of the energy minimum of the interaction between particles and σ is the distance at which the interaction energy between two particles is zero. This wavelength is the relevant quantity when interparticle interactions rather than temperature is an important parameter of the system. When any of the quantities described above is much smaller than the interparticle distance, the system can be considered classical. On the other hand, when any of them is on the order of or larger than the interparticle distance, quantum effects will dominate the behaviour of the system.

Thus, it can be seen that in the realm of light particles, low temperatures and/or weakly interacting systems, quantum behaviour is manifest. The following subsection provides a brief introduction to the main tenets of quantum mechanics.

1.2.1 The Schrödinger equation and the Born-Oppenheimer approximation

In quantum mechanics, due to Heisenberg's uncertainty principle, the state of a system at a given time cannot be described by its phase space variables, namely momentum and position. A quantum system is instead represented by a function that depends only on either position or momentum, the wave function. Similarly, the dynamics of a many particle system is described in quantum mechanics by the time-dependent Schrödinger equation (here we have chosen the position representation)

$$i\hbar\frac{\partial\Phi(\mathbf{R},\mathbf{r},t)}{\partial t} = \hat{H}\Phi(\mathbf{R},\mathbf{r},t) \tag{1.1}$$

where i is the imaginary unit, t is the time, $\hbar = h/2\pi$, $\mathbf{R}$ and $\mathbf{r}$ are vectors representing the nuclear and electronic coordinates respectively, $\Phi(\mathbf{R},\mathbf{r},t)$ is the wave function and $\hat{H}$ is the Hamiltonian. For a closed and isolated molecular system, $\hat{H}$ is time independent and is given by

$$\hat{H} = -\sum_A \frac{\hbar^2}{2m_A}\nabla_A^2 - \frac{\hbar^2}{2m_e}\sum_i \nabla_i^2 - \frac{e}{4\pi\epsilon_0}\sum_{i,a}\frac{Z_A}{|r_i - R_A|} + \frac{e^2}{4\pi\epsilon_0}\sum_{i<j}\frac{1}{|r_j - r_i|} + \frac{1}{4\pi\epsilon_0}\sum_{A<B}\frac{Z_A Z_B}{|R_A - R_B|}. \quad (1.2)$$

The indices A and B refer to nuclei and i and j refer to electrons. The first term is the kinetic energy operator for each nucleus of mass m_A. Similarly, the second term is the kinetic contribution of the electrons (m_e refers to the electron mass). The rest of the terms correspond to the Coulombic interaction between the particles: the first is the attraction between electrons and nuclei bearing charges e and Z respectively and the last two terms correspond to the repulsion between like particles (electron-electron and nucleus-nucleus).

Eq. 1.2 can be rewritten in a more compact way that emphasizes its operational character as

$$\hat{H} = \hat{T}_N(\mathbf{R}) + \hat{T}_e(\mathbf{r}) + \hat{V}_{eN}(\mathbf{r}, \mathbf{R}) + \hat{V}_{ee}(\mathbf{r}) + \hat{V}_{NN}(\mathbf{R}), \quad (1.3)$$

where $\hat{T}$ is the kinetic energy operator and $\hat{V}$ is the corresponding operator for the potential energy. The term $\hat{V}_{eN}(\mathbf{r}, \mathbf{R})$ prevents us from separating $\hat{H}$ into nuclear and electronic parts. Therefore, the wavefunction cannot be expressed as a simple product of nuclear and electronic terms. The Schrödinger equation with such a non-separable Hamiltonian can be solved analytically only for systems containing a single electron. One way to circumvent this limitation and study the quantum dynamics of multi-electronic systems is to resort to the Born-Oppenheimer (BO) approximation. In 1927, Born and Oppenheimer [58] showed that nuclear and electronic motions can be decoupled. This is possible due to the very different time scales of the motion of electrons and nuclei. The physical picture behind this decoupling is the observation that the electron is much lighter than the nucleus. The electron charge density is therefore able to quickly rearrange in response to the slower nuclear motion. By the same token, the nucleus can be regarded as being fixed with respect to the electronic motion. This allows for the separation of the Hamiltonian through a parametric

dependence on the nuclear coordinates so that the total wavefunction can be written as the product $\Psi(\mathbf{r};\mathbf{R})\chi(\mathbf{R})$. With this separation, the Schrödinger equation can be solved for a fixed nuclear geometry and the corresponding electronic energy is obtained by diagonalizing the Hamiltonian. One can obtain the potential energy surface (PES) by repeating the above procedure varying geometries over a large range of nuclear coordinates. The PES can then be used to study the dynamics of the nuclei. The BO approximation assumes that the nuclear dynamics evolves on a PES associated with a single electronic quantum state (adiabatic) such that electronic excitations do not occur upon nuclear motion. Using the BO approximation, one can further write the Hamiltonian of an N-particle system depending explicitly only on nuclear coordinates as

$$\hat{H} = \hat{H}_0 + \hat{V} = -\hbar^2 \sum_{A=1}^{N} \frac{\nabla_A^2}{2m_A} + V(\mathbf{R}) \tag{1.4}$$

where $V(\mathbf{R})$ is a function that describes the interaction between particles. The kinetic energy operator now corresponds to the complete Hamiltonian of a non-interacting system, hence $\hat{T} \equiv \hat{H}_0$. Since there is no explicit time-dependence in the Hamiltonian, one can obtain its eigenvalues (energies) and eigenfunctions by solving the so called time-independent Schrödinger equation

$$\hat{H}\Phi(\mathbf{R}) = E\Phi(\mathbf{R}). \tag{1.5}$$

Alternatively (for a time-independent Hamiltonian) the general solution to the partial differential equation in Eq. 1.1 is given by

$$\Phi(\mathbf{R}, t) = \exp\left[-i\hat{H}t/h\right]\Phi(\mathbf{R}, 0) = \hat{U}\Phi(\mathbf{R}, 0) \tag{1.6}$$

where $\hat{U}$ is regarded as the time propagation operator or propagator. Thus, the state of a system at time t can be obtained as the propagation of its wavefunction at time $t=0$. This interpretation is known as the Schrödinger representation of time evolution. In this picture of quantum dynamics, operators do not change in time, instead the wavefunction changes as a result of the action of the propagator.

One can write all above equations using a different notation: Dirac's bra-kets notation. In this notation, a physical system is associated with a complex Hilbert

space such that each instantaneous state of the system is described by a vector (ket) in that space. Next, it becomes useful to define the inner product in the Hilbert space associated with the system, in the position representation:

$$\langle \mathbf{R}(t)|\mathbf{R}'(t)\rangle \equiv \int d\mathbf{R}d\mathbf{R}'\Phi(\mathbf{R},t)^*\Phi(\mathbf{R}',t) \tag{1.7}$$

The Schrödinger equation provides a quantitative description of the rate of change of the state vector, as it does for the wave function. Using Dirac's notation, we can write the Schrödinger equation as

$$ih\frac{\partial}{\partial t}|\mathbf{R}(t)\rangle = \hat{H}|\mathbf{R}(t)\rangle, \tag{1.8}$$

with a solution for a time-independent Hamiltonian given by

$$|\mathbf{R}(t)\rangle = \exp[-itE/\hbar]|\mathbf{R}(0)\rangle. \tag{1.9}$$

Let the set $\{|\mathbf{R}_n\rangle\}$ be the eigenvectors of the Hamiltonian, i.e., the set of solutions of the time-independent Schrödinger equation. It follows that any state that is a solution of the time-dependent Schrödinger equation can be written as a linear combination of the energy states, as they form a complete basis:

$$|\mathbf{R}(t)\rangle = \sum_n c_n(t)|\mathbf{R}_n\rangle. \tag{1.10}$$

The above allow us to obtain the solution of the time dependent Schrödinger equation in terms of the energy eigenvectors as

$$|\mathbf{R}(t)\rangle = \sum_n \exp[-itE_n/\hbar]c_n(0)|\mathbf{R}_n\rangle. \tag{1.11}$$

Although all the above equations represent a rigourous framework to describe the equilibrium and dynamical properties of a quantum system, the exact solution of the time-independent Schrödinger equation is not possible for any but the simplest systems. Therefore, many approximations and alternatives have been developed to study many-body quantum systems. The following section describes one such alternative, based on Feynman's path integral formulation of quantum mechanics.

1.3 Path Integrals and Monte Carlo Methods

One of the many contributions of Richard Feynman to modern physics is the realization that a quantum system can be mapped onto a classical model of interacting "polymers" [59]. This can be done through the implementation of Feynman's path integral formalism of quantum mechanics. This mapping allows for a classical, and far more intuitive picture of a quantum system and it facilitates the translation of the theory into computational algorithms and techniques such as Monte Carlo methods. The advantages of this representation of quantum mechanics have long been exploited by condensed matter physicists. In particular, the understanding of Bose condensation and superfluidity of helium has benefited enormously from Feynman's path integrals [30]. The following sections are intended as a formal introduction, emphasizing clarity over exhaustiveness, of the theory and modern use of Feynman's path integrals in the context of ground state Monte Carlo (MC) simulations.

1.3.1 Path Integral Ground State (PIGS)

At sufficiently low temperature, the physics of a given system is governed by that of its ground state (GS). Therefore, methods have been developed to specifically study the state of lowest energy of a system. The path integral ground state (PIGS) or alternatively known as variational path integral (VPI) is one such method. The basic idea behind PIGS is to project out the GS wave function from a trial wave function non-orthogonal to the true ground state of the system. The aim is the same as in methods such as diffusion Monte Carlo (DMC) and Green's function Monte Carlo (GFMC) and therefore, all these implementations are collectively known as projection methods.

Let us consider the Hamiltonian given in 1.4. Formally, one can obtain the exact GS wave function $\Phi_0(R)$ from a trial wave function $\Psi_T(R)$ as

$$\Phi_0(\mathbf{R}) \propto \lim_{\beta\to\infty} \int d\mathbf{R}' G(\mathbf{R}, \mathbf{R}', \beta)\Psi_T(\mathbf{R}'), \tag{1.12}$$

where

$$G(\mathbf{R}, \mathbf{R}', \beta) = \langle \mathbf{R}| \exp[-\beta \hat{H}] |\mathbf{R}'\rangle \tag{1.13}$$

is referred to as the imaginary-time propagator. The term imaginary-time becomes clear if in Eq. 1.6 we make the change $t/\hbar \rightarrow -i\beta$. Although Eq. 1.12 is exact, one does not normally know how to compute $G(\mathbf{R}, \mathbf{R}', \beta)$ exactly for a nontrivial many-body system. However, there exist [60, 61, 62] approximations (referred to as short-time approximations) to the propagator whose accuracy increases as $\beta \rightarrow 0$. Consider $G_0(\mathbf{R}, \mathbf{R}', \beta)$ to be one such approximation. One can take advantage of the identity $\exp[-\beta \hat{H}] \equiv (\exp[-\tau \hat{H}])^M$, with $\beta = M\tau$ and obtain $G(\mathbf{R}, \mathbf{R}', \beta)$ as

$$G(\mathbf{R}, \mathbf{R}', \beta) \approx \int d\mathbf{R_1} \cdots d\mathbf{R_{M-1}} G_o(\mathbf{R}, \mathbf{R_1}, \tau) G_o(\mathbf{R_1}, \mathbf{R_2}, \tau) \cdots G_o(\mathbf{R_{M-1}}, \mathbf{R}', \tau). \tag{1.14}$$

For any finite value of M, Eq. 1.14 is approximate, becoming exact only in the limit $M \rightarrow \infty$ (i.e., $\tau \rightarrow 0$). In practice one is forced to work with finite values of M and τ. Therefore, one must choose a τ sufficiently small such that the replacement of G by G_0 does not introduce a significant loss of accuracy. At the same time, the product $M\tau$ should be large enough so that one approaches to the GS with the desired accuracy. The MC implementation of this method requires the statistical sampling of paths from the probability density

$$P(X) \propto \Psi_T(\mathbf{R_0}) \Psi_T(\mathbf{R_{2M}}) \prod_{j=0}^{2M-1} G_0(\mathbf{R_j}, \mathbf{R_{j+1}}, \tau) \tag{1.15}$$

It can be shown [30, 56] that in the limits ($\tau \rightarrow 0$, $M\tau \rightarrow \infty$), $\mathbf{R_M}$ is sampled from a probability density proportional to the square of the exact GS wave function $\Phi_0(\mathbf{R})$ irrespective of the choice of $\Psi_T(\mathbf{R})$. Therefore, expectation values of quantities $F(\mathbf{R})$ that are diagonal in the position representation can be obtained as statistical averages over the set $\{\mathbf{R_M^P}\}$ of midpoint configurations $\mathbf{R_M}$, i.e.,

$$\langle \Phi_o | \hat{F}(\mathbf{R}) | \Phi_o \rangle \approx \frac{1}{P} \sum_{p=1}^{P} F(\mathbf{R_M}^P). \tag{1.16}$$

The GS expectation value of the energy can be obtained using the so called mixed

estimate:

$$\langle \Phi_0 | \hat{H} | \Phi \rangle \approx \sum_{p=1}^{P} \frac{\hat{\Psi}_T(\mathbf{R}_M^p)}{\Psi_T(\mathbf{R}_M^p)}, \tag{1.17}$$

which provides an unbiased result for the Hamiltonian operator $\hat{H}$ since the later commutes with the imaginary time evolution propagator $\exp[-\tau\hat{H}]$.

1.3.2 Imaginary-time Propagator

As mentioned in Section 1.3.1, several forms are possible for G_0. It must be clarified at this point that the difference between propagators is only of computational efficiency. If we consider the Hamiltonian of Eq. 1.4, the simplest factorization of the exponential operator, known as the primitive factorization, is

$$\exp[-\tau\hat{H}] = \exp[-\tau\hat{V}/2]\exp[-\tau\hat{H}_0]\exp[-\tau\hat{V}/2] + O(\tau^3), \tag{1.18}$$

and this leads, after some algebra, to an expression for the propagator

$$G_P(\mathbf{R}, \mathbf{R}', \tau) = \rho_F((\mathbf{R}, \mathbf{R}', \tau)\exp[-1/2\tau(V(\mathbf{R}) + V(\mathbf{R}')] + O(\tau^3), \tag{1.19}$$

where

$$\rho_F(\mathbf{R}, \mathbf{R}', \tau) \equiv \langle \mathbf{R}| \exp[-\tau\hat{H}_0]|\mathbf{R}'\rangle = \left(2\pi\hbar^2\tau\right)^{-3N/2} \prod_{i=1}^{N} \exp\left(-\frac{m_i(\mathbf{r}_i - \mathbf{r}'_i)^2}{2\hbar^2\tau m_i^{-3/2}}\right) \tag{1.20}$$

is the exact propagator for a system of noninteracting particles.

The primitive approximation (PA), when used in Eq. 1.14, leads to an expression for the propagator G, that is accurate up to a term of order $1/M^2$. A number of propagators that enjoy a higher order of accuracy in τ have been derived [60, 61, 62] but their application in GS Monte Carlo calculations has been somehow rare [63, 64].

In this thesis, we shall make use of a high order factorization that is accurate to a term of order $1/M^4$:

$$\begin{aligned} \exp[-\tau\hat{H}] = \quad & \exp\left[-\tfrac{\tau}{6}\hat{H}_0\right] \quad \exp\left[-\frac{3}{8}\tau\hat{V}\right] \exp\left[-\frac{\tau}{3}\hat{H}_0\right] \exp\left[-\frac{\tau}{4}\hat{C}\right] \\ & \times \exp\left[-\tfrac{\tau}{6}\hat{H}_0\right] \quad \exp\left[-\frac{3}{8}\tau\hat{V}\right] \exp\left[-\frac{\tau}{3}\hat{H}_0\right] + O(\tau^5), \end{aligned} \tag{1.21}$$

with

$$\hat{C} = \hat{V} + \frac{1}{48}\tau[\hat{V}, [\hat{H}_0, \hat{V}]] \tag{1.22}$$

This factorization yields the following approximation to the propagator:

$$G_0(\mathbf{R}_j, \mathbf{R}_{j+1}, \tau) = \rho_F(\mathbf{R}_j, \mathbf{R}_{j+1}, \tau) \exp\left[-\frac{2\tau\hat{V}(\mathbf{R}_j)}{3}\right] \rho_V(\mathbf{R}_j), \tag{1.23}$$

where

$$\rho_V(\mathbf{R}_j) = \exp\left[-\frac{2\tau\hat{V}(\mathbf{R}_j)}{3} - \frac{\tau^3\hbar^2}{9}\sum_{i=1}^{N}[\nabla_i\hat{V}(\mathbf{R}_j)]^2/m_i\right] \tag{1.24}$$

if j is odd, whereas $\rho_V(\mathbf{R}_j) = 1$ if j is even.

1.3.3 Monte Carlo Integration

As stated in Section 1.3.1, the numerical implementation of PIGS requires the sampling of paths from the probability density given in Eq. 1.15. To accomplish this, one needs to evaluate a product of multidimensional integrals G_0. Numerical integration can be done in many different ways. For example, let us consider the following one-dimensional integral:

$$I = \frac{1}{b-a}\int_a^b f(x)dx. \tag{1.25}$$

Any method of choice will involve the evaluation of the integrand $f(x)$ in a series of points $\{x_m\} \ni [a, b]$. These points can be, for example, uniformly distributed in a grid as in the trapezoidal method. Then the integral can be evaluated as an appropriate weighted sum of the values $\{f(x_m)\}$. In the Monte Carlo method $\{x_m\}$ is sampled randomly from an uniform distribution and the integral is then evaluated as:

$$I \approx \frac{1}{M}\sum_{m=1}^{M} f(x_m) \tag{1.26}$$

The variance of the result is given by

$$\sigma^2 = \frac{\sum_{m=1}^{M}(f(x_m) - I)^2}{M(M-1)} \tag{1.27}$$

and so, the error decreases with the number of evaluations, M, as $\sim M^{-1/2}$, whereas the error in the trapezoidal rule goes as $\sim M^{-2/d}$, d being the dimensionality of

the integral. Hence MC integration is less efficient than grid-based methods for the one-dimensional case, but as d increases MC becomes the only practical approach.

1.4 Overview and organization of the thesis

In this thesis we present our contributions to the characterization and understanding of the physics relevant to clusters of hydrogen and deuterium molecules in their ground state. To this end, we use computer simulations based on the path integral formalism of quantum mechanics. We can summarize our computational approach as follows: the true ground state wavefunction of a many-particle system can be extracted through projection in imaginary time of a trial wavefunction. The discretization of the imaginary-time propagation gives rise to "paths" of particles in imaginary time. To compute ground state expectation properties, one needs to sample that given property at the middle point in the imaginary-time path. This is done using a Monte Carlo technique. The last piece of the puzzle corresponds to the details of how paths will be sampled. In this work we will use the multilevel Metropolis algorithm, as described in Ref. [30]. Using this methodology we do a systematic study of the energetics and structure of hydrogen clusters as a function of size, in particular in the range of N =2–20. These results are shown in Chapter 2. In Chapter 3, our aim is to characterize the solid- or liquid-like behaviour of hydrogen and deuterium clusters ranging from N=11–55. In Chapter 4, we study the weakly bound deuterium trimer inside hydrogen clusters of different sizes. A discussion of dynamical properties from imaginary time correlation functions is presented in Chapter 5. We draw our conclusions and present possible future avenues in Chapter 6.

Chapter 2

Path integral ground state: Applications to small hydrogen clusters

In this chapter, we study the energetic and structural properties of small *para*H_2 clusters of sizes ranging from 2 to 20 molecules. Simulations are done using the path integral ground state (PIGS) method. We use a fourth order formula to approximate the short imaginary-time propagator. Our results are compared to those of exact basis set calculations and, when available, to these of other quantum Monte Carlo methods. We find that for all cluster sizes under consideration, our results show a lower ground state energy than literature values obtained by diffusion Monte Carlo and variational Monte Carlo approaches. For the dimer and trimer, ground state energies are in good agreement with exact results obtained using the discrete variable representation. Finally, we explore the use of Pekeris coordinates to analyse the importance of linear arrangement in the *para*H_2 trimer, and in trimers within clusters of a larger size.[1]

[1]The results presented in this chapter have appeared in an article entitled: *Path integral ground state study of finite size systems: Application to small (para-hydrogen)$_N$ ($N = 2 - 20$) clusters* Reused with permission from Javier Eduardo Cuervo and Pierre-Nicholas Roy, The Journal of Chemical Physics **125**, 124314 (2006). Copyright 2006 American Institute of Physics.

2.1 Introduction

Clusters and droplets of the lightest chemical species in nature, such as helium and molecular hydrogen, have quite interesting properties. The weak nature of their intermolecular interactions (dispersion forces) and the low mass of their constituents lead to important delocalization effects that can be observed at both finite temperature and in the ground state. Of particular interest is the fact that such finite systems have been proposed as candidates for microscopic manifestations of superfluidity. Simulation studies have shown that superfluidity can occur in ^{4}He and *para*H_2 clusters [24, 25]. Microscopic superfluidity was later observed experimentally in doped helium nano-droplets [32] and vigourous research efforts have been devoted to the field of quantum nano-clusters in recent years.

Quantum Monte Carlo (QMC) methods have been the tool of choice for most of the theoretical studies of quantum clusters. In particular the path integral Monte Carlo (PIMC) method [30] has been widely used to study the energetic, structural and superfluidic properties of clusters at finite temperature. Similarly, ground state studies using diffusion Monte Carlo (DMC) [65] and variational Monte Carlo (VMC) [66, 67] methods have shed some light on the structure [26, 68], of clusters ($N < 50$) of ^{4}He and H_2. A common feature among these studies is the use of sophisticated trial wave functions variationaly tuned for different cluster sizes. More recently Baroni *et al* [38] studied the quantum melting of a small pure and CO doped H_2 clusters by means of reptation Monte Carlo [69]. However, QMC methods are not the only way to study these clusters. An *ab initio* study [70] has contributed to the understanding of the growth process of H_2 clusters, while Gianturco *et al* [71], by means of discrete variable representation (DVR), have studied the differences in binding of ^{3}He and ^{4}He to *ortho* and *para*H_2.

Important progress has been achieved in our understanding of hydrogen clusters, but some questions remain. Particularly, ground state properties of small $(para\mathrm{H_2})_N$ ($N \leq 20$) have not been completely addressed. Available studies focus for instance on clusters with "magic numbers" (7, 13, 19, 33, etc.) of particles. Additionally, incon-

sistency between results obtained using VMC and DMC methodologies [26, 68] has raised questions about the quality of the current ground state energies of these systems. The goal of the present work is to provide accurate ground state energetics and structures of p-H_2 clusters with ($N \leq 20$). We also present the first cluster application of the path integral ground state (PIGS) method using a fourth order propagator to achieve this objective. PIGS has previously been used to study condensed-phase ^{4}He [56, 57] and absorption of H_2 onto different substrates [72, 73] but its applicability to clusters or droplets has not been fully addressed [56, 74]. The remainder of this Chapter is organized as follows: in the following Section we describe the physical system under consideration; in Section 2.3 we present and discuss our results. We finally present conclusions in Section 2.4.

2.2 paraHydrogen clusters

Simulations of $(para H_2)_N$ clusters are performed using a model composed of a set of N point particles that move in three dimensions, enclosed in a parallelepiped box of volume Ω with periodic boundary conditions in all directions. The size of the box is chosen to be larger than the characteristic size of the clusters. The quantum mechanical Hamiltonian is that of Eq. 1.4 with a pairwise additive intermolecular potential,

$$V(\mathbf{R}) = \sum_{i<j} v(r_{ij}), \tag{2.1}$$

where $v(r_{ij})$ is a pair potential that depends of the relative distance, r_{ij}, between two H_2 molecules i and j. We consider two models for $v(r_{ij})$: the potential of Silvera and Goldman [75], widely used to study condensed-phase H_2 (designated Silvera-Goldman henceforth), and for the purpose of comparison with previous QMC studies, the gas-phase potential of Buck *et al.* [76].

2.3 Results and discussion

Structural properties and energies of *para*H_2 clusters were calculated using the PIGS method described in Sec. 1.3.1. For all calculations, we used a trial wave function of the type,

$$\Psi_T(\mathbf{R}) = \exp\left[-\frac{1}{2}\sum_{i<j} u(|\ \mathbf{r}_i - \mathbf{r}_j\ |)\right], \tag{2.2}$$

where $\mathbf{R} = \{\mathbf{r}_1, \mathbf{r}_2, \ldots, \mathbf{r}_N\}$ denotes the vector that contains the Cartesian coordinates (r_i) of the N particles of the cluster. The pseudopotential u is given by

$$u(r_{ij}) = \left(\frac{b}{r_{ij}}\right), \tag{2.3}$$

with b= 3.65 Å. This wave function has the same form of the one commonly used in condensed-phase systems such as liquid ^{4}He [57]. This far from optimized trial wave function has been chosen for the sole purpose of demonstrating the robustness of PIGS method. Note that as long as the trial wave function has a finite overlap with the true ground state, and the projection time is sufficiently long, convergence will be achieved in PIGS.

2.3.1 Energetics

We calculated the ground state energies of $(H_2)_N$ (N = 2–20). Individual convergence studies of the total energy with respect of the time step (τ) and projection time (β) were carried out for each cluster size up to N=10. For clusters with $N > 10$, β and τ where chosen based on the results of the convergence studies for smaller clusters. We observe that converged parameters are independent of the model potential. In the following, unless otherwise stated, we give details of the results obtained using Silvera-Goldman potential. More specifically, for cluster sizes 2,3,4,5, the (β, τ) values were set to (2.1, 0.0038), (1.4, 0.0027), (1.0, 0.0033), (1.02, 0.0068) respectively and for cluster sizes 6 to 10, the (β, τ) values were set to (0.84, 0.00168). For clusters with N = 11–20 the (β, τ) values were set to $(0.8, 0015625)$. Note that it was previously observed [57] that structural properties converge well before the energy does. Expectation values of the total energy per molecule as a function of τ were fitted to the

following quartic expression [77] $e(\tau) = a + b\tau^4$. Representative results for N=4 are shown in Fig. 2.1 (a), in which can be observed the expected quartic behaviour [78]. Note, however, that for the current case of finite-size systems, the energy increases as $\tau \rightarrow 0$ whereas an opposite trend was observed in the bulk [57]. A larger time step will therefore yield more tightly bound clusters and this may be interpreted as a more classical result. Based on the convergence studies, we chose time steps such that, within statistical error, the calculated energies were identical to the extrapolated values at $\tau = 0$. Similarly, the projection time β for each cluster is chosen by fitting the energy to the expression $e(\beta) = a + b\exp(-c\beta)$ (see Fig. 2.1 (b), for N=4). Table 2.1 summarizes the results for both potentials. As a further test to our PIGS calculations, we calculated the e of the dimer and trimer by means of exact diagonalization in the discrete variable representation (DVR) [79, 80]. The dimer energy per molecule was calculated using direct diagonalization of the Hamiltonian represented in a Colbert and Miller DVR [81]. The PIGS energy per particle is -1.88(5) K for the Silvera-Goldman potential. This number is in agreement with the exact DVR energy (-1.92 K). Results obtained using the Buck potential (Table 2.1) also show a good agreement between PIGS (-2.19(3) K) and DVR (-2.16 K) calculations. In this particular case, the VMC calculation of Ref. [68] yields the same energy as the DVR calculation for the reported precision. Trimer calculations were performed using a symmetry-adapted Lanczos diagonalization procedure using Pekeris coordinates and a Jacobi DVR [82, 83, 84]. We found that our PIGS result agreed very well with the exact calculation (approx. 0.7% of discrepancy) for the Silvera-Goldman potential. Similarly, an accurate result of -4.91(2) K was obtained for the Buck potential using PIGS (the DVR result is -4.89 K). In this case, the VMC result of -2.299(2) K corresponds to only 48% of the ground state energy calculated by DVR. This implies that the VMC wave function of Ref. [68] does not accurately describe the true ground state. We see in Table 2.1 that for clusters of size N=3,4,5 our results differ greatly from the existing VMC data [26]. Our PIGS energies are much lower in these cases. For larger clusters (N=6,7), our ground state energies are about 8% lower than the VMC [68] results but are much closer to the DMC results

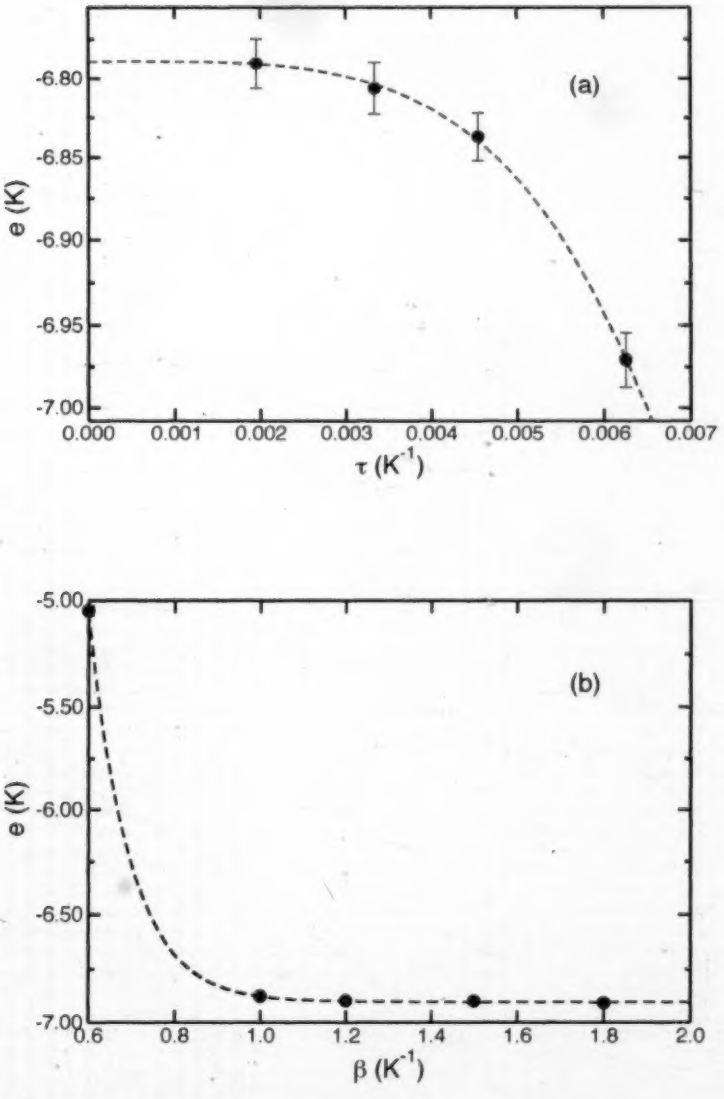

Figure 2.1: (Upper panel) Total energy per H_2 molecule ($e(\tau)$) (in K) as a function time step τ (in K^{-1}). The total projection time is $\beta = 1$ K^{-1} . The calculations were carried out for four particles using the Silvera-Goldman potential (Ref. [75]) . The dashed line is the quartic fit to the PIGS data. (Bottom panel)Total energy per H_2 molecule ($e(\beta)$) (in K) as a function of projection time β (in K^{-1}). The time step used in all calculations is $\tau = 0.0066$ K^{-1} . The calculations are for the same system as in (a). The dashed line is a fit to the PIGS data based on the expression: $e(\beta) = a + b\exp(-c\beta)$. Error bars are within the size of the symbols.

Table 2.1: Ground state energies per molecule ($e(N)$) (in K) of small *para*H_2 clusters obtained for the Silvera-Goldman potential (a) (Ref. [75]) and Buck potential (b) (Reference [76]) using PIGS. DVR results for the dimer and trimer are also shown. VMC results for n=2,3,4,5 are taken from Ref. [26], VMC and DMC results for n=6,7,13 are taken from Ref. [68]. Uncertainties appear in parentheses.

Cluster size	DVR[a]	PIGS[a]	DVR[b]	VMC[b]	DMC[b]	PIGS[b]
2	-1.92	-1.88(5)	-2.16	-2.155(1)		-2.19(6)
3	-4.39	-4.32(3)	-4.89	-2.299(2)		-4.91(2)
4		-6.76(2)		-2.611(2)		-7.75(2)
5		-9.02(2)		-2.664(1)		-10.29(2)
6		-10.92(2)		-11.390(5)	-12.1649(7)	-12.40(2)
7		-12.62(2)		-13.013(2)	-14.13(2)	-14.27(2)
8		-14.11(2)				-15.92(2)
9		-15.46(2)				-17.41(2)
10		-16.72(2)				-18.78(2)
11		-18.00(2)				-20.22(3)
12		-19.24(2)				-21.68(3)
13		-20.49(2)		-19.992(6)	-22.85(7)	-23.03(3)
14		-21.20(1)				-24.04(1)
15		-22.20(1)				-24.93(1)
16		-22.95(1)				-25.72(1)
17		-23.65(1)				-26.49(1)
18		-24.34(1)				-27.23(1)
19		-25.03(1)				-28.01(1)
20		-25.69(1)				-28.69(1)

of Ref. [68] (the differences are of about 2%). For clusters of sizes N=8–12,14–20, no previous calculations were available for the Buck potential and the present PIGS results can therefore serve as benchmarks. For N=13 our result is $\approx 3\%$ more negative than the DMC result. Note that the energies for N=2–20 reported in Table 2.1 are the first such results for the Silvera-Goldman potential. For completeness and comparison purposes, we show in Fig. 2.2 the evolution of the chemical potential as a function of cluster size, defined as $\mu(N) \approx E(N) - E(N-1)$, where $E(N)$ is the total energy of a cluster of N particles. A similar overall trend was found for the two potentials considered, however, some differences can be observed.

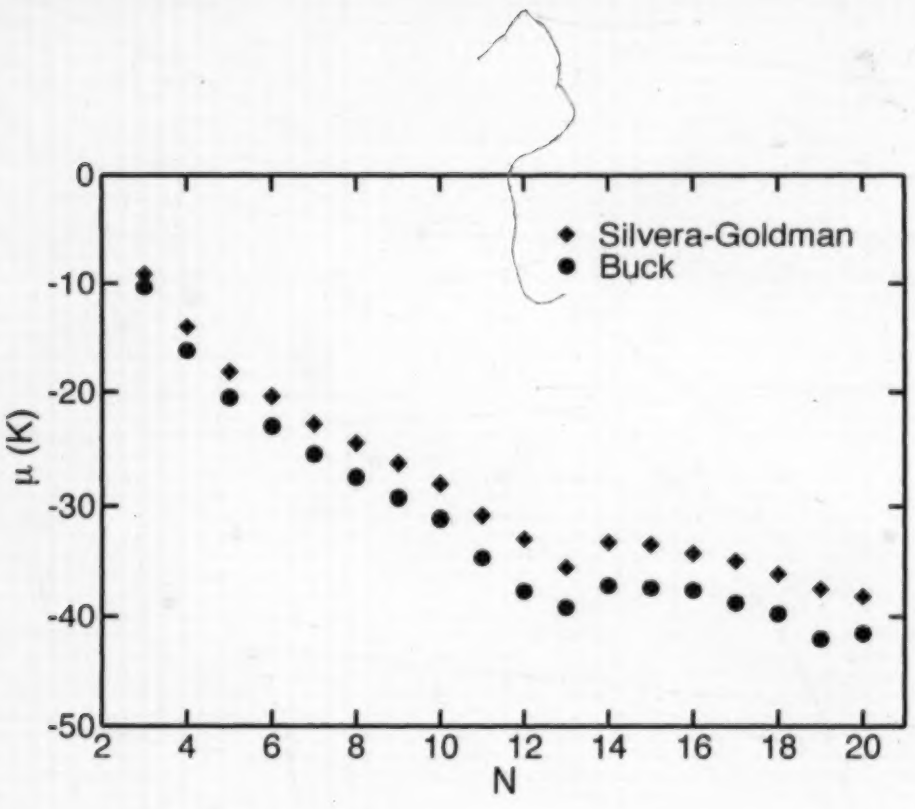

Figure 2.2: Chemical potential (μ) as a function of N using Silvera-Goldman potential (Ref. [75]) (diamonds) and Buck potential (Ref. [76]) (filled circles). Error bars are within the size of the symbols.

The chemical potential described by the Buck potential changes more rapidly with cluster size up to N=12, than does the Silvera-Goldman model. At N=13 both curves show a dip in μ, and this reduction is more pronounced for the case of the Silvera-Goldman potential. This feature is consistent with previous observation of "magic numbers" in these clusters. Furthermore, at N=19 (another "magic number") [27], the curve corresponding to the Buck potential shows another dip that is not observed when the Silvera-Goldman potential is used. At this cluster size, the system is expected to have an important contribution from a highly "ordered" structure [27].

2.3.2 Structural properties

Structural properties of the $(H_2)_N$ clusters were also computed using the PIGS method. We first note that the structural properties do not depend on the choice of interaction potential for these clusters. We present in Fig. 2.3 the cluster density, $\rho(r)$, as a function of the distance from the centre-of-mass, r. The density is defined according to the following normalization: $4\pi \int_0^\infty \rho(r) r^2 \mathrm{d}r = N$. One can observe that for N=3, there is a finite particle density at the centre-of-mass, an indication of the possibility of linear configurations and an indication of the floppiness of this weakly-bound trimer. Conversely, clusters with N=4,5,6,7 have a reduced density at the centre-of-mass and are likely to have a hollow core. These results are in agreement with earlier DMC calculations [68], in particular for N=6,7. For clusters with N=4,5, we report, to the best of our knowledge, the first structural results of this kind. For N=8, the density at the centre of the cluster begins to build up. This is more pronounced for N=9,10 where it is clear that a particle appears near the centre of the cluster at $N = 10$. This central density progressively increases with cluster size in the range $N = 10-14$ as shown in Figs. 2.3 (c) and 2.3 (d). Conversely, for $N = 15 - 18$ the density at the centre-of-mass gets depleted. This can be associated to the liquid-like nature of these systems. At N=19,20 the peak in density closer to the centre-of-mass is shifted to $r \approx 1.3$ and 1.8 Å respectively. This is an indication of a structural change in which no particle sits at the centre-of-mass and instead, some density starts to build around the centre of the cluster. We also present the pair distribution function, $g(r)$, for $N = 3, 7, 13, 20$ in Fig. 2.4. For all cluster sizes, the distributions have a maximum at $r \approx 4$ Å. As N grows, the $g(r)$ extends to greater distances as expected. For $N = 13-20$ a shoulder start to develop at $r \approx 7$ Å . Our results are in agreement with those obtained by Tejeda *et al* [55] using DMC. In that work, the authors present a pair distribution function, $P(\mathbf{R})$, normalized such that $\int_0^\infty P(\mathbf{R}) d\mathbf{R} = 1$. Therefore the amplitude of the shoulder appearing at ≈ 7 Å is enhanced by the r^2 Jacobian factor.

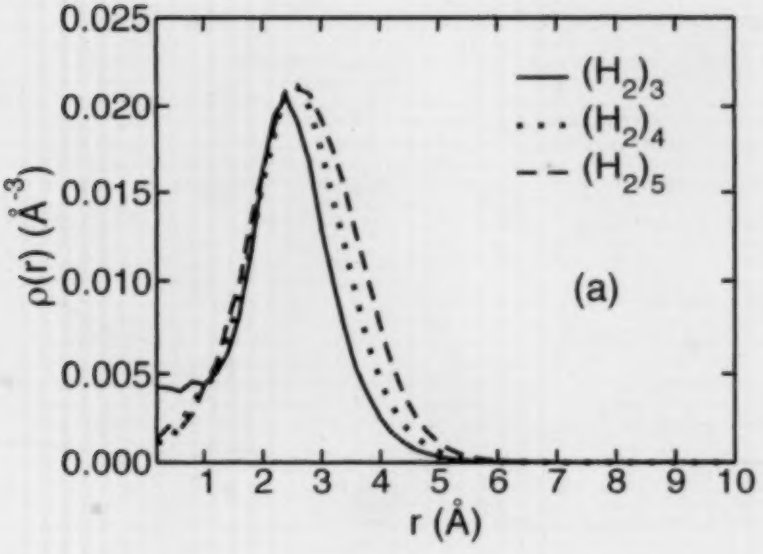
0.025
0.020
0.015
0.010
0.005
0.000
ρ(r) (Å^{-3})
1 2 3 4 5 6 7 8 9 10
r (Å)
(H$_2$)$_3$
(H$_2$)$_4$
(H$_2$)$_5$
(a)

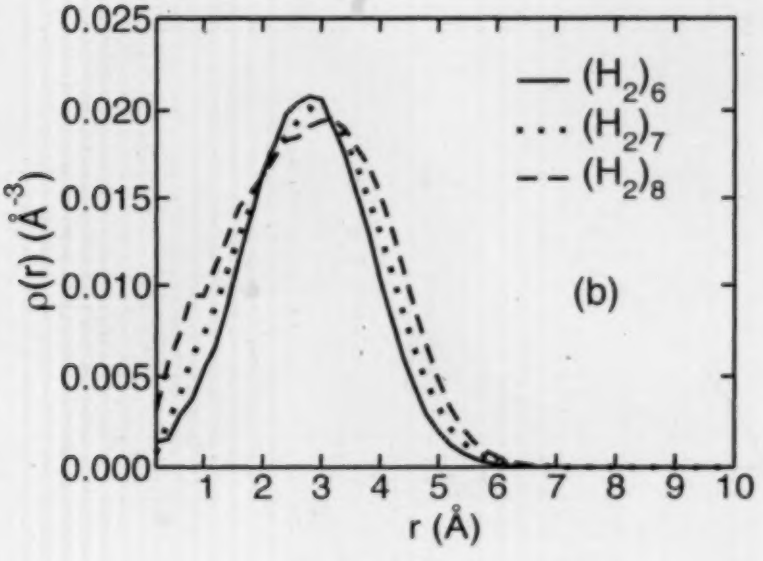
0.025
0.020
0.015
0.010
0.005
0.000
ρ(r) (Å^{-3})
1 2 3 4 5 6 7 8 9 10
r (Å)
(H$_2$)$_6$
(H$_2$)$_7$
(H$_2$)$_8$
(b)

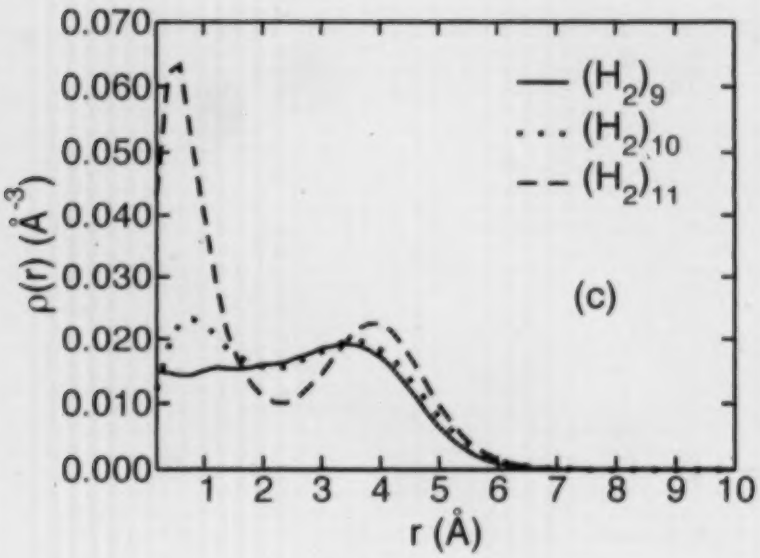
0.070
0.060
0.050
0.040
0.030
0.020
0.010
0.000
ρ(r) (Å^{-3})
1 2 3 4 5 6 7 8 9 10
r (Å)
— $(H_2)_9$
··· $(H_2)_{10}$
– – $(H_2)_{11}$
(c)

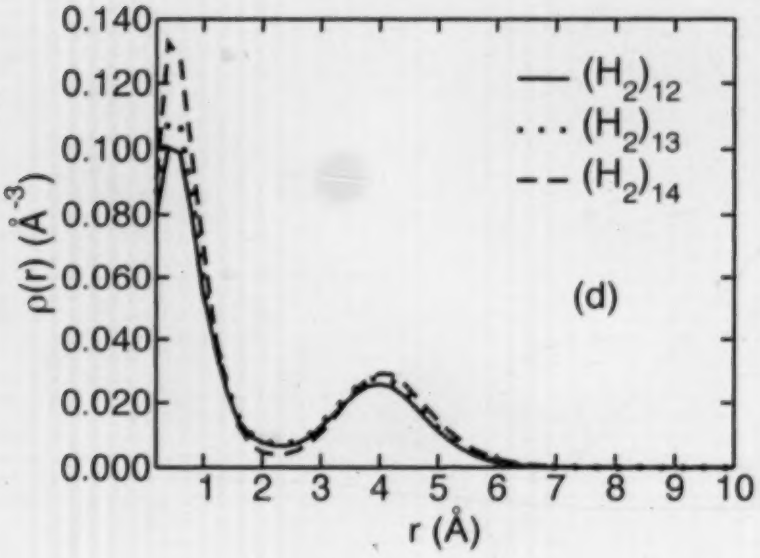
0.140
0.120
0.100
0.080
0.060
0.040
0.020
0.000
ρ(r) (Å^{-3})
1 2 3 4 5 6 7 8 9 10
r (Å)
— $(H_2)_{12}$
··· $(H_2)_{13}$
– – $(H_2)_{14}$
(d)

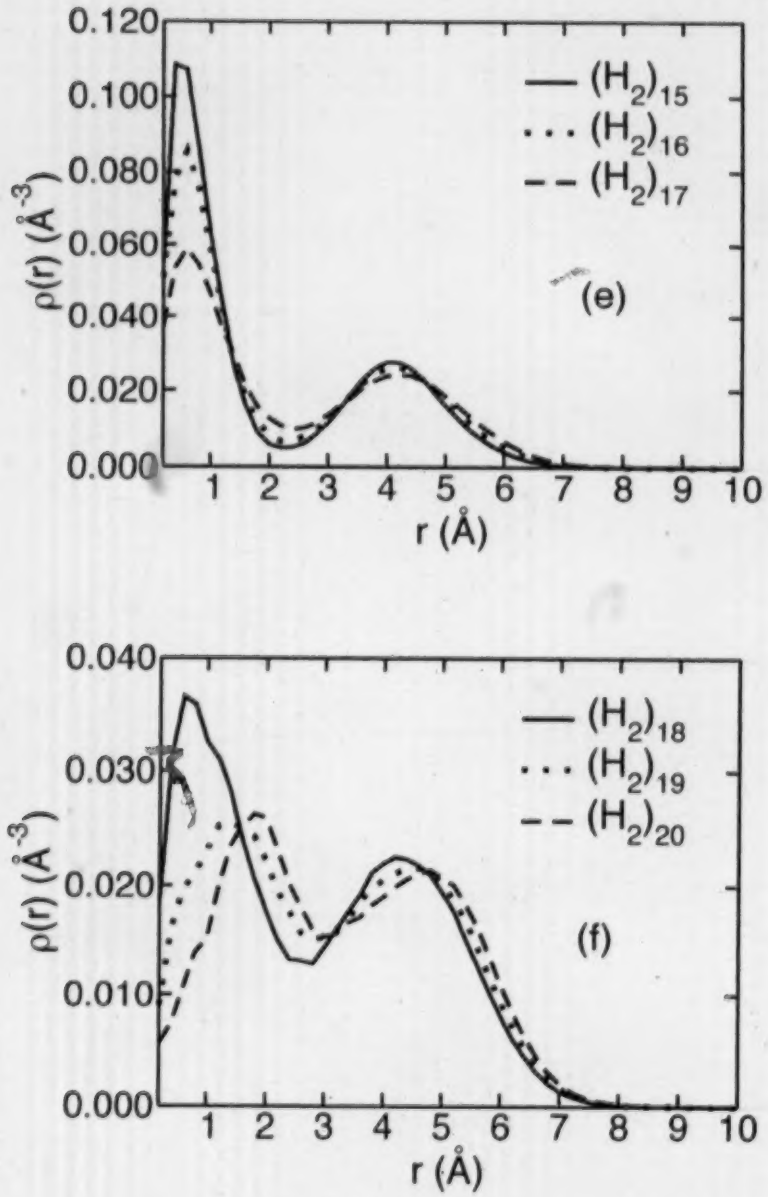

Figure 2.3: Density profiles of various $(para\mathrm{H_2})_N$ clusters obtained from PIGS and the Silvera-Goldman potential (Ref. [75]). The solid, dotted, and dashed lines correspond respectively to: N = 3, 4, 5 (a); N= 6, 7, 8 (b); N= 9, 10, 11 (c); N= 12, 13, 14 (d); N=15, 16, 17 (e); N=18, 19, 20 (f).

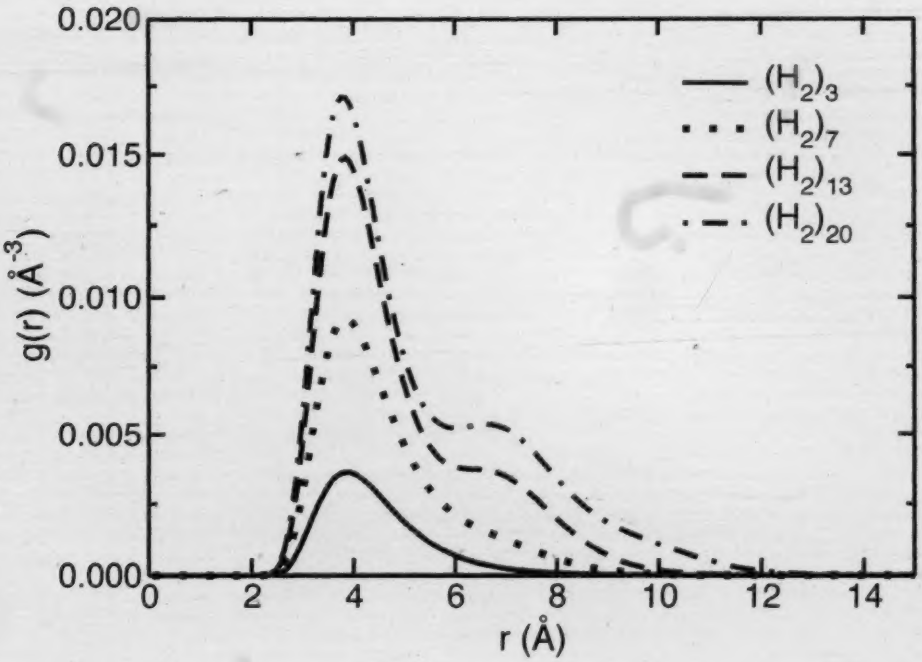

Figure 2.4: Pair distribution function of *para*H_2 clusters calculated using PIGS and the Silvera-Goldman potential (Ref. [75]). The solid, dotted, dashed and dotted-dashed lines correspond respectively to N= 3,7,13,20. The normalization is $4\pi \int_0^\infty g(r) r^2 \mathrm{d}r = (N-1)$.

We finally present an analysis of structural properties based on Pekeris coordinates [85, 86]. This system of coordinates is defined as follows:

$$r_1 = \frac{1}{2}(r_{12} + r_{31} - r_{23}), \tag{2.4}$$

$$r_2 = \frac{1}{2}(r_{12} + r_{23} - r_{13}), \tag{2.5}$$

$$r_3 = \frac{1}{2}(r_{23} + r_{31} - r_{12}), \tag{2.6}$$

where r_{ij} corresponds to the intermolecular distance between molecule i and molecule j. The Pekeris coordinates correspond to the radii of mutually tangent circles centred on each nucleus of a trimer. When the value of one of the coordinates is zero, the trimer has a linear configuration. These coordinates have being used to analyse the bound state wavefunctions of weakly bound bosonic rare gas clusters [82], mixed $^4He_x^{20}Ne_yH$ clusters [83], and the excited states of the half-neon trimer [84]. To perform the analysis, we define a one-dimensional Pekeris distribution function, $d(r_P)$, such that,

$$d(r_P) = \int d\mathbf{R} \mid \Psi(\mathbf{R}) \mid^2 \delta(r_P - r_\alpha(\mathbf{R})) \tag{2.7}$$

where $r_\alpha(\mathbf{R})$ is the dependence of the αth Pekeris coordinate on the system configuration, R. We show in Fig. 2.5 a comparison of the one-dimensional Pekeris distributions obtained using the DVR and the PIGS methods for $N = 3$. The agreement between the PIGS and DVR results is excellent. Contribution of linear configuration is clear in both calculated distributions with non-zero values at r=0. The maximum of the distributions appears at $r \approx 2.2$ Å(Pekeris coordinates) and it decays completely around 8 Å. This agreement is further evidence of the accuracy of the PIGS approach for clusters. For larger clusters, the evolution of "trimers" within the clusters is also shown in Fig 2.5 for N=7,10 and 20. As N increases, the distribution broadens as in the case of the related pair distribution functions of Fig 2.4. We also note that the amplitude at r=0 increases due to greater number of possible of linear trimers.

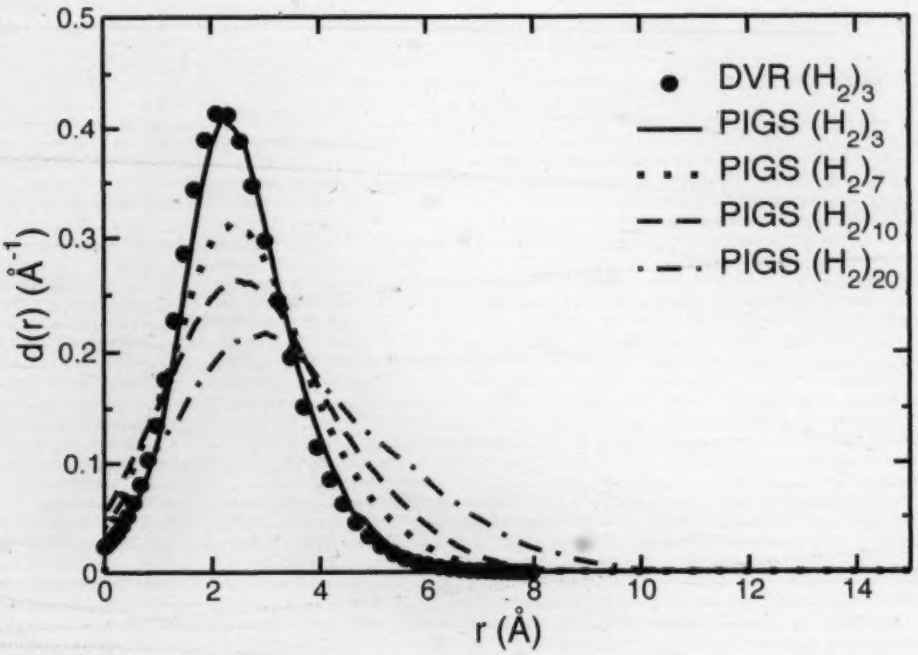

Figure 2.5: One particle distribution function in Pekeris coordinates of *para*H_2 clusters calculated using DVR and PIGS. DVR: filled circles denotes N=3. PIGS: Solid, dotted, dashed and dotted-dashed lines correspond respectively to N= 3,7,10,20.

2.4 Conclusions

We have carried out quantum Monte Carlo calculations of *para*H_2 clusters using (for the first time in this context) the path integral ground state method with a fourth order propagator. A very simple trial wave function was used to showcase the robustness of the approach. Our results are in very good agreement with exact DVR calculation for the dimer and the trimer. We also compared our PIGS results to previous VMC and DMC calculations. Except for the dimer case, existing VMC results are inaccurate for the smaller clusters while DMC results compare favourably to ours. Our calculated structural properties show that small clusters are mostly hollow and that the centre of larger clusters progressively fills up to reach a density maximum at $N = 14$. The density near the centre-of-mass decreases again in the $N = 15$–20 size range, an indication of a structural change. The analysis of the size dependence of the chemical potential is consistent with the previous observation that clusters with $N = 13$ are stabilized [27, 38]. The use of Pekeris coordinate allows us to study the importance of linear configurations and further test the accuracy of the PIGS method. Although new insight of the energetics and structure of *para*H_2 clusters has been gained through this investigation, different questions can be also asked. In particular, very little has been said about the physical state of these systems, i.e. whether hydrogen clusters are solid- or liquid-like. Similarly, the structure of these clusters can be described to a higher level of detail. The following Chapter is devoted to answer precisely these questions.

Chapter 3

Rigid-liquid behavior of pure quantum clusters

In this Chapter we extend our previous work by studying pristine clusters of $(para\mathrm{H}_2)_N$ and $(ortho\mathrm{D}_2)_N$ of size ranging from $N = 11$ to 55 molecules. The chemical potential is calculated for two different interaction models and we show that the location of magic numbers is sensitive to the choice of interaction potential. Density profiles are calculated and they reveal the difference between the two isotopes with regard to shell structure. We aim to characterize these systems in terms of their solid- and/or liquid-like behaviour. The magnitude of relative pair-distance and position fluctuations is used to asses the rigidity of these finite-size quantum systems. We propose as a probe of the onset of rigidity in the clusters the difference between the generic and specific distance fluctuations. We find that smaller $(para\mathrm{H}_2)_N$ clusters are fluid-like and start to display increased rigidity for clusters of size $N \geq 26$, whereas $(ortho\mathrm{D}_2)_N$ clusters of $N = 13$ and $N \geq 19$ are rigid. Small clusters exhibit structures loosely based on an anti-Mackay icosahedral motif. Finally, we suggest a transition from anti-Mackay to Mackay structure at N=41-42.[1]

[1]The results presented in this chapter have appeared in an article entitled: *On the solid- and liquidlike nature of quantum clusters in their ground state* Reused with permission from Javier Eduardo Cuervo and Pierre-Nicholas Roy, The Journal of Chemical Physics **128**, 224509 (2008). Copyright 2008 American Institute of Physics.

3.1 Introduction

Solid and liquid phases, along with transitions between them have been extensively studied in the bulk. Analogously, it is of great interest to characterize the liquid-like or solid-like nature of finite size systems. In this context, "solids" show order and localization, reminiscent of a crystal, on a scale comparable to their size. Conversely, "liquids" are homogeneous and isotropic systems characterized by the lack of long range order. In small clusters, most of the particles are located at the surface, giving rise to unusual properties and behaviour when compared to bulk matter. For example, finite size systems have a very complex multidimensional potential energy landscape. This richness of inherent structures [4] allows for multiple structural transformations, even at low temperatures. These characteristics make the study of transitions between stable and metastable structures an important challenge. Proykova and Berry [3] have recently reviewed these issues extensively. When the quantum nature of clusters is taken into account, additional challenges arise, such as particle exchange, and large amplitude zero point motion (ZPM). To investigate the question of whether quantum clusters display solid- or liquid-like character, we have chosen the Bosonic isotopes of the hydrogen molecule: *para*H_2 and *ortho*D_2.

As previously stated in this thesis, small *para*H_2 clusters have recently been the focus of many studies, both theoretical [87, 51, 45, 44, 52, 50, 47, 53] and experimental [55]. The current interest in these clusters rests upon the fact that, besides the isotopes of He, they are the only systems expected to display superfluidity [23].

Nonetheless, the relationship between the structure of hydrogen clusters and the non-monotonic behaviour observed in the size evolution of their calculated superfluid (SF) fraction is still a matter of debate [51, 52, 50, 53]. Recent ground state studies by Guardiola and Navarro [45, 47] suggested that clusters of $(para\mathrm{H}_2)_N$ of $3 \leq N \leq 50$ exhibit a clear geometrical order, with molecules distributed in spherical coronas. However, it is not clear whether the molecules within these shells behave as a liquid or a solid.

In this Chapter, we continue our study of the ground state structure of pure

$(para\mathrm{H}_2)_N$ and extend this study to the heavier isotope $(ortho\mathrm{D}_2)_N$, this time aiming to characterize these systems in terms of their rigidity. To gain a deeper understanding of the size-dependent energetics and structure of these clusters, we examined their chemical potential, relative bond-length fluctuations [88, 89, 3, 90], the relative distance to the centre-of-mass fluctuations, and the bond order parameters (BOP) [91, 92]. The rest of this Chapter is organized as follows: in section 3.2 we briefly describe the computational methodology. We present and discuss our results in Section 3.3. Conclusions are presented in Section 3.4.

3.2 Methodology

We use the variational path integral method (VPI), also known as path integral ground state (PIGS)[56] as described in Section 1.3.1. The mass of the $para\mathrm{H}_2$ and $ortho\mathrm{D}_2$ molecules we use are 2.0156500642 a.m.u. and 4.028203556 a.m.u., respectively. Two models of interaction are considered to describe molecular hydrogen and deuterium: the Silvera-Goldman [75] and the Buck [76] pair potentials. The trial wave function we use is described in Eq. 4.1 with a pseudopotential given by Eq. 4.2. We have shown that this trial wave function yields converged results using our methodology [44]. The computational approach is identical to that of Ref. [44]; note that all the calculations presented below use an imaginary time step of $\tau = 0.0015625$ K^{-1} and a projection time of $\beta = 0.8$ K^{-1}.

3.3 Results and Discussion

3.3.1 Energetics

Tables 3.1 and 3.2 contain the energy per particle of $(para\mathrm{H}_2)_N$ and $(ortho\mathrm{D}_2)_N$ clusters for both potential models. In Fig. 3.1 we show the difference in the energy per particle between our results and those obtained by Guardiola *et al.* [47]. Small discrepancies can be observed. The PIGS energies per particle are always more negative than those obtained by DMC regardless of the potential model used. The observed discrepancies may be due to population-control biasing in the DMC calculations.

Table 3.1: Ground state energies per molecule ($e(N)$) (in K) of *para*H_2 and *ortho*D_2 clusters obtained for the Silvera-Goldman potential (a) (Ref. [75]) and Buck potential (b) (Ref. [76]) using PIGS (N=11-35). Uncertainties appear in parentheses.

Cluster size	*para*$H_2{}^a$	*para*$H_2{}^b$	*ortho*$D_2{}^a$	*ortho*$D_2{}^b$
11	-18.54(2)	-20.22(3)	-33.03(3)	-36.33(3)
12	-19.77(2)	-21.68(3)	-35.63(3)	-39.06(3)
13	-21.10(2)	-23.03(3)	-38.93(3)	-42.87(3)
14	-22.00(2)	-24.04(1)	-39.30(3)	-43.25(3)
15	-22.87(2)	-24.93(1)	-40.23(3)	-44.20(3)
16	-23.65(2)	-25.72(1)	-41.12(3)	-45.28(3)
17	-24.31(2)	-26.49(1)	-42.04(3)	-46.37(3)
18	-25.05(2)	-27.23(1)	-43.61(3)	-47.88(3)
19	-25.73(2)	-28.01(1)	-45.79(3)	-50.13(3)
20	-26.40(2)	-28.69(1)	-46.44(3)	-50.90(3)
21	-27.08(2)	-29.39(1)	-46.99(3)	-51.59(3)
22	-27.61(2)	-30.05(1)	-48.16(3)	-52.77(3)
23	-28.27(2)	-30.72(1)	-49.64(3)	-53.66(3)
24	-28.83(2)	-31.34(1)	-50.23(3)	-54.94(3)
25	-29.41(2)	-31.93(1)	-51.13(3)	-55.90(3)
26	-29.96(2)	-32.63(1)	-52.60(3)	-57.47(3)
27	-30.51(2)	-33.08(1)	-52.87(3)	-57.78(3)
28	-30.94(2)	-33.61(2)	-53.48(3)	-58.37(3)
29	-31.40(2)	-34.22(1)	-53.59(3)	-58.52(3)
30	-31.83(2)	-34.56(1)	-54.80(3)	-59.38(3)
31	-32.23(2)	-34.97(1)	-55.33(3)	-60.42(3)
32	-32.63(2)	-35.43(1)	-55.63(3)	-60.46(3)
33	-33.06(2)	-35.98(1)	-56.69(3)	-61.91(3)
34	-33.68(2)	-36.64(1)	-56.55(3)	-62.11(3)
35	-33.89(2)	-36.90(1)	-57.26(3)	-63.04(3)

Table 3.2: Ground state energies per molecule ($e(N)$) (in K) of *para*H_2 and *ortho*D_2 clusters obtained for the Silvera-Goldman potential (*a*) (Ref. [75]) and Buck potential (*b*) (Ref. [76]) using PIGS (N=36-55). Uncertainties appear in parentheses.

Cluster size	*para*$H_2{}^a$	*para*$H_2{}^b$	*ortho*$D_2{}^a$	*ortho*$D_2{}^b$
36	-34.20(2)	-37.10(1)	-58.02(3)	-63.25(3)
37	-34.49(2)	-37.48(1)	-58.43(3)	-63.88(3)
38	-34.82(2)	-37.87(1)	-59.04(3)	-64.31(3)
39	-35.24(2)	-38.27(1)	-59.08(3)	-65.00(3)
40	-35.55(2)	-38.47(2)	-59.63(3)	-65.40(3)
41	-36.05(2)	-39.16(3)	-61.80(3)	-65.44(4)
42	-36.40(3)	-39.59(3)	-62.42(3)	-66.54(5)
43	-36.84(3)	-39.93(3)	-61.99(2)	-66.99(3)
44	-37.16(2)	-40.27(3)	-63.24(3)	-67.41(5)
45	-37.52(2)	-40.62(3)	-63.64(3)	-66.85(4)
46	-37.75(3)	-40.84(3)	-63.68(3)	-67.74(3)
47	-37.94(2)	-41.11(3)	-63.49(3)	-68.23(3)
48	-38.22(3)	-41.41(3)	-64.41(3)	-68.65(3)
49	-38.44(3)	-41.70(3)	-64.20(5)	-69.04(3)
50	-38.68(3)	-41.89(3)	-64.38(3)	-68.65(3)
51	-38.91(2)	-42.12(3)	-64.62(3)	-69.94(3)
52	-39.08(2)	-42.26(3)	-65.62(3)	-70.51(5)
53	-39.31(2)	-42.69(2)	-66.58(3)	-69.84(3)
54	-39.53(3)	-42.86(3)	-66.79(5)	-70.94(3)
55	-39.79(2)	-43.03(2)	-67.09(3)	-71.53(5)

In an independent DMC study, which employed a somewhat different guiding function than that used in Ref. [47], it was found that the energy per particle of para-hydrogen clusters with N=23 can change by up to 0.2K when the number of walkers is increased from 1000 to 4000 [93]. The chemical potential, as defined in Section 2.3.1, is shown in Fig. 3.2 for (*para*$H_2)_N$ (both potentials). The chemical potential curves agree very well with those of Ref. [47] up to N=25 for the Buck model and up to N=33 for the Silvera-Goldman potential. We observed that N = 13 is a magic cluster for both models. For larger clusters, the agreement deteriorates. We observe additional pronounced magic numbers at N =26, 29, 34, 39, 41 and 53 for the Buck potential and at N=34, 39 and 41 in the case of Silvera-Goldman

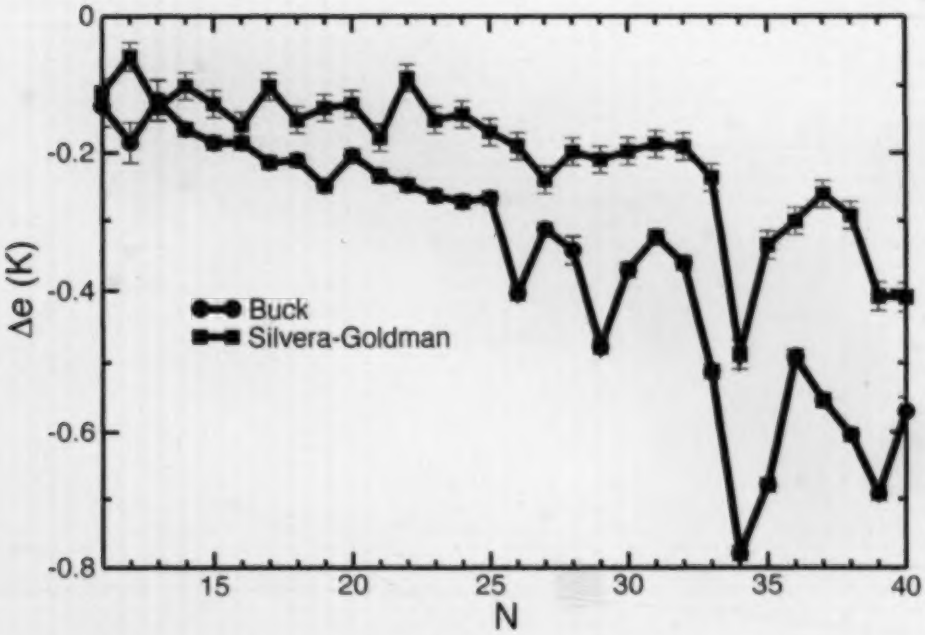

Figure 3.1: Difference in the energy per particle of *para*Hydrogen clusters (Δe) (in K) defined as the results of this work minus those of Ref. [47] as a function of N using Buck potential (filled circles) (Ref. [76]) and Silvera-Goldman potential (squares) (Ref. [75]). When not shown, error bars are within the size of the symbols. Solid lines are only guides to the eye.

interaction model. Our findings agree qualitatively with the finite temperature results of Mezzacapo *et al.* [53] in that we both report a less monotonic chemical potential curve compared to Guardiola *et al.* [47]. We found that in the ground state the appearance of magic numbers depends on the choice of interaction model. This is in disagreement with the finite temperature results of Khairallah *et al.* [50]. When the Silvera-Goldman potential is used, fewer peaks in the chemical potential curve were found. Compared to the path integral Monte Carlo (PIMC) results in Ref. [50], five of the magic numbers are missing in the ground state.

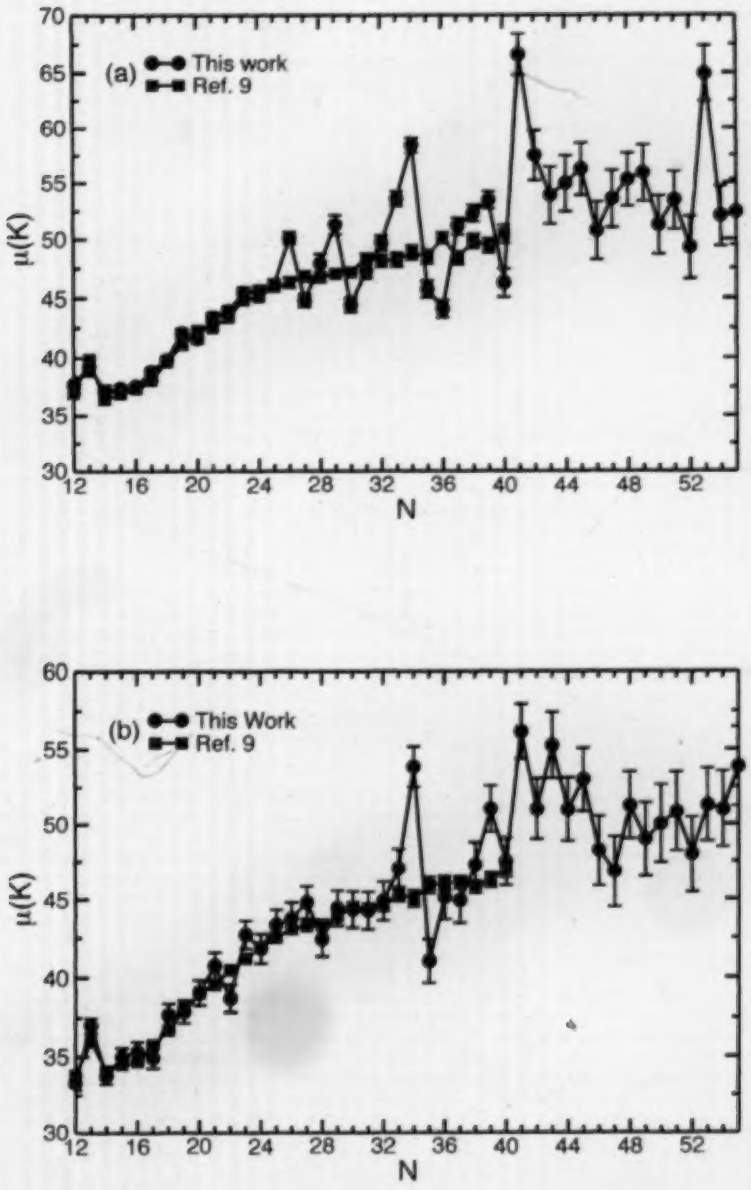

Figure 3.2: Chemical potential (μ) as a function of N of *para*Hydrogen clusters (filled circles) using Buck potential (a) (Ref. [76]) and Silvera-Goldman potential (b) (Ref. [75]). Results from Guardiola and Navarro (Ref. [47]) (squares) are also shown. When not shown, error bars are within the size of the symbols. Solid lines are only guides to the eye.

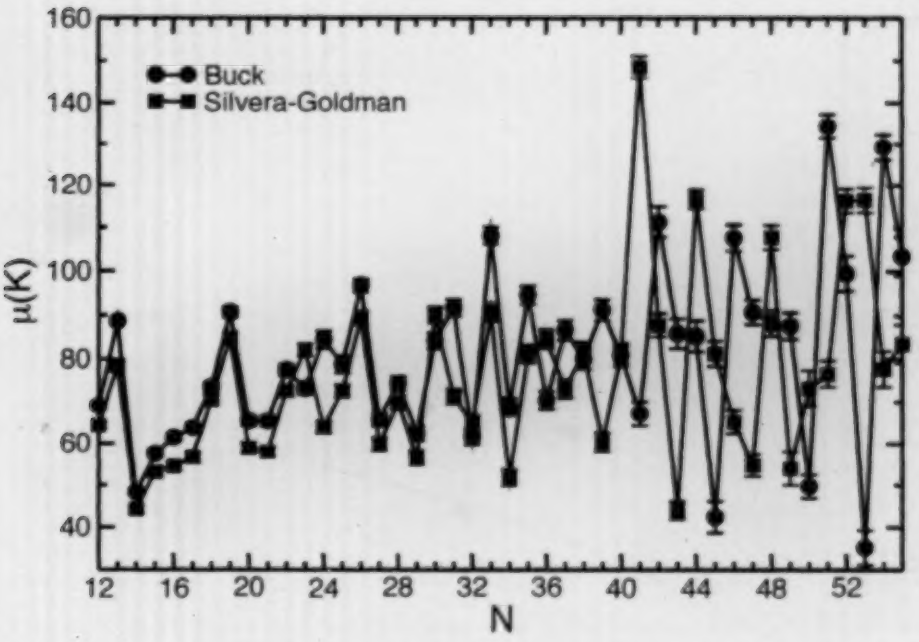

Figure 3.3: Chemical potential (μ) as a function of N of *ortho*Deuterium clusters using Buck potential (Ref. [76]) (filled circles) and Silvera-Goldman potential (Ref. [75]) (squares). When not shown, error bars are within the size of the symbols. Solid lines are only guides to the eye.

We propose that these otherwise magic clusters undergo quantum melting [51] in the ground state. Additionally, the chemical potential curve of $(ortho\mathrm{D}_2)_N$ clusters is shown in Fig. 3.3. We first notice a far richer chemical potential curve in terms of magic numbers for both potentials. The second most important difference is the range of chemical potentials that spans over 60 K, whereas in the case of $para\mathrm{H}_2$ the range is only 30 K. In the case of the Buck potential, the most pronounced peaks correspond to magic numbers $N = 13$, 26, and 33. Smaller peaks are at $N = 22$, 24, 28, 31, 35, 37 and 39. On the other hand, magic numbers for the Silvera-Goldman potential are $N = 13$, 19, 23, 26, 30, 36 and smaller peaks appear at $N = 28$ and 38. Most of the

magic numbers that are observed for both isotopes, and the two different potentials, correspond to the proposed [6, 94] hierarchical structures made of icosahedra (IC) and interpenetrated double icosahedra (DIC) (N = 13, 19, 23, 26, 29, 32, 34, 36) and octahedron (N= 38) and have been observed in classical Lennard-Jones clusters [94] and PIMC calculations of $(para\mathrm{H_2})_N$ [52, 50].

Unexpected magic numbers (N = 22, 24, 30, 31, 33, 35, 37, 39 and in the case of $para\mathrm{H_2}$ N=41) can be interpreted as a departure from the icosahedral symmetry, where relatively more stable alternatives such as carved face centred cubic (fcc) and hexagonal closed packed (hcp) lattice-like structures can be favoured. In particular, the appearance of hcp lattice-like structures would not be surprising, since this is the equilibrium lattice structure of the bulk. This overall richness of magic $(ortho\mathrm{D_2})_N$ clusters compared to their lighter isotopes reflect their more localized and rigid nature. Quantum melting is therefore not expected to occur in the ground state for the heavier isotope. We finally note that in the $N < 13$ range, the heavy and light isotopes have a similar chemical potential curve as observed in earlier work on HF doped $(para\mathrm{H_2})_N$ clusters [95].

3.3.2 Structure

We have seen in section 3.3.1, that the chemical potential is very sensitive to the interaction model for the larger clusters. We do not observe such a strong model dependence in the structural properties. Small differences were observed, but in none of the cases did they lead to drastically different conclusions to those drawn below. The structural properties presented in this section are based on simulations performed using the Buck potential [76].

To gain a better understanding of the differences between a highly quantum system and its more classical counterpart, we compare the density profile ($\rho(r)$) of $(para\mathrm{H_2})_N$ and $(ortho\mathrm{D_2})_N$ at different N. Fig. 3.4 shows $\rho(r)$ for N = 13, 19, 23, 26, 28, 29, 33, 34, 38, 39, 41 and 55. The general feature of $(ortho\mathrm{D_2})_N$ clusters is a more structured and solid-like density profile compared to $(para\mathrm{H_2})_N$. For N = 13 in particular, the density goes to zero at the first minimum ($r \approx 2$ Å), a clear sign of increased order

and localization when compared to $(para\mathrm{H_2})_{13}$. At $N = 19$, the $\rho(r)$ of $(ortho\mathrm{D_2})_N$ displays three large narrow peaks and zero density at the centre of the cluster, consistent with a DIC structure. On the other hand, the lighter $(para\mathrm{H_2})_{19}$ cluster displays finite density at the centre-of-mass and two wide and shallow peaks, consistent with a more liquid-like structure. The $\rho(r)$ of $(para\mathrm{H_2})_{23,26,28,29}$ are very similar with no density at the centre-of-mass and two broad peaks. Similarly, $(ortho\mathrm{D_2})_{23,26,28}$ clusters have the same above features. The main difference being narrower and larger peaks at $r \approx 2$ Å and a small splitting of the second peak at $r \approx 4.8$ Å. The $(ortho\mathrm{D_2})_{26}$ cluster shows a more localized structure and a very small value is observed at the first minimum of its density profile. The density profile of $(ortho\mathrm{D_2})_{29}$ is similar to that of $(ortho\mathrm{D_2})_{19}$, with the addition of what it appears to be a shoulder that starts to develop at $r \approx 6$ Å. Similar features are observed in $(ortho\mathrm{D_2})_{33}$. On the other hand $(para\mathrm{H_2})_{33}$ only displays two broad peaks that suggest a more liquid-like structure. The $(ortho\mathrm{D_2})_{34}$ cluster shows two large and narrow peaks at short distances and two small peaks at larger distances. Its $(para\mathrm{H_2})_{34}$ counterpart shows similar features, but its more liquid-like character is evident in that the cluster is less compact, however, a deeper minimum is observed between the second and third peak, that suggest a relatively low particle flow between these "shells". This feature is also consistent with the appearance of a magic cluster a N=34 present for both interaction models. At this point it is worth to mention that the Lennard-Jones cluster N=38 has an octahedral equilibrium structure.[94] Similarly, the density profile of $(ortho\mathrm{D_2})_{38}$ shows a major structural change compared to smaller clusters. It shows a sharp peak at $r \approx 1$ Å and the first minimum of almost zero density at ≈ 2 Å. Two additional broader peaks are located at ≈ 3 and 6 Å. These features can be reconciled with an octahedral structure. The $(para\mathrm{H_2})_{38}$ cluster shows a much more liquid-like structure. The density profile suggest what it could be a loose octahedral structure: three short and wide peaks at slightly larger distances compare to those of $(ortho\mathrm{D_2})_{38}$. Similar features are observed in $(para\mathrm{H_2})_{39}$. The $(ortho\mathrm{D_2})_{39}$ cluster no longer displays a density profile compatible with an octahedral structure (no density at very short distance from the centre-of-mass). This suggest a return to the icosahedral-based

structure observed in the Lennard-Jones cluster N=39 [94]. The clusters with N= 41 show interesting differences. The density profile of $(para\mathrm{H_2})_{41}$ shows what it would be a solid-like structure with density at the centre-of-mass and two peaks.

On the other hand the heavier isotope $(ortho\mathrm{D_2})_{41}$ displays a density profile with three peaks and a small shoulder. From N=42 and on, both isotopes present density profiles similar to that of N=55. They display a large value of density at the centre-of-mass, zero density at $\approx$ 2 Å and two peaks at $\approx$ 4 and 6.5 Å consistent with a much more solid-like character. Although N=55 does not appear to be a magic number, this is the number of particles needed to complete a second solvation shell. These two shells are confirmed by the density profile. On the other hand, a rather large density at the centre-of-mass is more consistent with a core made of an icosahedron of 13 particles rather than the 19 particles DIC core expected of a anti-Mackay layering. We suggest an anti-Mackay to Mackay transition at N=42. It is worth to mention that a structure based on a carved hcp lattice is also consistent with the features mentioned above, therefore one should not completely rule-out the possibility that at this size these clusters start to have an structure more reminiscent of the bulk.

Density profiles provide only a qualitative indication of the physical state of the clusters. In the absence of accurate first principles theories of melting, the Lindemann melting criterion[96] has proven to be extremely useful. It states that a solid melts when the relative root mean square (RMS) bond-length fluctuations (δ_L) exceeds a critical value, often taken as 15% [90].

In this work we use the following definition of δ_L:

$$\delta_L = \frac{2}{N(N-1)} \sum_{i<j} \frac{(\langle r_{ij}^2 \rangle - \langle r_{ij} \rangle^2)^{1/2}}{\langle r_{ij} \rangle}, \tag{3.1}$$

where r_{ij} is the distance between particles i and j. Similarly, we defined the "generic" RMS bond-length fluctuation (δ_{L^g}) as:

$$\delta_{L^g} = \frac{(\langle r^2 \rangle - \langle r \rangle^2)^{1/2}}{\langle r \rangle}, \tag{3.2}$$

where the $\langle \cdots \rangle$ denotes the average over all particles pairs within a cluster. In the recent literature, Chakravarty *et al.* [90] have used a modification of the Lindemann

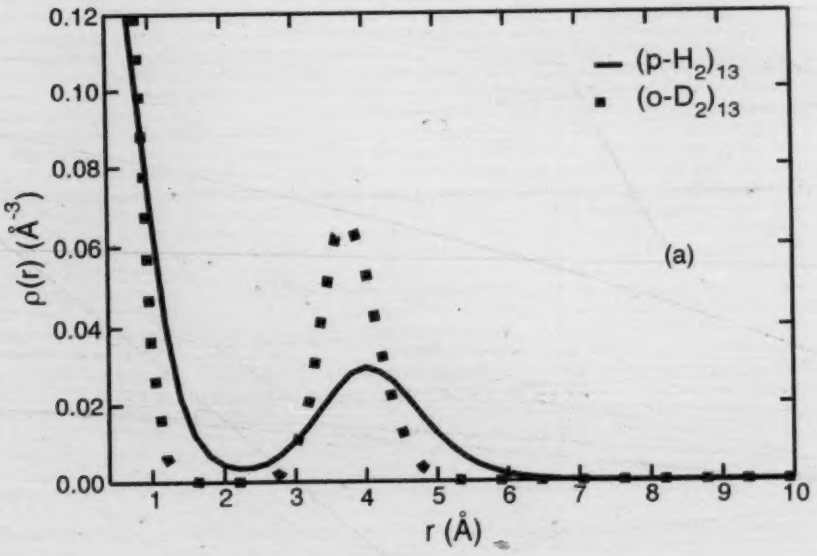
0.12
0.10
0.08
0.06
0.04
0.02
0.00
ρ(r) (Å^{-3})
1
2
3
4
5
6
7
8
9
10
r (Å)
(p-H$_2$)$_{13}$
(o-D$_2$)$_{13}$
(a)

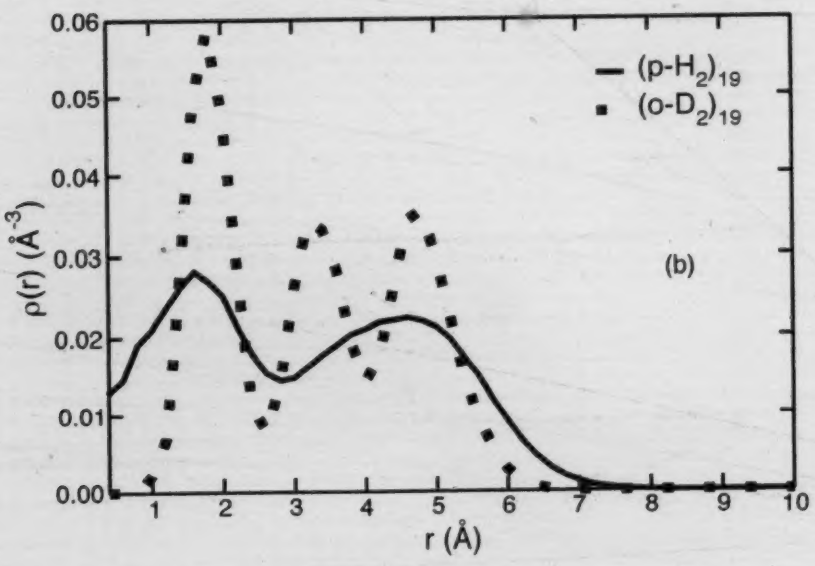
0.06
0.05
0.04
0.03
0.02
0.01
0.00
ρ(r) (Å^{-3})
1
2
3
4
5
6
7
8
9
10
r (Å)
(p-H$_2$)$_{19}$
(o-D$_2$)$_{19}$
(b)

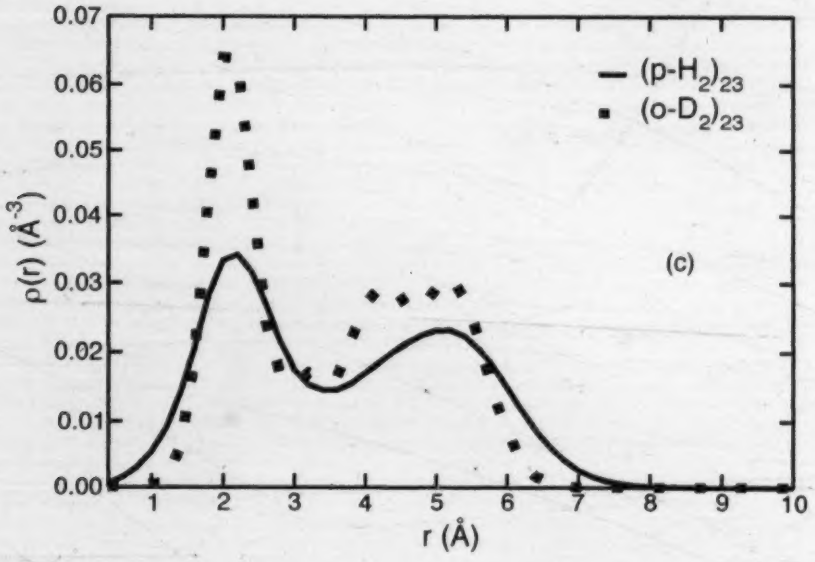
0.07
0.06
0.05
0.04
0.03
0.02
0.01
0.00
ρ(r) (Å^{-3})
1
2
3
4
5
6
7
8
9
10
r (Å)
(p-H$_2$)$_{23}$
(o-D$_2$)$_{23}$
(c)

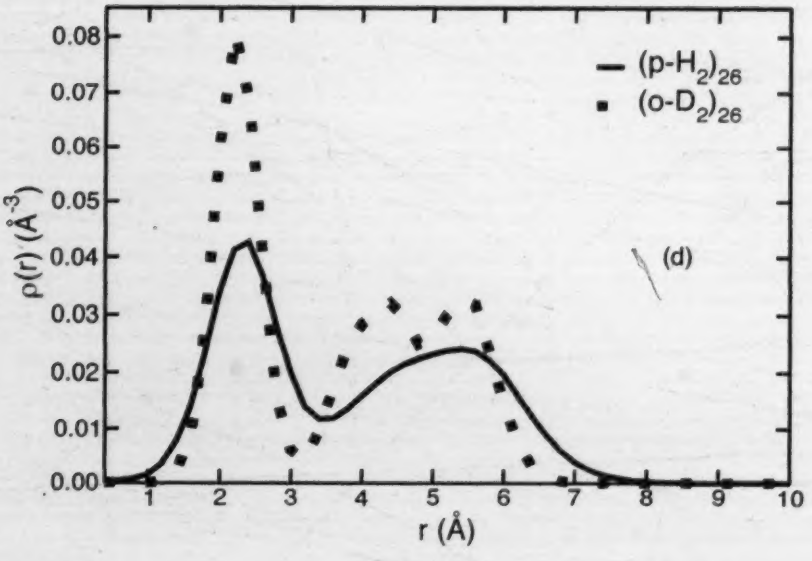
0.08
0.07
0.06
0.05
0.04
0.03
0.02
0.01
0.00
ρ(r) (Å^{-3})
1
2
3
4
5
6
7
8
9
10
r (Å)
(p-H$_2$)$_{26}$
(o-D$_2$)$_{26}$
(d)

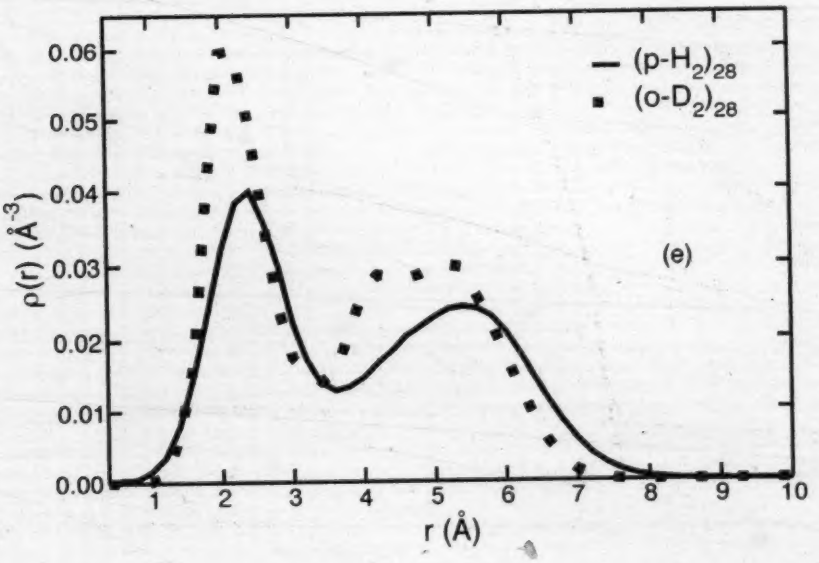
0.06
0.05
0.04
0.03
0.02
0.01
0.00
ρ(r) (Å^{-3})
1
2
3
4
5
6
7
8
9
10
r (Å)
(p-H$_2$)$_{28}$
(o-D$_2$)$_{28}$
(e)

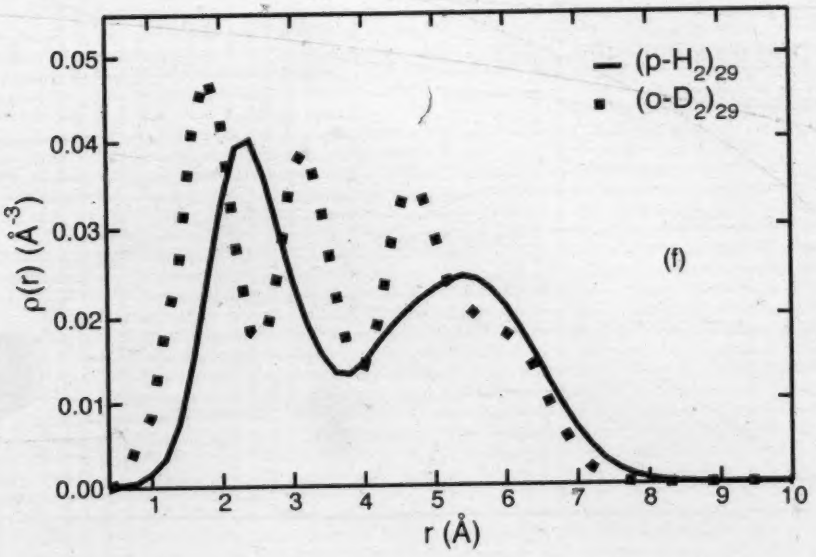
0.05
0.04
0.03
0.02
0.01
0.00
ρ(r) (Å^{-3})
1
2
3
4
5
6
7
8
9
10
r (Å)
(p-H$_2$)$_{29}$
(o-D$_2$)$_{29}$
(f)

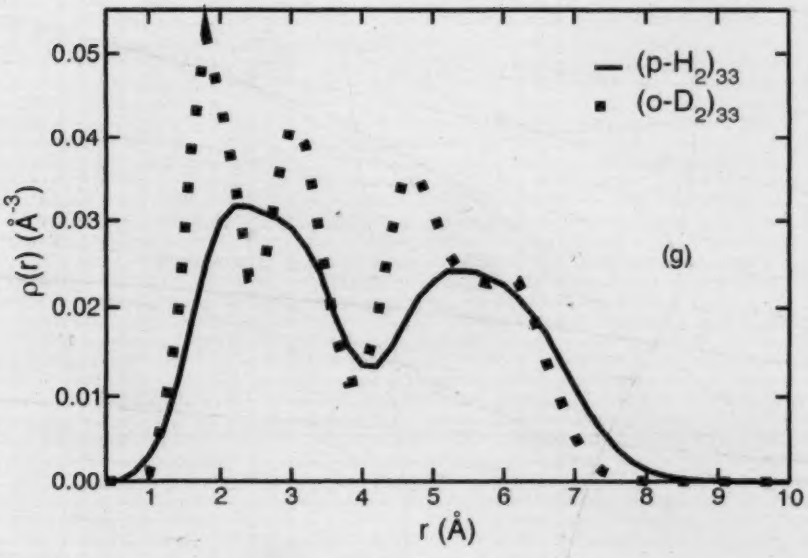
0.05
0.04
0.03
0.02
0.01
0.00
ρ(r) (Å^{-3})
1
2
3
4
5
6
7
8
9
10
r (Å)
(p-H$_2$)$_{33}$
(o-D$_2$)$_{33}$
(g)

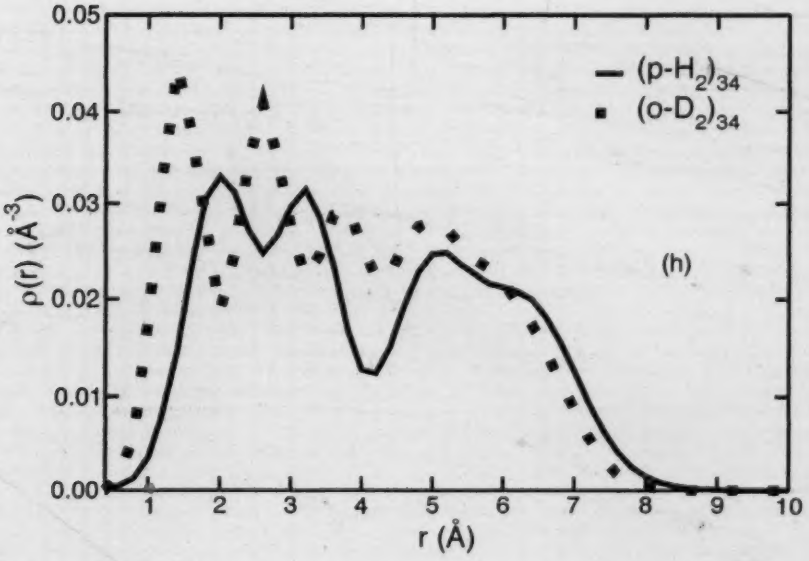
0.05
0.04
0.03
0.02
0.01
0.00
ρ(r) (Å^{-3})
1
2
3
4
5
6
7
8
9
10
r (Å)
(p-H$_2$)$_{34}$
(o-D$_2$)$_{34}$
(h)

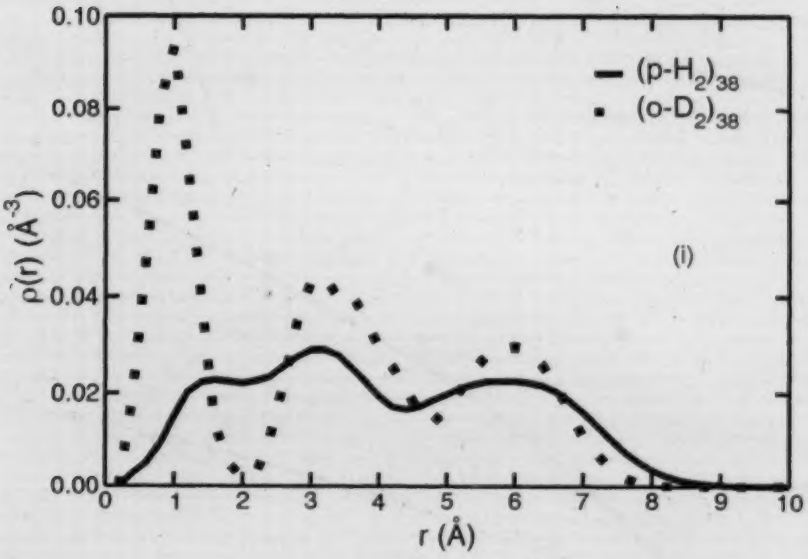
0.10
0.08
0.06
0.04
0.02
0.00
ρ(r) (Å^{-3})
0
1
2
3
4
5
6
7
8
9
10
r (Å)
(p-H$_2$)$_{38}$
(o-D$_2$)$_{38}$
(i)

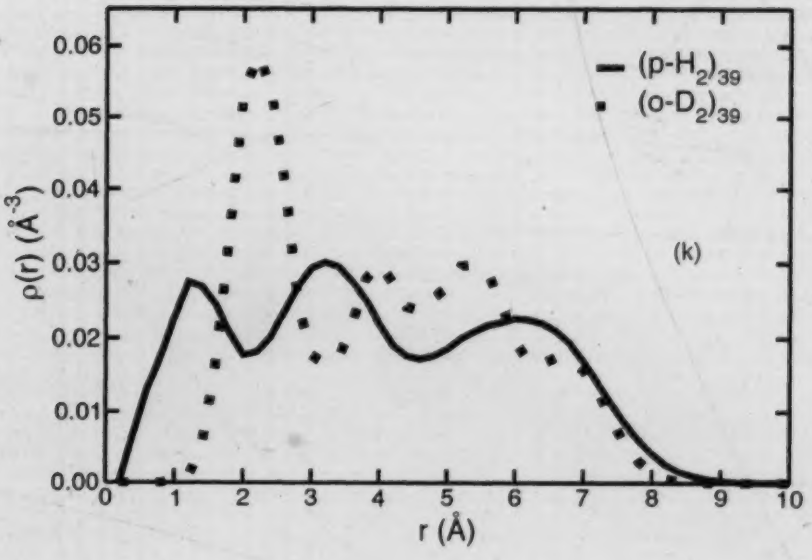
0.06
0.05
0.04
0.03
0.02
0.01
0.00
ρ(r) (Å^{-3})
0
1
2
3
4
5
6
7
8
9
10
r (Å)
(p-H$_2$)$_{39}$
(o-D$_2$)$_{39}$
(k)

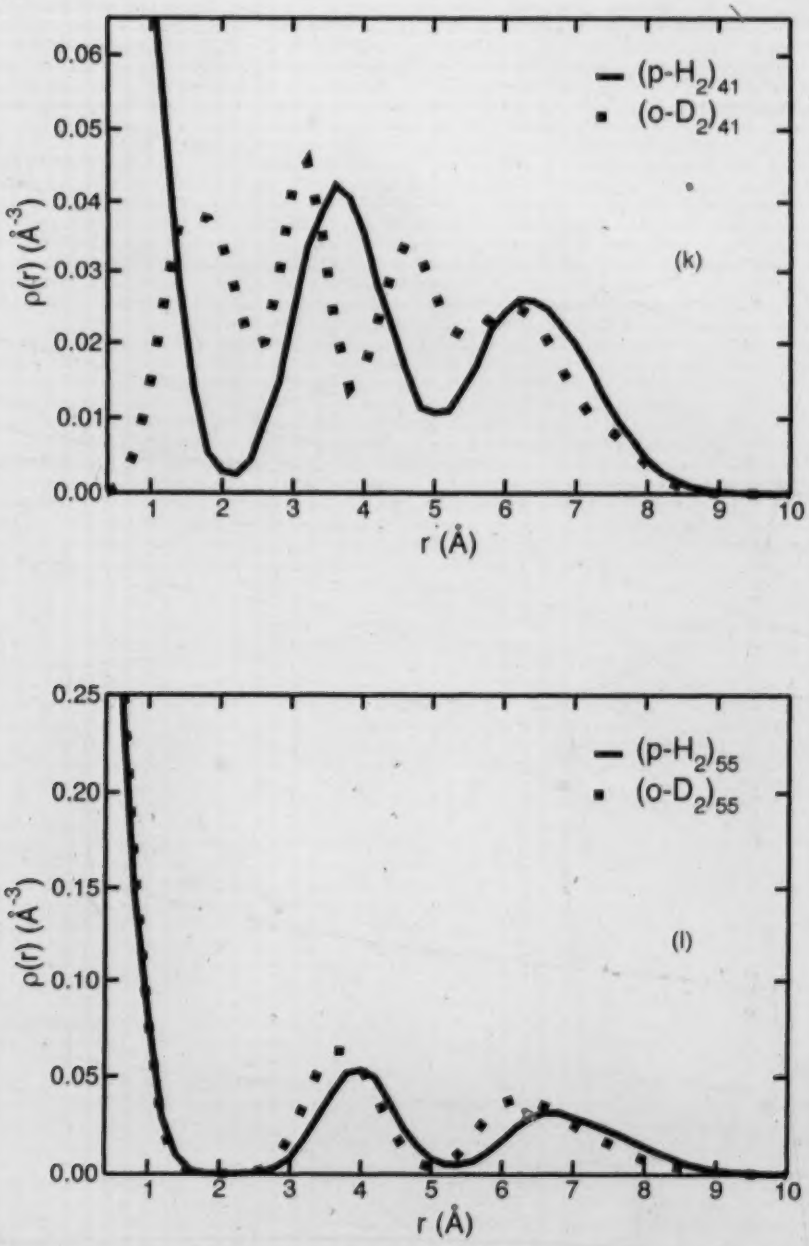

Figure 3.4: Density profile of $(para\mathrm{H}_2)_N$ (solid line) and $(ortho\mathrm{D}_2)_N$ (dotted line), N =13 (a), 19 (b), 23 (c), 26 (d), 28 (e), 29 (f), 33 (g), 34 (h), 38 (i), 39(j) 41(k), 55(l).

index related to the concept of inherent structures,[4] the return distance of inherent structures (RDIS), to study the solid-liquid phase transition in classical bulk matter.

Fig. 3.5 depicts both δ_L and δ_{L^g} as a function of cluster size for $(para\mathrm{H}_2)_N$ and $(ortho\mathrm{D}_2)_N$. In the case of $para\mathrm{H}_2$, one notices that both quantities are always larger than 0.28 up to N=40. Based on the Lindemann criterion, one should refer to the clusters in the size range as liquid systems. Although their density profiles clearly show shell structures, fluctuations indicate that within and in between these shells the molecules have a mobility characteristic of liquid phase systems.

Interestingly, there is a departure of the generic fluctuations from the specific ones at $N = 26$ in the case $para\mathrm{H}_2$ clusters. This is the same cluster size at which the superfluid fraction at finite temperature gets abruptly quenched.[51, 52, 50] From this size on, the value of the specific fluctuations is smaller than its generic counterpart. The system appears to behave as a liquid due to large zero point motion, but exhibits increased rigidity. This behaviour can be correlated with the suppression of quantum permutations and decreased superfluid response at finite temperature.[51, 52, 50] For N=41-45,53, $para\mathrm{H}_2$ clusters should be regarded as rigid. This is consistent with the previous observation based on the density profile (and a magic number at N=41) that $para\mathrm{H}_2$ clusters become more solid like. The larger clusters show a vastly different behaviour of the specific vs. the generic fluctuations, but the value of δ_L still suggest a liquid-like character.

A different behaviour is observed in $ortho\mathrm{D}_2$ clusters. In general, these clusters display generic fluctuations that are always larger than the specific ones. This is very noticeable at N =13 and $N \geq 19$ where δ_L is always < 0.15, whereas the generic fluctuations are always over 0.25. These clusters can be considered solid-like.

This small magnitude of fluctuations for $N \geq 19$ is consistent with the very small finite temperature superfluid fractions observed for clusters with $N > 17$.[52] We also observe that the depressions in δ_L coincide with the magic numbers in the chemical potential of Fig. 3.3.

The relative RMS distance from the centre-of-mass fluctuations δ_{rcm} are shown in

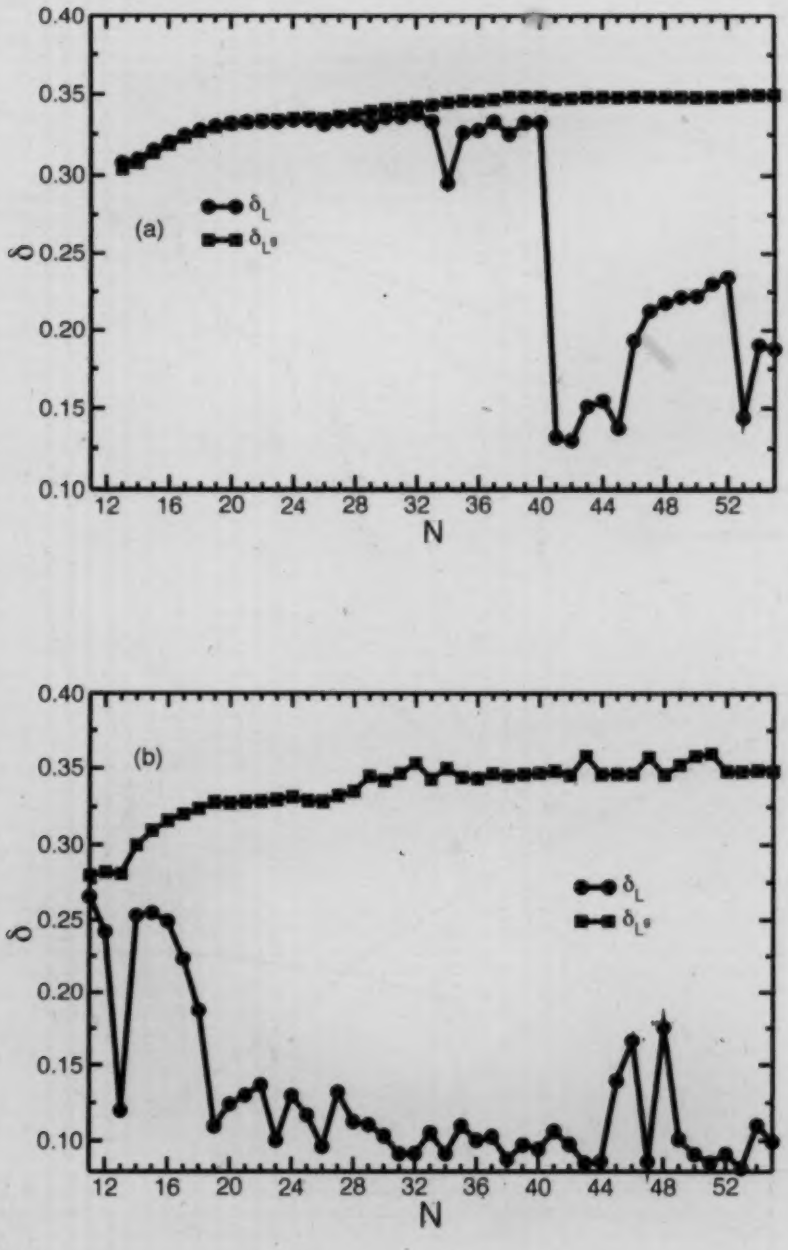

Figure 3.5: Specific (δ_L) (filled circles) and generic (δ_{L^g}) (squares) relative root mean square bond-length fluctuations as a function of N for $(para\mathrm{H}_2)_N$ (a) and $(ortho\mathrm{D}_2)_N$. (b).

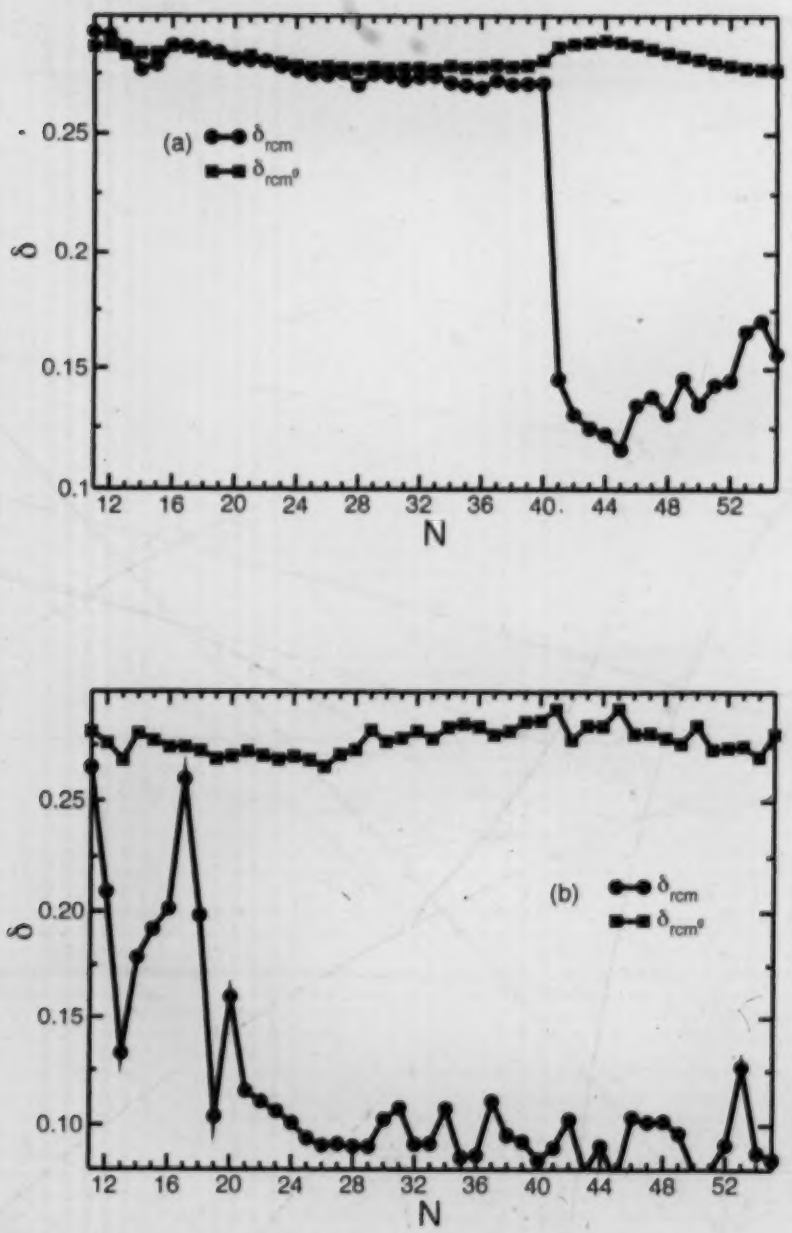

Figure 3.6: Specific (δ_{rcm}) (filled circles) and generic (δ_{rcm^g}) (squares) relative root mean square distance to the centre-of-mass fluctuations as a function of N for $(para\mathrm{H}_2)_N$ (a) and $(ortho\mathrm{D}_2)_N$ (b).

Fig. 3.6. This quantity is defined as:

$$\delta_{rcm} = \frac{1}{N}\sum_{i}\frac{(\langle R_{CM_i}^2\rangle - \langle R_{CM_i}\rangle^2)^{1/2}}{\langle R_{CM_i}\rangle}. \tag{3.3}$$

where R_{CM_i} is the distance of particle i from the centre-of-mass.

The "generic" counterpart to the above fluctuation is given by,

$$\delta_{rcm^g} = \frac{(\langle R_{CM}^2\rangle - \langle R_{CM}\rangle^2)^{1/2}}{\langle R_{CM}\rangle}, \tag{3.4}$$

where the $\langle\cdots\rangle$ represents average over all particles and an ensemble average. We observe a behaviour similar to that of δ_L. Large values of δ_{rcm} can be interpreted as particles moving between the shells. These results support the observations made above regarding the nature of these clusters.

We note that at N=34, δ_L exhibit a dip that is not present in the δ_{rcm} curve. This implies that at this size there is a quenching of the fluctuations of the pair distances, but this feature is not reflected in the fluctuations of the distance with respect to the centre-of-mass. This can be interpreted as particles being free to move between the shells to sites that are relatively fixed in space. On the other hand, at N=41 there is a loss of connectivity between the shells that coincides with the proposed structural transition. Similarly, it can be observed that at this same size (N=41) a rise appears in the generic centre-of-mass fluctuation (δ_{rcm^g}) curve.

Thus far, our discussion has focussed on the mobility of the particles within the cluster. Nothing has been said about the "order" of these systems when they display rigid behaviour. Translational symmetry is broken in finite size systems and we can therefore only refer to rotational symmetry. To assess this property, we calculate the ground state expectation value of the orientational BOP[91, 92] Q_4 and Q_6 defined as:

$$Q_l = \left(\frac{4\pi}{2l+1}\sum_{m=-l}^{m=l}|\bar{Q}_{lm}|^2\right)^{1/2}, \tag{3.5}$$

with

$$\bar{Q}_{lm} = \frac{1}{N_b}\sum_{r_{ij}<r_b} Y_{lm}(\theta_{ij},\phi_{ij}), \tag{3.6}$$

where $Y_{lm}(\theta_{ij}, \phi_{ij})$ are the spherical harmonics and the sum runs over all the pairs that are within a distance r_b. The distance r_b corresponds to the first minimum of the pair distribution function ($g(r)$).

These quantities have been used in the past[17, 18, 19, 97] to study temperature and size driven structural transitions of Lennard-Jones (LJ) clusters. Recently, Chakravarty *et al.* ?? have correlated the RDIS with the BOP, and found that a significant negative correlation can be interpreted as a solid behaviour. In a similar context, Baroni and Moroni[38] have used the so-called rotating-axes multipoles, and their imaginary time correlation function, to study the solid-liquid behaviour of $(para\mathrm{H_2})_{13}$ and $\mathrm{CO}(para\mathrm{H_2})_{12}$. More recently Paolini *et al.* [98] have used the same criterion to study positive ions in ^{4}He clusters. The main difference between BOPs and multipoles is that the former are calculated along "bonds" (pairs of particles) whereas the latter are calculated with respect to the centre-of-mass of the cluster.

Figure 3.7 shows Q_4 and Q_6 as a function of cluster size for $(para\mathrm{H_2})_N$ and $(ortho\mathrm{D_2})_N$. A rather monotonic behaviour is observed in the graph of Q_4 for both cluster types. With the exception of the jumps at N= 23 and 34 in the case of hydrogen, and at N =13 and 23 for deuterium, Q_4 decreases with increasing cluster size. A very similar behaviour is observed for Q_6. The values at N=13 do not correspond to a perfect IC ($Q_4 = 0$ and $Q_6 = 0.66332$) [92]. Despite the fact that $N = 13$ corresponds to a magic number, and in the case of deuterium to a rigid cluster, the system does not possess perfect five fold rotational symmetry. Larger clusters behave similarly and particles do not occupy fixed positions of concentric ICs. They correspond to an anti-Mackay growth pattern, similar to the findings in References [18] and [19]. This pattern consists of interpenetrated IC (such as the DI expected for N=19).

The main difference between our results, and those obtained for LJ clusters is the absence of anti-Mackay to Mackay transition at N= 39 [18]. We suggested a similar transition located at N=41-42. However, these BOP cannot be used to identify this transition, neither can they be used to identify an octahedral structure at N=38 in the case of $ortho\mathrm{D_2}$. It is also difficult to assess whether these clusters can lead to hcp-like structures as mentioned above. Recently[97], a method that utilizes simultaneously

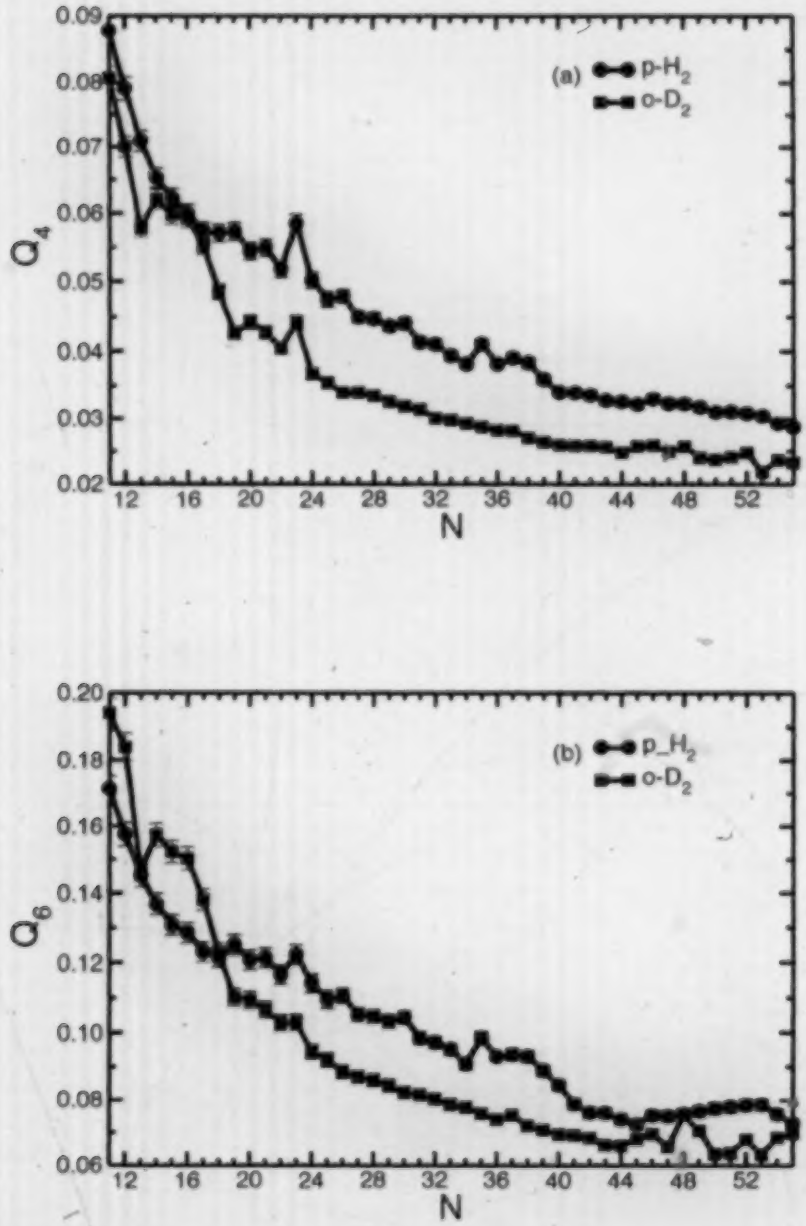

Figure 3.7: Bond order parameters Q_4 (a) and Q_6 (b) as a function of the number of particles N for *para*H_2 (filled circles) and *ortho*D_2 (squares).

local and global BOP has been used to determine structural transitions in Lennard-Jones clusters. This method may allow us to determine if the structural transitions we have proposed indeed occur in these quantum clusters.

3.4 Conclusions

In this Chapter, we have shown that the fine features of the energetics of $(para\mathrm{H}_2)_N$ are sensitive to the interaction potential used. In particular, different "magic numbers" are observed using different interaction models. We found that in the ground state, $(para\mathrm{H}_2)_N$ ($11 \leq N \leq 40$) are liquid with some degree of rigidity appearing at $N \geq 26$. It is possible that a liquid and a more rigid phase coexist beyond $N = 26$. In the N=41-45 range, $(para\mathrm{H}_2)_N$ clusters are rather rigid, while larger ones appear to be more liquid-like. The $(ortho\mathrm{D}_2)_N$ clusters with N=13 and $N \geq 19$ are on the other hand rigid. For the small clusters, an anti-Mackay layering is inferred from the results obtained in this work. At N= 41,42 an anti-Mackay to Mackay transition is proposed. Similarly, an octahedral structure is inferred for $(ortho\mathrm{D}_2)_{38}$. We do not find an important correlation between δ_L and the BOP (results not shown). In a finite size system, a small value of Q_6 does not necessarily mean a less ordered structure. Therefore, the monotonic behaviour of Q_4 and Q_6 cannot be associated to the lack of order in more rigid systems, as the results for $(ortho\mathrm{D}_2)_N$ clusters would suggest. We finally propose that the departure between the generic and specific behaviour of the distance and position fluctuations can be used as an indicator of the onset of rigidity in quantum clusters.

Chapter 4

Structure, energetics, and isomer coexistence in mixed quantum clusters

In this Chapter, we perform ground state simulations of mixed $(para\mathrm{H}_2)_N(ortho\mathrm{D}_2)_3$ clusters of size ranging from $N = 8$ to 37. The chemical potential is calculated and it is observed that magic numbers are consistent with those found in pure $para\mathrm{H}_2$ and $ortho\mathrm{D}_2$ clusters. The structural features of the mixed clusters are examined by analysing density profiles, one-dimensional Pekeris distribution functions of the $(ortho\mathrm{D}_2)_3$ sub-system and by direct visualization of density isosurfaces of the systems. The heavier $(ortho\mathrm{D}_2)_3$ complex resides in the centre-of-mass of the cluster for the various sizes under consideration. It is found that certain cluster sizes favour either equilateral, or near-linear isosceles $(ortho\mathrm{D}_2)_3$ configurations, while others show a coexistence between those two triangular shapes.[1]

4.1 Introduction

Scoles and coworkers [99] discovered a method to combine helium with other substances in the gas phase. These mixtures can be achieved if helium is prepared as

[1]The results presented in this chapter have appeared in a submitted article entitled: *Weakly bound complexes trapped in quantum matrices: Structure, energetics, and isomer coexistence in (paraH_2)$_N$ (orthoD_2)$_3$ clusters* Reused with permission from Javier Eduardo Cuervo and Pierre-Nicholas Roy, The Journal of Chemical Physics **submitted**, (2008). Copyright 2008 American Institute of Physics.

a small droplet containing up to a few thousands atoms. This discovery lead to the development of a new type of spectroscopy: Helium nanodroplet isolation (HENDI) spectroscopy [100, 101, 102, 103]. In this technique, Helium is used to provide a unique quantum environment to spectroscopic probes. Helium droplets are used to effectively isolate chromophores that, in turn, allow for the measurement of a spectrum similar to that of a free molecule in vacuum. Several studies have reported infrared and microwave spectra of a large number of chromophores using this technique [100].

Another interesting use of helium matrices that has been experimentally exploited is the isolation of complexes in metastable structures. Given certain experimental conditions, molecules can be captured by Helium droplets with an average time between each capture on the order of tens of microseconds. This time scale is very long with respect to the relaxation of intramolecular vibrations in gas-phase complexes [104]. Therefore, trapped molecules are completely cooled between capture events. In this way, complexes can be formed when a cold monomer combines with a similarly cold dimer, and so forth to produce larger complexes. The fast energy dissipation (quenching) provided by the Helium removes the energy that is released upon cluster formation, allowing the possibility to trap the system in a local minimum. Once a certain structure is established, the system is kinetically trapped, again because thermal energy is very limited in the cold quantum matrix environment. The most striking evidence of this process is the observation of the water cyclic hexamer and linear chain of HCN molecules by Nauta and Miller [105, 104] inside a Helium nanodroplet.

Besides the isolation of exotic structures of multiple dopants, the spectroscopic features and structural changes of weakly bound systems formed in the quantum matrix have also been studied experimentally [100]. The number of theoretical works is however more scarce and studies are limited to a maximum of two impurities [106]. An example can by found in the theoretical study by Jiang *et al.* [107].

Hydrogen clusters are also highly quantum systems and have been predicted to be superfluid [25, 51]. Therefore, hydrogen clusters offer an alternative to Helium for matrix isolation of molecules. Recent work [49] has shown that *para*H_2 clusters with $N = 11 - 25$ have shell structures that are liquid-like in their ground state. Larger

clusters ($N = 26 - 40$) display an increased rigidity that is believed to be caused by two phases coexisting in the same system. Theoretical finite temperature studies have shown that under certain conditions even a single isotopic substitution is enough to considerably "freeze" the clusters and hinder their superfluid properties [53].

The inclusion of a single molecular impurity inside small *para*H_2 clusters or in *para*H_2 clusters embedded in Helium nanodroplets, has been explored both experimentally [34, 108, 109] and theoretically [37, 110, 111]. In particular, $(para\text{H}_2)_N$CO and $(para\text{H}_2)_N$HF have been the subject of most of the theoretical works. Clusters composed of Hydrogen isotopic mixtures have also been studied in the past [112, 29, 53]. However, little attention have been given to the structure of the inherent weakly bound complex formed by the dopants. Due to isotopic segregation [112], it can be anticipated that the heavy isotope will migrate to the interior of the clusters. This creates the scenario of a complex embedded in a larger *para*H_2 cluster. In particular, it is interesting to study structural changes of the *ortho*D_2 trimer that may occur as the number of *para*H_2 molecules surrounding the complex is systematically augmented. In this way, the effect of different quantum environments on the properties of the complex can be investigated. Here, we seek to characterize the ground state properties of mixed quantum clusters and elucidate the effect of different quantum environments on the structure of the weakly-bound *ortho*D_2 trimer. The rest of this Chapter is organized as follows: in the following section, our methodology is briefly described. We show and discuss in Section 4.3 the results of ground state path integral Monte Carlo simulations. We finally provide conclusions in Section 4.4.

4.2 Methodology

In this work we use the path integral ground state method (PIGS) [56] as described in our previous work [57, 44]. Both isotopes are considered as point particles that differ only in their masses. Particles interact through a pair-wise additive potential that depends only on the interparticle distance, r_{ij}, for two particles i and j. The masses of *para*H_2 and *ortho*D_2 molecules we use are 2.0156500642 and 4.028203556

amu respectively. Two models are considered: the condensed phase Silvera-Goldman [75] (SG) and the gas phase Buck [76] potentials. The trial wave function we use is

$$\Psi_T(\mathbf{R}) = \exp\left[-\frac{1}{2}\sum_{i<j} u(\mid \mathbf{r}_i - \mathbf{r}_j \mid)\right], \tag{4.1}$$

where $\mathbf{R} = \{\mathbf{r}_1, \mathbf{r}_2, \ldots, \mathbf{r}_N\}$ denotes the vector that contains the cartesian coordinates ($\mathbf{r}_i$) of the N particles of the cluster. The pseudopotential u is given by

$$u(r_{ij}) = \left(\frac{b}{r_{ij}}\right)^5, \tag{4.2}$$

with b= 3.65 Å. We have shown that this trial wave function yields converged results using our methodology [44]. The computational approach is identical to that of Ref. [44]; note that all the calculations presented below use an imaginary time step of $\tau = 0.00125$ K^{-1} and a projection time of $\beta = 0.8$ K^{-1}.

4.3 Results and Discussion

We have calculated the ground state energy of $(para\mathrm{H}_2)_N(ortho\mathrm{D}_2)_3$ clusters. Table 4.1 contains the energy per particle ($e(N+3)$) of the mixed clusters for both potentials. Additionally, Fig. 4.1 shows the chemical potential, defined as $\mu(N+3) = E(N+3) - E((N-1)+3)$, where $E(N+3)$ is the energy of a cluster with N $para\mathrm{H}_2$ molecules. Both potentials show a rich chemical potential curve in terms of magic numbers. For the Buck potential, magic numbers are observed at a total number of particles of $N+3$ = 13, 19, 23, 26, 29, 36. The SG potential results display the same magic numbers except for their absence at $N+3$ =19, 36 and the presence of an additional magic number at $N+3 = 37$. These magic numbers have been observed previously in pristine clusters of either $para\mathrm{H}_2$ or $ortho\mathrm{D}_2$ [45, 44, 50, 52, 49]. For the small clusters of $N+3 = 13$ and $N+3 = 19$, magic numbers can be correlated to the completion of the first solvation shell and a very symmetric double icosahedral (DI) structure respectively. Magic numbers for a larger number of particles can be related to very symmetric and/or rigid structures, although only a detailed structural analysis can provide better insight into the nature of these clusters.

Table 4.1: Ground state energies per molecule ($e(N)$) (in K) of $(para\mathrm{H}_2)_N(ortho\mathrm{D}_2)_3$ clusters obtained for the Silvera-Goldman potential (Ref. [75]) and Buck potential (Ref. [76]) using PIGS. Uncertainties appear in parentheses.

N+3	Silvera-Goldman	Buck
11	-23.02(3)	-25.02(3)
12	-24.25(3)	-26.31(3)
13	-25.55(3)	-27.82(4)
14	-26.15(3)	-28.33(4)
15	-26.72(3)	-28.94(4)
16	-27.36(3)	-29.66(5)
17	-28.16(3)	-30.50(5)
18	-28.90(3)	-31.30(4)
19	-29.63(3)	-32.31(4)
20	-30.21(3)	-32.77(3)
21	-30.82(3)	-33.40(3)
22	-31.50(3)	-34.16(3)
23	-32.29(3)	-35.10(3)
24	-32.61(3)	-35.41(6)
25	-33.08(3)	-35.90(4)
26	-33.89(3)	-36.81(3)
27	-34.07(3)	-36.99(3)
28	-34.37(3)	-37.30(4)
29	-35.05(3)	-37.91(4)
30	-35.26(3)	-38.04(4)
31	-35.50(3)	-38.40(3)
32	-36.02(3)	-39.02(3)
33	-36.32(2)	-39.44(3)
34	-36.91(2)	-39.96(3)
35	-36.98(2)	-39.76(4)
36	-37.14(2)	-40.17(4)
37	-37.38(2)	-40.4(1)
38	-37.74(2)	-40.87(3)
39	-37.17(2)	-41.39(3)
40	-37.45(2)	-41.37(3)

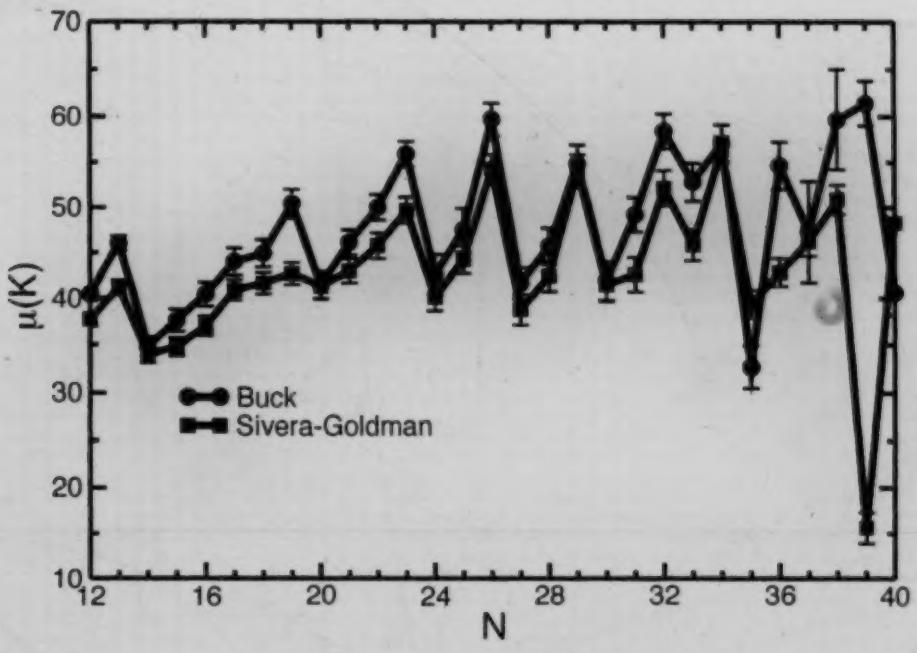

Figure 4.1: Chemical potential (μ) as a function of cluster size of $(para\mathrm{H}_2)_N(ortho\mathrm{D}_2)_3$ clusters using Buck potential (filled circles) (Ref. [76]) and Silvera-Goldman potential (squares) (Ref. [75]). When not shown, error bars are within the size of the symbols. Solid lines are only guides to the eye.

4.3.1 Structure

The radial density profile ($\rho(r)$) of $para\mathrm{H}_2$ and $ortho\mathrm{D}_2$ for some representative clusters are shown in Fig. 4.2. The $\rho(r)$ of $(para\mathrm{H}_2)_{10}(ortho\mathrm{D}_2)_3$, Fig. 4.2 (a), shows that a deuterium molecule occupies the centre-of-mass of the cluster and is never replaced by a hydrogen molecule. This is consistent with the isotopic segregation observed by Chakravarty [112]. The remaining particle density of both isotopes is located at a distance of ≈ 4 Å. No particle density is observed in between the centre-of-mass and the solvation shell. One can associate the above description with a structure

loosely based on an icosahedron. The completion of an icosahedral shell agrees with the magic number observed at $N = 13$. The doped system is more localized than its pure hydrogen counterpart [49]. Similar features are observed in clusters of up to 18 particles in total. At $N + 3 = 19$ a structural change is observed (Fig. 4.2 (b)). The density at the centre-of-mass gets completely depleted. A peak in the density of *ortho*D_2 appears at ≈ 1.8 Å. Continuous density develops between this peak and a peak at ≈ 5 Å in the hydrogen density. These features have been observed in clusters of both isotopes and are associated with a double icosahedral (DI) structure. This icosahedron consist of three parallel stacked rings of 5 particles, together with four particles placed along an axis perpendicular to the planes of the rings, and going through all three rings. This structure is also known as an anti-Mackay icosahedron [6]. Similar general features are observed in clusters of up to 28 particles. The main difference between these clusters is the extent of penetration of the hydrogen particles and the sharpness of the distribution of the deuterium particles. Examples are Fig. 4.2 (c) and 4.2 (d) that show the density profiles of clusters of 23 and 25 particles in total. New features are observed in the density profile of $(para\mathrm{H}_2)_{26}(ortho\mathrm{D}_2)_3$ (Fig 4.2 (e)). The density of *para*H_2 overlaps with that of *ortho*D_2 at distances between 1 and ≈ 3 Å. At this distance the *para*H_2 density reaches a minimum before it rises again into a second broad peak at ≈ 5 Å. The *ortho*D_2 density shows a wider splitted peak that covers distances from 3 to 4 Å. The $\rho(r)$ of deuterium in the $N + 3 = 34$, Fig. 4.2 (f), shows one peak and one small shoulder at ≈ 2 and 3 Å respectively. Similarly, the corresponding hydrogen density displays two peaks and one shoulder at ≈ 3, 5 and 6.5 Å . Another structural change is observed in $N + 3 = 37$, Fig. 4.2 (g), where the maximum of the deuterium density is shifted to a larger distance at $\approx$ 3 Å. Conversely, the first maximum of the hydrogen density is located at ≈ 1.5 Å , followed by a wide peak centred at ≈ 5.5 Å. At a cluster size of $N + 3 = 39$, Fig. 4.2 (h), both density profiles change back to display features similar to those observed at $N + 3 = 34$. The above analysis of density profiles indicates important structural changes occurring as a function of cluster size.

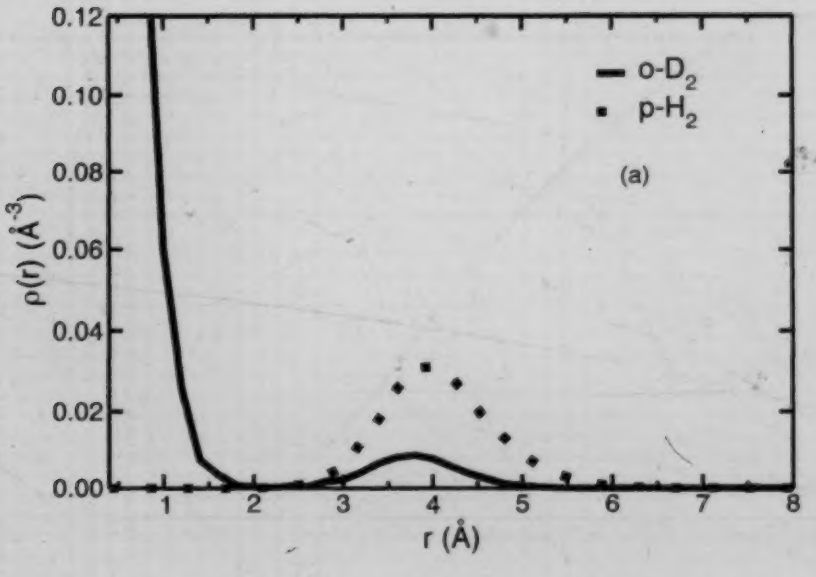
0.12
0.10
0.08
0.06
0.04
0.02
0.00
ρ(r) (Å^{-3})
1
2
3
4
5
6
7
8
r (Å)
o-D$_2$
p-H$_2$
(a)

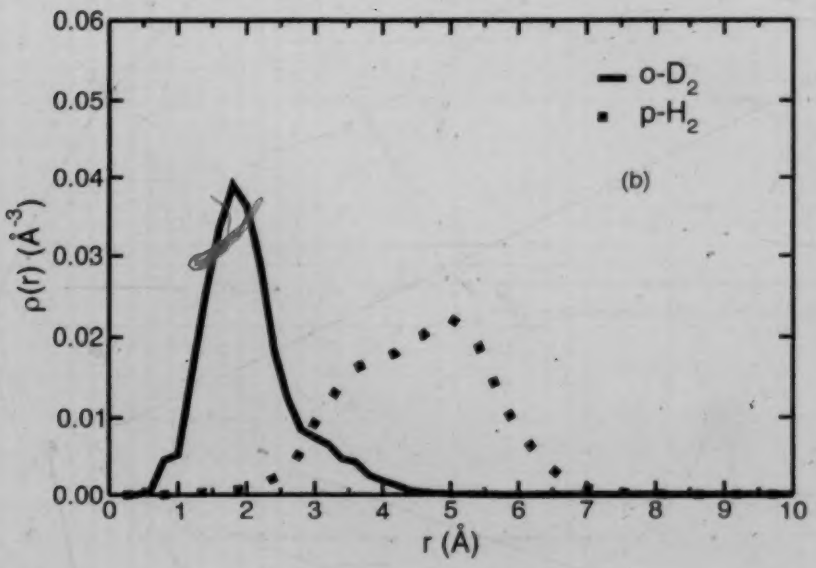
0.06
0.05
0.04
0.03
0.02
0.01
0.00
ρ(r) (Å^{-3})
0
1
2
3
4
5
6
7
8
9
10
r (Å)
o-D$_2$
p-H$_2$
(b)

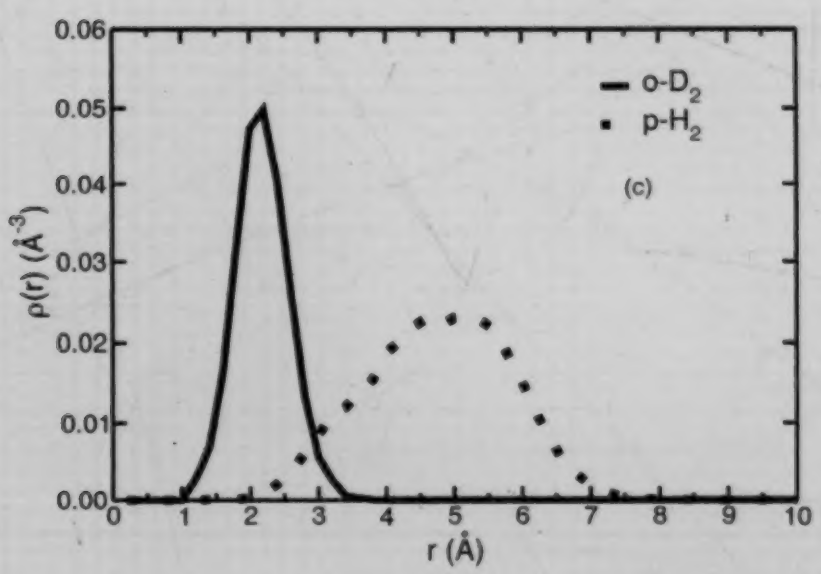
0.06
0.05
0.04
0.03
0.02
0.01
0.00
ρ(r) (Å^{-3})
0 1 2 3 4 5 6 7 8 9 10
r (Å)
o-D$_2$
p-H$_2$
(c)

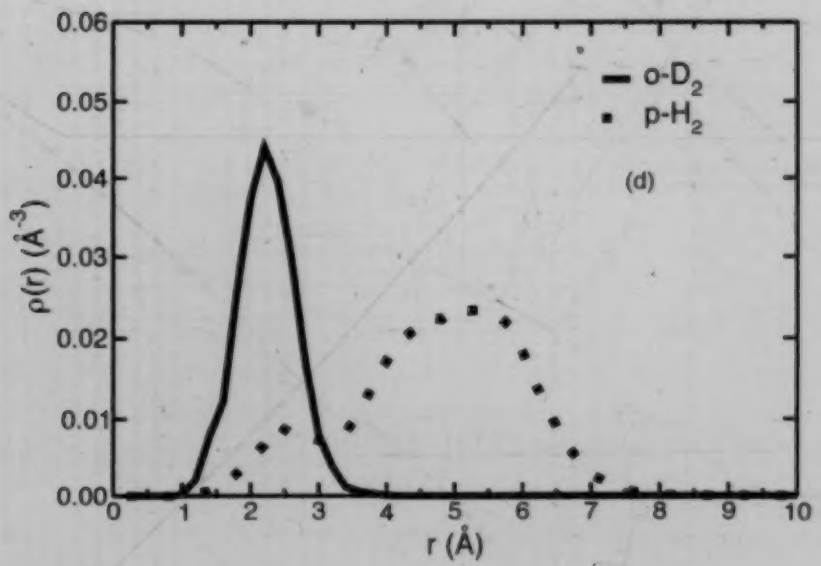
0.06
0.05
0.04
0.03
0.02
0.01
0.00
ρ(r) (Å^{-3})
0 1 2 3 4 5 6 7 8 9 10
r (Å)
o-D$_2$
p-H$_2$
(d)

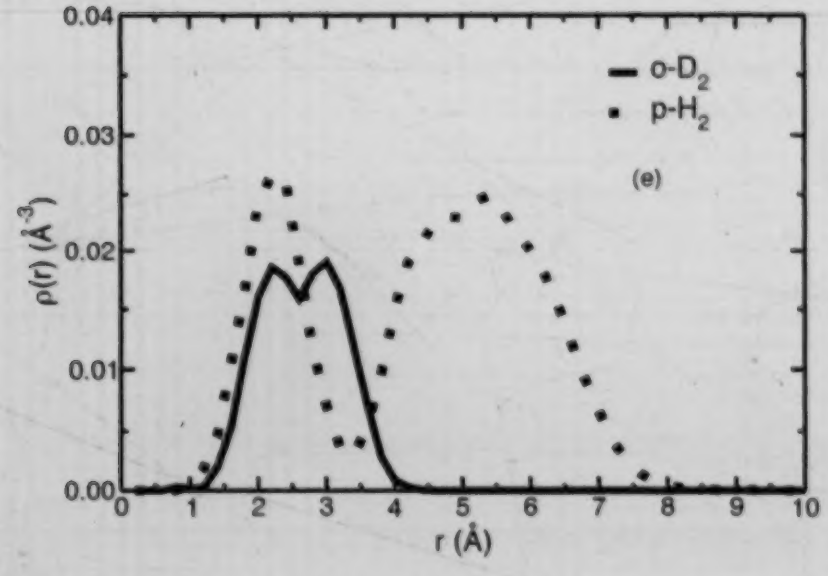
0.04
0.03
0.02
0.01
0.00
ρ(r) (Å^{-3})
o-D$_2$
p-H$_2$
(e)
0
1
2
3
4
5
6
7
8
9
10
r (Å)

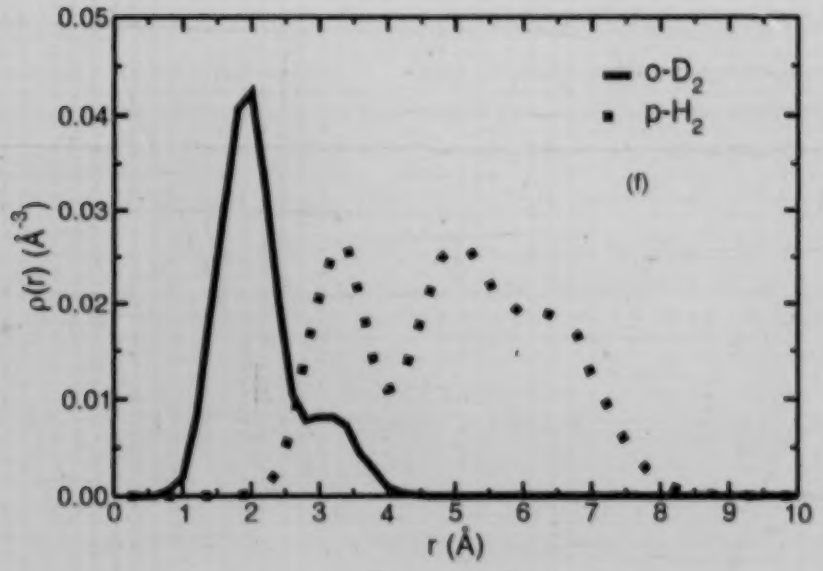
0.05
0.04
0.03
0.02
0.01
0.00
ρ(r) (Å^{-3})
o-D$_2$
p-H$_2$
(f)
0
1
2
3
4
5
6
7
8
9
10
r (Å)

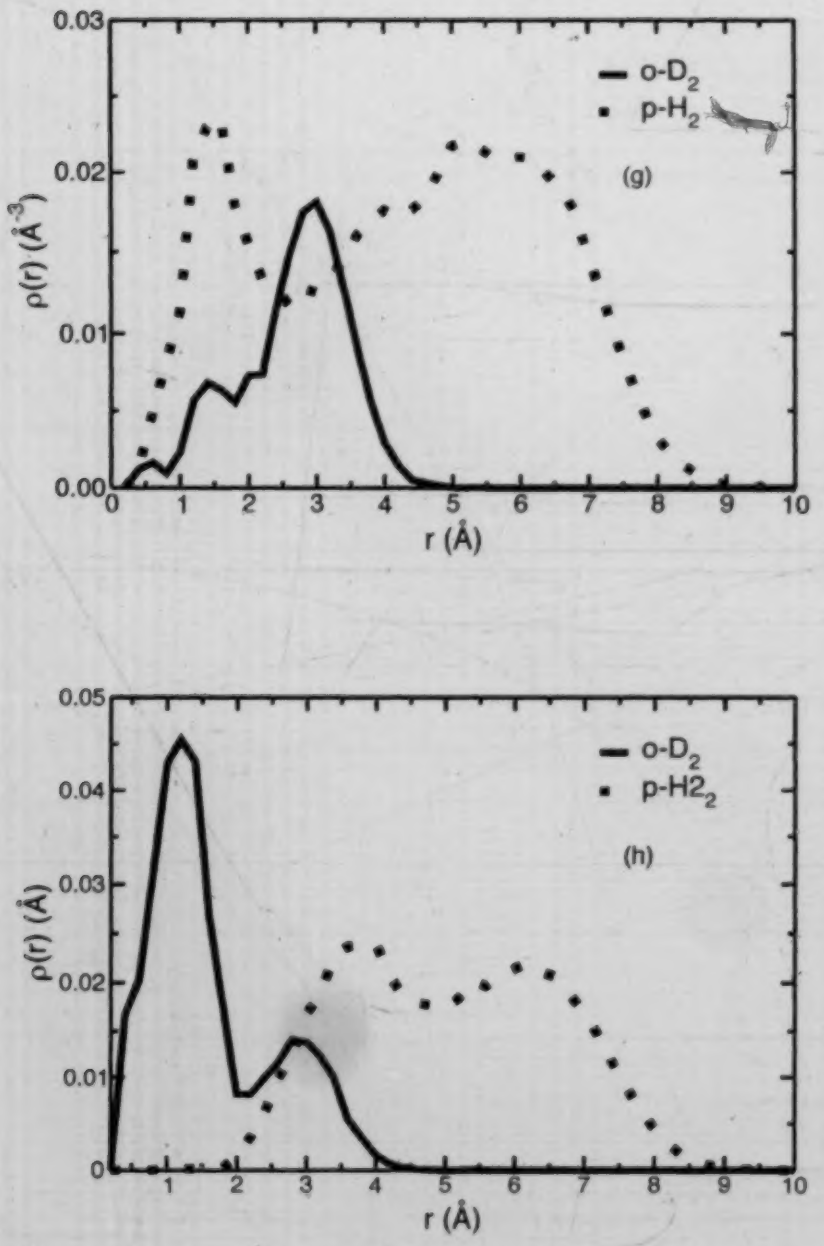

Figure 4.2: Density profile of ($ortho$D$_2$) (solid line) and ($para$H$_2$) (dotted line), in ($para$H$_2$)$_N$($ortho$D$_2$)$_3$ clusters N+3=13 (a), 19 (b), 23 (c), 25 (d), 29 (e), 34 (f), 37 (g), 39 (h).

To gain further insight in the behaviour of the deuterium dopant, we show in Fig. 4.4, the Pekeris one particle distribution function of the $(ortho\mathrm{D}_2)_3$ subsystem in different clusters. This type of distribution has been defined in Ref. [82] and used in previous work [83, 44]. The distribution, $d(r_\alpha)$ is obtained from the value of the Pekeris coordinates [113] of the dopant trimer along the simulation. The three coordinates, r_α (where α=1,2 or 3), correspond to the radii of the mutually tangent circles centred at the particle position and can be defined in terms of inter particle distance as,

$$\begin{aligned} r_1 &= \frac{1}{2}(r_{12} + r_{31} - r_{23}), \\ r_2 &= \frac{1}{2}(r_{12} + r_{23} - r_{13}), \\ r_3 &= \frac{1}{2}(r_{23} + r_{31} - r_{12}) \,. \end{aligned} \tag{4.3}$$

For the $N+3 = 11-18$ clusters, similar Pekeris distributions are observed. We show specifically in Fig. 4.4 (a) the distributions for $N+3 = 11,15$. For all clusters in this size range, $d(r_\alpha)$ shows a non-zero value at $r_\alpha = 0$. This corresponds to linear configurations of the subsystem. The value of the distribution function at $r_\alpha = 0$ is reduced as the clusters grow in size. At larger cluster sizes, the distribution gets sharper peaking at ≈ 2 Å. The amplitude of the distribution at zero gets depleted and ultimately reaches a value of zero as shown in Fig. 4.4 (b) for $(para\mathrm{H}_2)_{16}(ortho\mathrm{D}_2)_3$ and $(para\mathrm{H}_2)_{23}(ortho\mathrm{D}_2)_3$. These can be interpreted as the trimer having mostly an equilateral conformation. The only two exceptions to this behaviour are found at $N+3 = 29, 37$, Fig. 4.4 (c), where multimodal distributions are observed. The first peak of these distributions is at ≈ 0.8 Å, the second at ≈ 2 Å and the third and last peak at ≈ 3.2 Å. These features can be interpreted as important contributions from equilateral (middle peak) and obtuse (isosceles) triangular configurations.

To directly inspect the structure of these clusters, we have computed the volumetric density of the systems. We have taken advantage of the internal frame of reference that the $(ortho\text{-}\mathrm{D}_2)_3$ trimer provides. The body-fixed frame or embedding is defined as follows: the Z axis is defined as the relative distance vector between the two $ortho\text{-}\mathrm{D}_2$ molecules that are the furthest apart; the distance vector between the

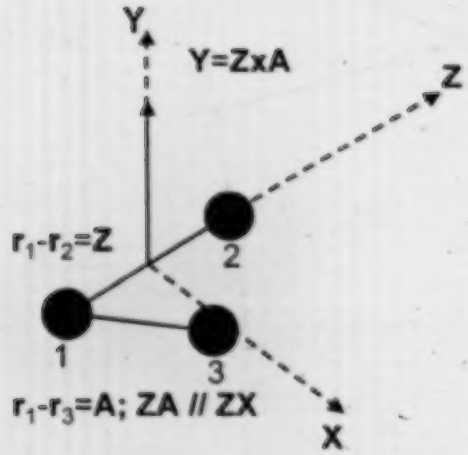

Figure 4.3: Deuterium-fixed frame.

third *ortho*-D_2 and its closest neighbour is used to define the XZ plane; the Y axis is finally obtained as a vector orthogonal to the XZ plane via a cross product. This choice of embedding (depicted in Fig. 4.3.1) allows the construction of the density isosurfaces shown in Fig. 4.5. As expected, the general feature of all clusters is a much more localized deuterium trimer sub-system compared to the hydrogen solvent. Small clusters ($N+3 \leq 22$) show a very delocalized *para*H_2 density (Figs. 4.5 (a) and (b)). Well defined structural features can however be observed. In particular, clusters with $N+3 = 13$ and $N+3 = 19$ respectively have icosahedral and DI structures as observed in pure classical Lennard-Jones clusters [11, 12]. At a cluster size of ($N + 3 = 23$), as shown in Fig. 4.5 (c), a much more localized structure is observed. The structure corresponds to a very symmetric DI, supporting our earlier inference regarding an anti-Mackay layering. The addition of two *para*H_2 ($N + 3 = 25$) particles, as shown in Fig. 4.5 (d), results in further delocalization. The two additional molecules do not occupy specific sites in a DI motif, they are rather delocalized on the surface of the cluster. To illustrate this point, we show in Fig. 4.5 (d) the delocalized isosurfaces (in grey) that correspond to a value of density that approximately represents the extra particles. This behaviour is observed through all the clusters up to $N + 3 = 29$.

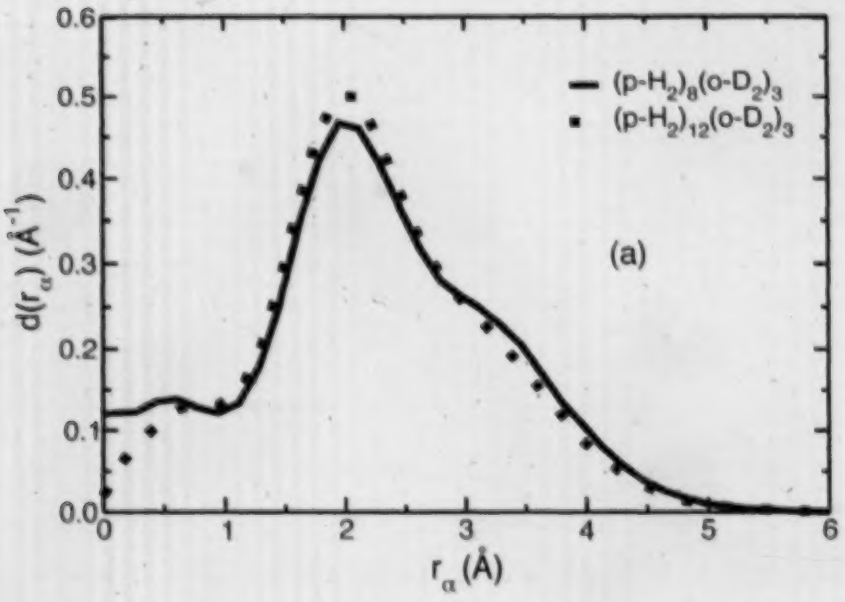
0.6
0.5
0.4
0.3
0.2
0.1
0.0
0
1
2
3
4
5
6
$d(r_\alpha)$ (Å^{-1})
r_α (Å)
$(p\text{-}H_2)_8(o\text{-}D_2)_3$
$(p\text{-}H_2)_{12}(o\text{-}D_2)_3$
(a)

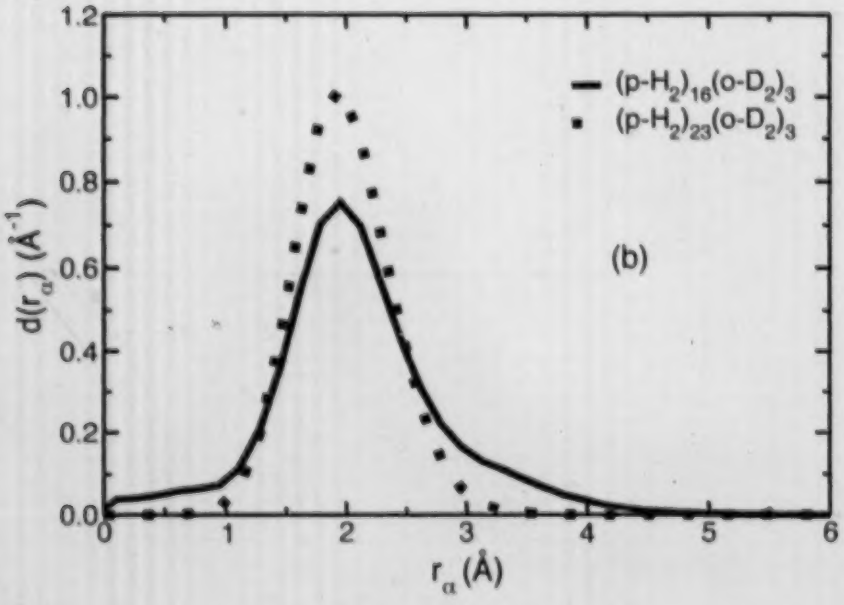
1.2
1.0
0.8
0.6
0.4
0.2
0.0
0
1
2
3
4
5
6
$d(r_\alpha)$ (Å^{-1})
r_α (Å)
$(p\text{-}H_2)_{16}(o\text{-}D_2)_3$
$(p\text{-}H_2)_{23}(o\text{-}D_2)_3$
(b)

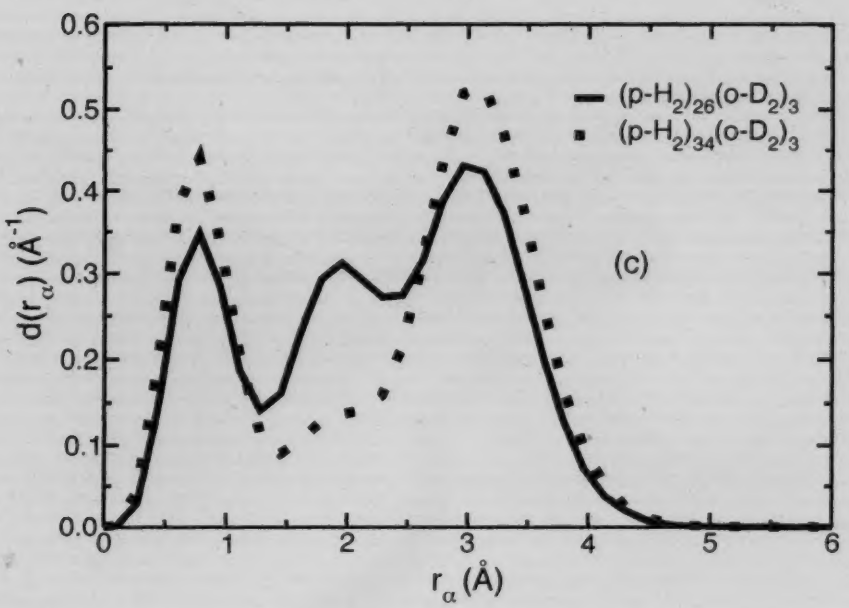

Figure 4.4: Pekeris distribution function of $(orthoD_2)_3$ in some $(paraH_2)_N(orthoD_2)_3$ clusters.

(a)

(b)

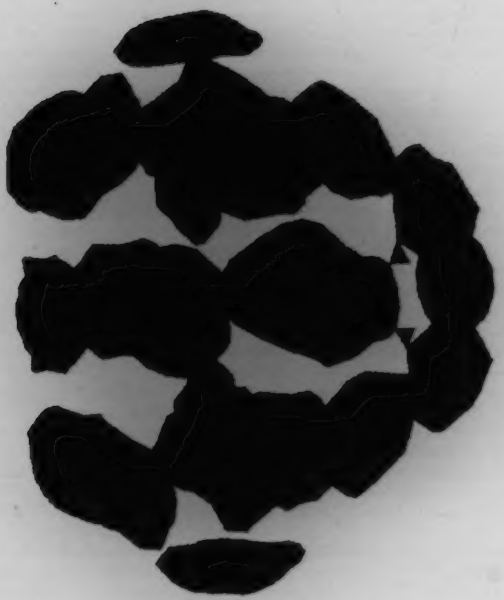

(c)

(d)

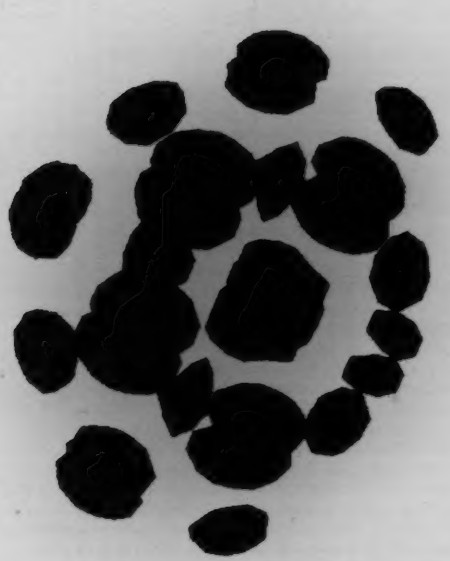

(e)

(f)

Figure 4.5: Density isosurfaces of $(para\mathrm{H}_2)_N(ortho\mathrm{D}_2)_3$ clusters of $N+3=13$ (a), 19 (b), 23 (c), 25 (d), 29 (e) and 37 (f). Pictures generated with VMD.[114]

At $N+3=29$, Fig. 4.5 (e), the whole cluster becomes localized again and displays a symmetric DI structure. Larger clusters, such as $N+3=37$, show a localized core based on a $N+3=29$ DI inside a delocalized surface as shown in Fig. 4.5 (f). Additionally, clusters made of $N+3$ =29,37 particles display an obtuse triangle structure for the deuterium subsystem, rather than the equilateral triangle observed in the rest of the clusters, which confirms our above interpretation based on Pekeris distribution functions.

4.3.2 Stabilization of isomers

Based on the results described in Section 4.3.1, we can explore the possibility that hydrogen clusters can provide an environment for structural transformations (isomerization) of the deuterium subsystem. To further explore this scenario, we define the following reaction coordinate for the isomerization from equilateral to obtuse isosceles triangular configurations,

$$q=\sqrt{(r_{12}-r_{13})^2+(r_{12}-r_{23})^2+(r_{23}-r_{13})^2}, \tag{4.4}$$

where r_{ij} corresponds to the distance between deuterium particles i and j at a given configuration of the system. This quantity measures the deviation of the trimer from the equilateral conformation. We show in Fig. 4.6 the negative of the natural logarithm of the asymmetric factor distribution function, calculated for some representative systems from the PIGS simulation as

$$w(q)=-\ln\left[\int d\mathbf{R}|\Psi(\mathbf{R})|^2\delta(q-q(\mathbf{R}))\right], \tag{4.5}$$

where $\Psi(\mathbf{R})$ is the ground state wavefunction. The inspection of $w(q)$ reveals, for some clusters, an interesting behaviour. The smallest clusters ($N+3\leq 15$), shown in Fig. 4.6 (a), display two minima separated by an small rather wide "barrier". The deeper minimum at ≈ 0.8 Å corresponds to structures close to equilateral. As the clusters get larger, the "barrier" increases and the shallower minimum disappears, until the point that only one deep minimum can be observed, as shown in Fig. 4.6 (b). The latter feature is observed for all clusters of $N+3\geq 23$ particles, with the

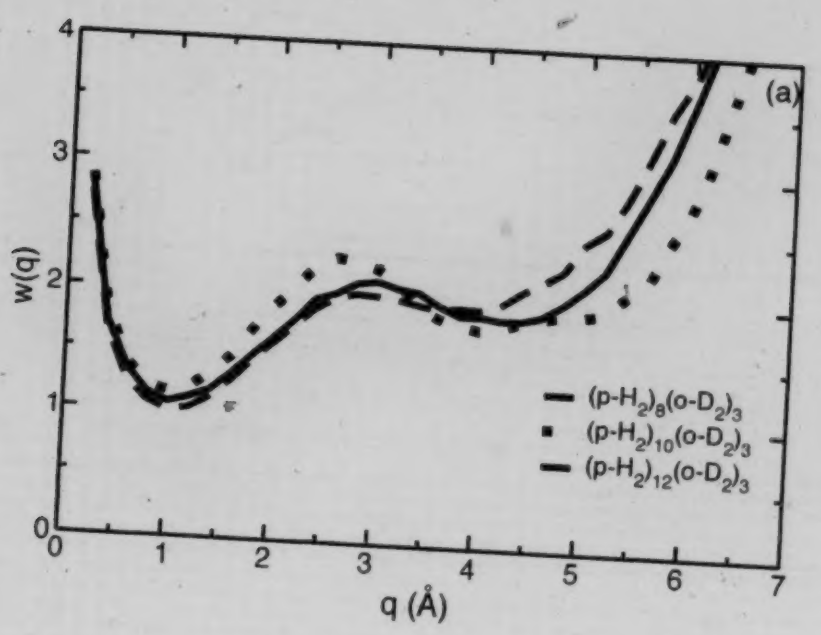
(a)
w(q)
q (Å)
$(p\text{-}H_2)_8(o\text{-}D_2)_3$
$(p\text{-}H_2)_{10}(o\text{-}D_2)_3$
$(p\text{-}H_2)_{12}(o\text{-}D_2)_3$

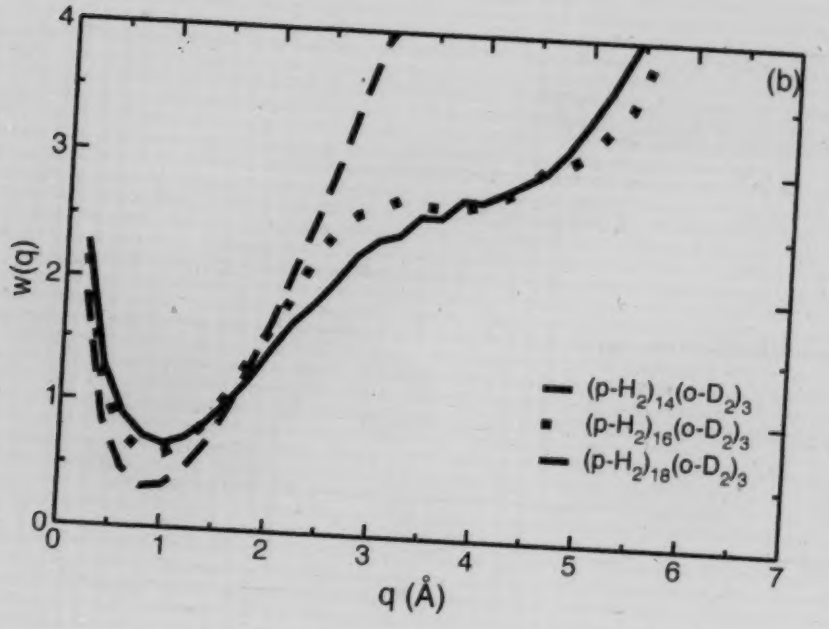
(b)
w(q)
q (Å)
$(p\text{-}H_2)_{14}(o\text{-}D_2)_3$
$(p\text{-}H_2)_{16}(o\text{-}D_2)_3$
$(p\text{-}H_2)_{18}(o\text{-}D_2)_3$

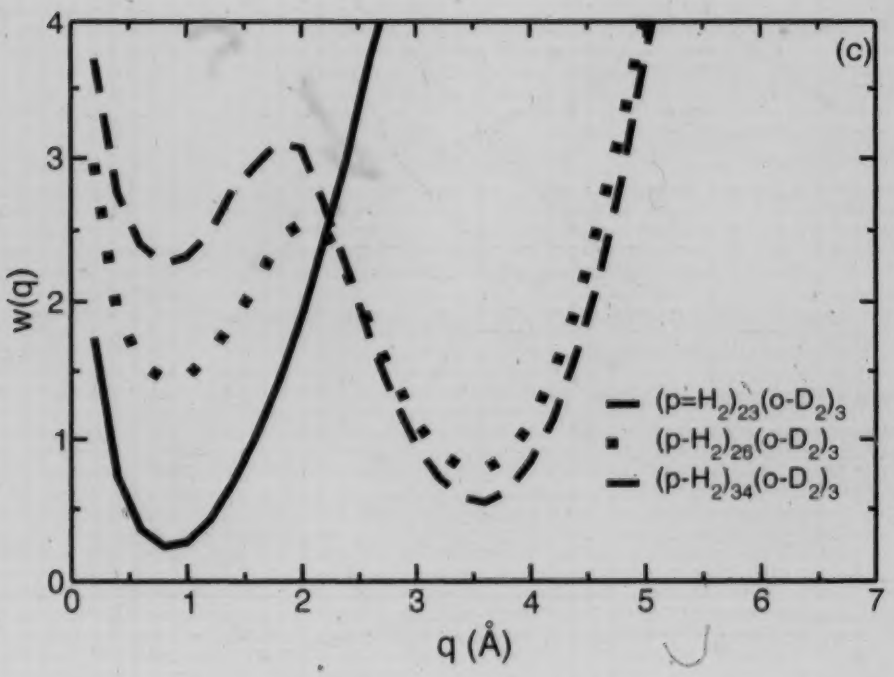

Figure 4.6: Negative of the natural logarithm of the reaction coordinate distribution function for some $(para\mathrm{H_2})_N(ortho\mathrm{D_2})_3$ clusters.

exceptions of $N+3 = 29, 37$ (Fig. 4.6 (c)). These two clusters display a population inversion in the asymmetric factor distribution function. In these particular cases, the deeper minimum is located at ≈ 3.5 Å and a sharper "barrier" is also observed. These features are in agreement with the previous observation that these two clusters display an obtuse deuterium trimer, instead of the more generally observed equilateral structure. These observations are evidence of the stabilization of less favoured structures of the trimer by the hydrogen environment. On the other hand, they are also evidence of an environment-enhanced tunnelling-driven isomerization process. These phenomena can be seen as the hydrogen counterpart of the observations made by Nauta and Miller [105, 104] in their Helium droplet experiments. The time-scale of these processes is of great importance, since it determines the possibility of realizing an experimental setup to isolate and observe these two distinct configurations. However, the determination of this rate falls in the realm of quantum dynamics and will be the subject of future work.

4.4 Conclusions

We have calculated the ground state energy of $(para\mathrm{H}_2)_N(ortho\mathrm{D}_2)_3$ clusters with ($N = 8$–37) using the PIGS method. The chemical potential as a function of cluster size displays magic numbers consistent with those observed in pure clusters of both isotopic species. In the size range studied, the interaction potential does not have a strong effect on the position of the magic numbers as it does in the case of pristine clusters.

The $(ortho\mathrm{D}_2)_3$ sub-system remains at the interior of the cluster. At small cluster sizes ($N \leq 22$), the $para\mathrm{H}_2$ environment is delocalized. Larger clusters display a localized anti-Mackay icosahedral core and a delocalized surface.

We found that different environments have different effects on the structure of the $(ortho\mathrm{D}_2)_3$. From $N = 8 - 14$, the deuterium trimer is a floppy system, able to explore different structures including linear configurations. On the other hand, from $N = 19 - 40$, the environment "locks" the trimer in a triangular configuration,

mostly equilateral. The exception of this behaviour was found at $N = 23, 34$. These clusters display a deuterium trimer that prefers an isosceles configuration, although the system is able to explore equilateral configurations. To summarize, small *para*H_2 clusters provide a unique quantum environment to the deuterium trimer that allows the subsystem to undergo structural transformations. On the other hand, we found that the dopand can favour the localization of larger clusters that, in turn, restricts the movement of the deuterium particles. Equilateral structures are generally favoured except in the cases of $N + 3 = 29$,37 where the quantum environment induces an isosceles structure of the deuterium trimer. Additionally, these structural changes are correlated with the appearance of magic numbers in the chemical potential. The asymmetric factor proved to be a suitable reaction coordinate and will be used in future quantum dynamical studies of the rate of isomerization.

Chapter 5

Imaginary-time dynamics of quantum clusters

In this Chapter we explore the imaginary-time dynamics of quantum clusters. We calculated imaginary time correlation functions by means of the PIGS method. To test our methodology we attempt to extract the excited states of the hydrogen trimer. Armed with imaginary-time correlation functions, we further study the structural transformations of the weakly bound deuterium trimer inside a small hydrogen cluster. We calculate the imaginary-time side-side correlation function along a suitable reaction coordinate. From this data we estimate the imaginary time rate constant of the process. Our preliminary results are encouraging, however they reveal the formidable challenge of real-time quantum dynamics.

5.1 Introduction

The calculation of dynamical properties of complex quantum mechanical systems is one of the biggest challenges of theoretical chemistry. It is of great importance to tackle this challenge since many properties that are accessible experimentally, such as transport coefficients and reaction rates, are time-dependent in nature. Notwithstanding all the theoretical effort thus far, there still exists important limitations to the numerically exact solutions of the Schrödinger equation for complex molecular systems. For example, exact basis-set methods are limited by the size of the systems they can treat due to exponential scaling.

Many experimental methods used to probe the dynamics of a system share a common characteristic: they monitor the response of the system to a perturbation caused by an external field weakly coupled to it. In this regime, linear response theory is adequate to describe the dynamics of the system. This means that dynamical properties can be expressed in terms of time correlation functions (TCF) of the corresponding dynamical operators [115].

The calculation of time correlation functions for quantum dynamical systems is a formidable task. It is however relatively easy to perform such calculations for classical systems. For this reason, approximate methods that combine classical and quantum mechanics have recently been gaining popularity. Methods based on semiclassical theory use trajectories calculated from classical dynamics to obtain approximate quantum mechanical TCF. Semiclassical methods are able to capture (sometimes very accurately) quantum effects such as interference, zero point motion and tunnelling [116, 117, 118]. Nevertheless, extensive development of these methods is still in progress [119, 120, 121, 122]. Similarly, methods derived from path integral theory, such as centroid molecular dynamics (CMD) [123, 124, 125] and ring polymer molecular dynamics (RPMD) [126] have shown great promise for the study of complex systems. These methods are amenable to the study of large molecular systems due to their favourable scaling with the size of the system. The main impediment to the wider application of these methods is the insufficient understanding of their limitations [127]. Their applicability to systems of appreciable complexity remains therefore unexplored.

Stochastic path integral methods have proven to be very successful at calculating equilibrium properties of many-body quantum systems. They however suffer from the so called real-time "sign problem" when applied to the calculation of dynamical properties. The "sign problem" arises from the exponential growth of statistical errors at longer times. This exponential growth is due to the the rapidly oscillating kernel (real-time propagator) of the multidimensional integrals that need to be evaluated using Monte Carlo techniques. This hinders the direct application of path integral methodologies to calculate TCF.

A different avenue to quantum dynamics is the use of imaginary-time correlation functions (ITCF) [128, 129, 130]. The main advantage of this type of methods is that, contrary to real TCF, ITCF can be readily obtained by means of path integral Monte Carlo (PIMC) simulations, circumventing the "sign problem". Methods based on this scheme involve the analytic continuation of the imaginary time correlation function to real time. The continuation requires the numerical inversion of a Laplace transform that is known to be a highly unstable operation, thus requiring the use of sophisticated methods such as maximum entropy (ME) techniques. These methods have been used to calculate transport properties in quantum condensed phase systems [131, 132] and thermal rate constants [133, 134, 135]. Excited states can also be extracted through ITCF obtained from ground state simulations [136, 69, 137, 138]. In particular, the dipole-dipole ITCF calculated using the reptation quantum Monte Carlo (RQMC) [69, 139, 140] method have been very useful for the simulation of the rotational and vibrational spectra of linear rotors embedded in Helium clusters. Similarly, pure helium clusters and clusters doped with different spectroscopic probes have been studied using the projection operator imaginary time spectral evolution (POITSE) method [141, 142, 143]. Although promising, these methods still have limitations. To ensure the stability of the analytic continuation, the imaginary time data must be determined with high accuracy, which implies long and possibly expensive simulations. More importantly, many real time signals can be compatible with the imaginary time data due to the statistical uncertainty of the latter.

In this chapter we describe our initial efforts to the study of dynamics in quantum clusters. In particular, we explore the adequacy of the PIGS method for the calculation of excited states of weakly bound trimers and rate constants. In the case of rate constants, we avoid the analytic continuation and assess the quality of the physical insight that can be obtained from imaginary time data. To this end we use a methodology based on ground state ITCF. The remainder of this chapter is organized as follows: in the following section we describe the theory and methodology used in the calculations. In Section 5.3 we present and discuss our results. We finally present our conclusions in Section 5.4

5.2 Theory and methodology

A general quantum time correlation function is given by

$$C_{AB}(t) = \langle \hat{A}(0)\hat{B}(t)\rangle = \frac{1}{Z}\mathrm{Tr}\left(\exp[-\hat{H}/(k_B T)]\hat{A}\exp[i\hat{H}t/\hbar]\hat{B}\exp[-i\hat{H}t/\hbar]\right), \tag{5.1}$$

where $\exp[-\hat{H}/k_B T]$ is the thermal density operator, $Z = \mathrm{Tr}\left(\exp[-\hat{H}/k_B T]\right)$ is the partition function, $\hat{A}$ and $\hat{B}$ are quantum mechanical operators corresponding to measurable observables and $\exp[i\hat{H}t/\hbar]\hat{B}\exp[-i\hat{H}t/\hbar] = \hat{B}(t)$ is the Heisenberg representation of operator $\hat{B}$. In the ground state, Eq. 5.1 becomes,

$$C_{AB}(t) = \langle \hat{A}(0)\hat{B}(t)\rangle = \langle \Phi_0|\hat{A}\exp[i\hat{H}t/\hbar]\hat{B}\exp[-i\hat{H}t/\hbar]|\Phi_0\rangle. \tag{5.2}$$

One can also define a ground state imaginary-time autocorrelation function of $\hat{A}$ as

$$\hat{C}_A(\tau) = \langle \hat{A}(0)\hat{A}(\tau)\rangle = \sum_{n=0}^{\infty} |\langle \Phi_0|\hat{A}|\Phi_n\rangle|^2 \exp[-\tau(E_n - E_0)], \tag{5.3}$$

where a complete set of states was used and $-it/\hbar$ was replaced by τ. The above is a sum of decaying exponentials with decay constants $E_n - E_0$ (excitation energies), and with spectral weights given by the matrix element $|\langle \Phi_0|\hat{A}|\Phi_n\rangle|^2$. Note that at long imaginary-time, only the lowest lying excited states contribute to the sum. This allow us to approximate the ITCF as a finite sum amenable to multi-exponential fitting.

5.2.1 Reaction rates

Miller and co-workers [144, 145] have developed a quantum mechanical theory for thermal rate constants. The theory is based on the quantum mechanical reactive flux through a surface (s) that divides reactants from products. The exact expression for the thermal rate constant is given by

$$k(T) = Z_r(T)^{-1}\mathrm{Tr}\left(\exp[-\hat{H}/k_B T]\hat{F}P_r\right), \tag{5.4}$$

where Z_r is the partition function of the reactants, $\hat{F} \equiv i/\hbar[\hat{H}, \hat{h}]$ is the reactive flux operator and P_r is the long time limit of the heaviside function,

$$P_r = \lim_{t\to\infty} \exp[i\hat{H}t/\hbar]\hat{h}(s)\exp[-i\hat{H}t/\hbar]. \tag{5.5}$$

It can be shown that the projection operator P_r corresponds to the time integral of the time-evolved flux operator, which allows us to write the expression for $k(T)$ i terms of the flux-flux quantum autocorrelation function, $C_{ff}(t)$, as

$$k(T) = Z_r(T)^{-1} \int_0^\infty dt C_{ff}(t) \,. \tag{5.6}$$

Additionally, a different expression for the thermal rate constant can be written in terms of another TCF as

$$k(T) = \lim_{t\to\infty} \frac{dC_{ss}(t)}{dt}, \tag{5.7}$$

where $C_{ss}(t)$ is the side-side quantum autocorrelation function

$$C_{ss}(t) = \mathrm{Tr}\left(\exp\left[-\hat{H}/(k_B T)\right]\hat{h}(s)\exp\left[i\hat{H}t/\hbar\right]\hat{h}(s)\exp\left[-i\hat{H}t/\hbar\right]\right). \tag{5.8}$$

Although these formulations are formally exact, their practical use is hindered by the difficulty that poses the calculation of quantum TCF of complex molecular systems. On the other hand, as mentioned in Section 5.1, the calculation of ITCF is rather trivial via Monte Carlo simulations [146].

5.3 Results and discussion

As discussed above, the imaginary time correlation function can be decomposed in terms of eigenstates. Our initial attempt is to extract the first excited state of a hydrogen cluster. This is done for the *para*H_2 trimer for which the bound states can be obtained from exact diagonalization. We use the approach described in Ref. [82] and used in Chapter 2 for this exact diagonalization. The results are presented in Table 5.1 and will be used to assess the quality of our analysis of the ITCF. We also present in Table 5.1 the bound states of the *ortho*D_2 trimer for further comparison purposes. In order to extract some bound states from a PIGS imaginary time correlation function, we first need to chose the operator $\hat{A}$ for which we will calculate the auto-correlation function (see Eq. 5.8). Our initial choice is to use the magnitude of the average interparticle pair distance vector. For three particles,

Table 5.1: Exact ($J = 0$) bound states of the *para*H_2 and *ortho*D_2 trimers (using the potential of Ref. [75])

	(*para*H_2)		(*ortho*D_2)	
n	$E_n(K)$	$\lvert\langle 0\rvert r\rvert n\rangle\rvert^2$	$E_n(K)$	$\lvert\langle 0\rvert r\rvert n\rangle\rvert^2$
0	-13.2	24.3	-28.5	17.7
1	-4.5	0.38	-16.5	0.09
2			-8.7	0.0002

this quantity is $r = \frac{1}{3}(r_{12} + r_{13} + r_{23})$. This quantity is symmetric upon exchange of particles and only excited states of that symmetry will have a non-zero matrix element with the ground state (which is also totally symmetric). We also show in Table 5.1 those matrix elements obtained from exact diagonalization. The PIGS correlation function for this operator is shown in figure Fig. 5.1. The PIGS implementation of the procedure to extract excited states is very similar to that of the POITSE method [141, 142]. In general, we compute the PIGS imaginary-time autocorrelation function of the operator $\hat{A}$ as

$$\begin{aligned}
\langle \hat{A}(0)\hat{A} \quad (\tau) \quad \rangle \approx & \left[\int d\mathbf{R}_1 \cdots \int d\mathbf{R}_{M+l} \langle \Psi_T | \mathbf{R}_1 \rangle \prod_{i=1}^{M+l} G_0(\mathbf{R}_i, \mathbf{R}_{i+1}) \hat{A} \right] \\
\times & \left[\int d\mathbf{R}_{M+l+1} \cdots \int d\mathbf{R}_{M+l+k} \prod_{i=M+l+1}^{M+l+k} G_0(\mathbf{R}_i, \mathbf{R}_{i+1}) \hat{A} \right] \\
\times & \left[\int d\mathbf{R}_{M+l+k+1} \cdots \int d\mathbf{R}_{2(M+l)} \prod_{i=M+l+k+1}^{2(M+l)} G_0(\mathbf{R}_i, \mathbf{R}_{i+1}) | \langle \mathbf{R}_{2(M+l)} | \Psi_T \rangle \right] \\
\times & \left[\int \mathbf{R}_1 \cdots \int d\mathbf{R}_{2M} \langle \Psi_T | \mathbf{R}_1 \rangle \prod_{i=1}^{2M-1} G_0(\mathbf{R}_i, \mathbf{R}_{i+1}) \langle \mathbf{R}_{2M} | \Psi_T \rangle \right]^{-1}, \qquad (5.9)
\end{aligned}$$

where the total length of the path is $2(M+l)\tau = \beta/2 + \lambda = 2.7\ \mathrm{K}^{-1}$. In this definition $\beta/2 = 0.225\ \mathrm{K}^{-1}$ is the projection imaginary-time needed for the trial wavefunction to relax to the ground state and $\lambda = 0.9\ \mathrm{K}^{-1}$ is the imaginary-time interval at which the ITCS is calculated. Finally, $\tau = 0.0004\ \mathrm{K}^{-1}$ is the unit of imaginary time discretization. Note that k must be in the interval $[0, l]$. The main difference between our approach and the POITSE method is that we begin to calculate the ITCF on a

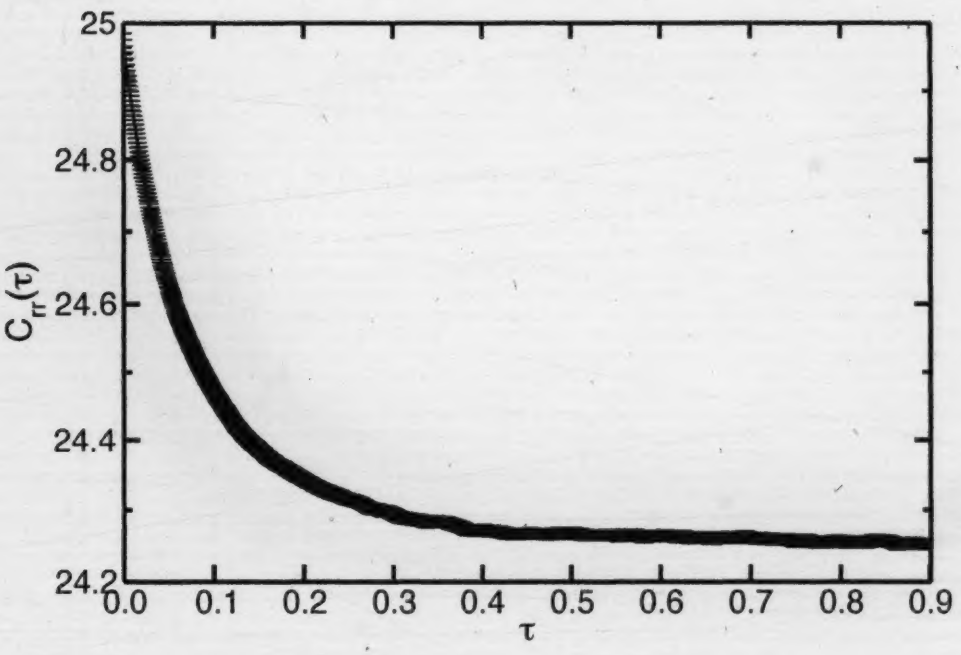

Figure 5.1: Average pair distance imaginary-time autocorrelation function of $(para\mathrm{H}_2)_3$.

portion of the path where the trial wavefunction has already converged to the ground state. In this way, the bias introduced by the trial wavefunction is eliminated.

In order to obtain the first excited state, we analyse the long time tail of this function. To do so, we first re-write the correlation function as,

$$-\ln\left[\langle\hat{A}(0)\hat{A}(\tau)\rangle - |\langle 0|\hat{A}|0\rangle|^2\right]/\tau + E_0 = E_1 - \ln\left[|\langle 0|\hat{A}|1\rangle|^2\right]/\tau \qquad (5.10)$$

In Eq. 5.10 we have assumed that only the first excited state contributes to the tail of the wavefunction. We do a linear least square fit on the early part of data. The earliest part of the data is plagued with large statistical errors and is neglected in the fitting procedure. This result is shown in Fig. 5.2. The fit (correlation coefficient $r = 0.9931$) yields an intercept of -4.6 K. This is the lowest lying excited state. When comparing to the result of Table 5.1, we see that we can catch this excited state with an error of 2%. We can also obtain the matrix element, 0.49, with an error of 8%. These results show that it is in principle possible to extract excited states using a ITCF calculated from a PIGS simulation. However, it is worth noting, that the above example is probably the most tractable application, since $(para\mathrm{H}_2)_3$ only has two bound states. Preliminary results (not shown) indicate that the situation is more difficult for systems with more bound states. While the method needs refinement, it is promising and further developments are in progress.

5.3.1 Reaction rates

In the previous Chapter we studied the ground state properties of a weakly bound cluster, the $ortho\mathrm{D}_2$ trimer, embedded in hydrogen clusters of different sizes. One of the main findings of that work was that the hydrogen environment has an effect on the structure of the trimer subsystem. Moreover, in some particular clusters, two distinct configurations of the trimer coexist. To study this phenomenon in more depth, we have chosen to focus on the $(ortho\mathrm{D}_2)_3(para\mathrm{H}_2)_8$ cluster. In Fig. 5.3 we show the Pekeris distribution function of the trimer subsystem, along with the three bound states of the deuterium trimer, represented in terms of their Pekeris distributions. We observe that when $(ortho\mathrm{D}_2)_3$ is placed inside the $(para\mathrm{H}_2)_8$ cluster, its ground

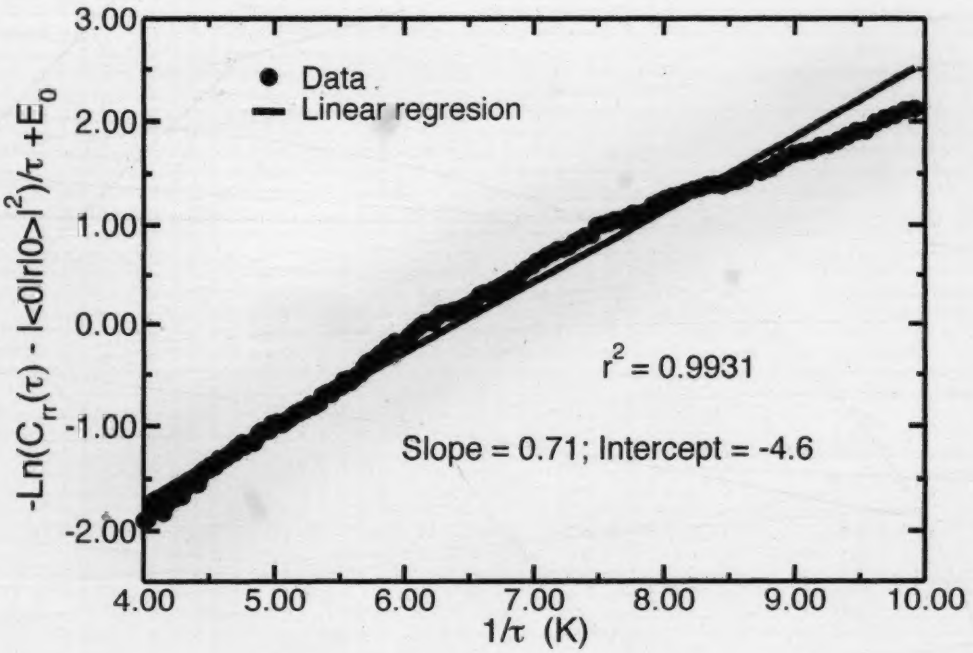

Figure 5.2: Linearization of the long time tail of the imaginary-time correlation function. Statistical errors of the data are within the size of the symbol

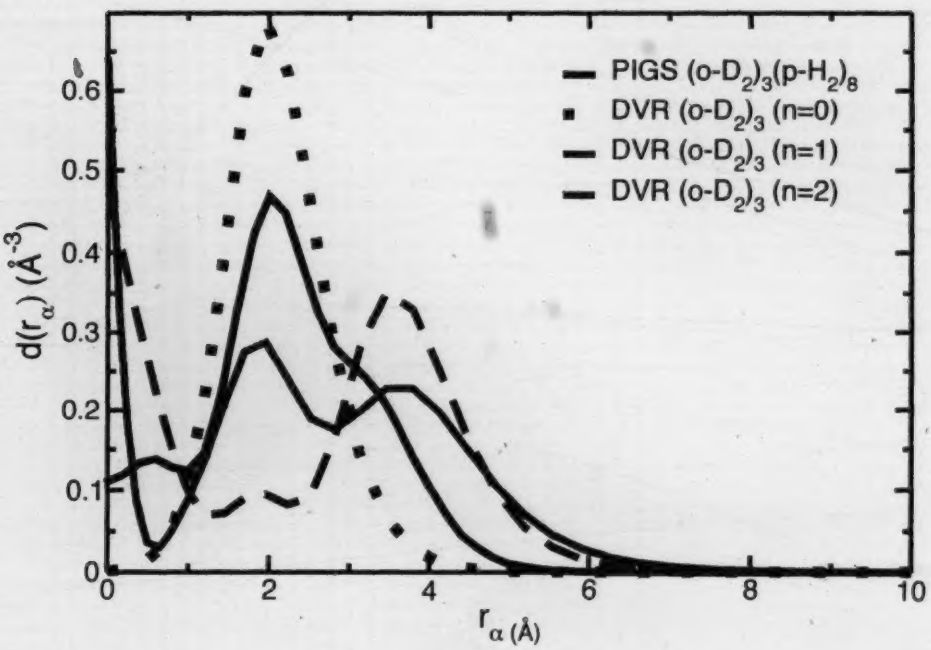

Figure 5.3: Pekeris distribution functions of $(ortho\mathrm{D}_2)_3(para\mathrm{H}_2)_8$ (PIGS) and the bound states of $(ortho\mathrm{D}_2)_3$ (DVR).

state develops characteristics of the excited states of the pure trimer. In particular, the non-zero value at $r_\alpha = 0$ and the shoulder that develops at ≈ 3.4 Å are features that are unique to the excited states. This result can be interpreted in the following way: the hydrogen is able to stabilize to some degree the excited states of the trimer. This extra stabilization allows the trimer to explore more configurations. In some cases the "residence time" in these configurations is such that it leads to coexistence between higher energy structures and the more stable equilateral triangle one. To gain further insight into this behaviour, we calculated the negative of the natural logarithm of the distribution function of the asymmetry factor $w(q)$. This quantity has been defined and used in Chapter 4 and serves as suitable reaction coordinate for the isomerization reaction of the deuterium trimer. We refer back to Fig. 4.6 (a) where $w(q)$ for $(ortho\mathrm{D}_2)_3(para\mathrm{H}_2)_8$ is shown . In this particular case, the asymmetry factor reveals a double well and the separation between reactants and products is therefore well defined. This separation facilitates the use of the side-side ITCF to study this process. In this particular case we placed the dividing surface at $q = 3.0$ Å. Then the Heaviside function is defined as $h(q) = 1$, if $q \geq 3.0$ and zero otherwise. This means that we are considering the reaction from left to right as the forward reaction. We show this correlation function in Fig. 5.4.

In this work, we limit ourselves to analyse the results of the imaginary-time dynamics in terms of the quantum rate theory developed by Miller and coworkers [144, 145]. The finite temperature path integral implementation of this theory relies on the analytic continuation of the ITCF [146]. In the ground state however, the implementation of this methodology is difficult. We opt for the imaginary time analysis of the signal here. Following Miller's ideas, one can obtain the "imaginary-time" rate constant of the isomerization process as the integral of the flux-flux ITCF (Eq. 5.6). This can be obtained as the derivative of the side-side ITC. We calculate this quantity using numerical differentiation and integration of the data. This procedure yields a value of $\tilde{k} = -0.089011$. We first notice the negative sign. This means that the backward reaction, towards equilateral configurations, is favoured. This result is consistent with the shape of the $w(q)$ function shown in Fig. 4.6 (a) where reactants are clearly

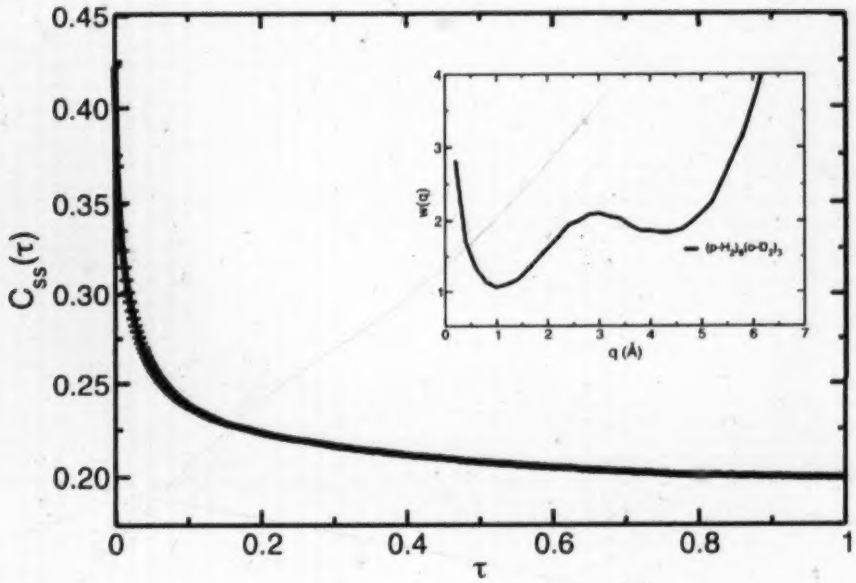

Figure 5.4: Side-Side imaginary-time correlation function along the asymmetry factor of $(ortho\mathrm{D}_2)_3(para\mathrm{H}_2)_8$.

favoured due to their higher statistical weight. At this point this result is preliminary but encouraging.

5.4 Conclusions

In this Chapter we have calculated imaginary-time correlation functions using the PIGS method. Our methodology is, in principle, exact and avoids the inclusion of bias from the trial wavefunction. This is achieved by calculating the correlation function in a region of the path where the ground state has already been reached. Using the average pair distance ITCF, we attempted to extract the first excited state (totally symmetric, J=0) of the $(para\mathrm{H}_2)_3$ trimer. Our results in this regard are modest. We obtained both the lowest energy level and the matrix element with an accuracy of 10% when compared to exact diagonalization results. We also studied the mixed $(ortho\mathrm{D}_2)_3(para\mathrm{H}_2)_8$ cluster. We explained the observed relatively floppy nature of the deuterium subsystem compared to the pure counterpart in terms of partial stabilization of excited states of the trimer by the surrounding hydrogen molecules. Finally, we analysed the side-side imaginary time correlation function using the equilateral asymmetry factor as reaction coordinate. We obtained the imaginary-time rate constant and its value suggests that a reaction towards equilateral configurations is favoured. The results presented in this Chapter are preliminary attempts to study the dynamical behaviour of quantum clusters in their ground state.

Chapter 6

Conclusions

The behaviour of a system that is composed of a small number of particles is different from that of bulk matter. The differences are due to the importance of surface effects and fluctuations in the determination of the physical properties of the system. If quantum effects are included to the picture, intriguing phenomena, such as superfluidity, can be observed. The last decade has witnessed a rising interest in understanding the behaviour of finite size systems composed of particles governed by the laws of quantum mechanics. Over this period of time, a great wealth of knowledge about the physics of quantum clusters has been accumulated. The contributions of many researchers, including ours, have helped to draw a clearer picture of these interesting systems. In Chapter 1, we presented a survey of the most recent research endeavours aimed at getting a better understanding of the physical properties and applications of quantum clusters, and pointed out some of the current outstanding questions. We also described the theoretical framework of the research presented in this thesis: the path integral ground state method.

In the following lines we conclude by summarizing the *original contributions* made by the authors of this work. In Chapter 2, we presented the results of the first accurate systematic study of the ground state energetic and structural properties of the smallest ($N \leq 20$) hydrogen clusters [44]. The relevance of this work rests on the fact that it bridged the gap in the existent literature concerning these systems. Almost simultaneously, a similar work was published by Guardiola *et al.* [45]. The authors used a DMC methodology to study clusters of up to $N = 50$ molecules; the

results of that work showed consistently higher ground state energies compared to our benchmark study. In a follow up work by the same authors [48], the calculated DMC energies agreed much better with ours, however, at the expense of introducing a three-body term in the DMC trial wavefunction. From the results of all these studies, a fair amount of new insight regarding these systems was acquired and further questions were raised. In particular, the solid- or liquid-like nature of these systems remained unclear.

We addressed the above question in Chapter 3. The results described in this chapter showed that the fine details, i.e. magic numbers, of the energetics of $(para\mathrm{H}_2)_N$ are sensitive to the interaction potential used to describe the system. This is a result that is far from obvious. More importantly, we found that in the ground state, $para\mathrm{H}_2$ clusters are mostly liquid-like. Some degree of rigidity appears at $N \geq 26$, revealing the possibility that a liquid and a more rigid phase could coexist beyond $N = 26$. The most rigid hydrogen clusters were found in the N=41-45 size range. On the other hand, $ortho\mathrm{D}_2$ clusters with N=13 and $N \geq 19$ are rigid, whereas the rest of the small ones are liquid. To arrive at these conclusions, we made use of the Lindemann melting criterion and introduced the difference between specific and generic distance fluctuations as a complementary measure of rigidity. The assessment of orientational order was rather elusive, and we were unable to draw definite conclusions in this regard. However, based on the density profiles, we inferred that an anti-Mackay layering is the predominant structure in clusters in the $19 \leq N < 41$ size range. The structures of the rest of the clusters are thought to be consistent with a Mackay structure, except for $N = 38$ that can be octahedral.

In Chapter 4 we studied the structure of the deuterium trimer embedded in hydrogen clusters. We observed that the heavy isotope is segregated to the interior of the cluster. At small cluster size ($N \leq 22$), the $para\mathrm{H}_2$ provides a quantum delocalized environment for the dopant. Larger clusters display a localized anti-Mackay icosahedral core and a delocalized surface. The main finding of this chapter was that different environments have different effects on the structure of the $(ortho\mathrm{D}_2)_3$ trimer. For clusters made of $N = 8 - 19$ hydrogens, the deuterium trimer is a floppy

system, capable of exploring different structures including linear and in particular non-equilateral configurations. On the other hand, from $N = 20 - 40$ the environment "locks" the trimer in an equilateral configuration. The exception of this behaviour was found at $N = 23, 34$. These clusters display a deuterium trimer that prefers an isosceles configuration, although the system is able to explore equilateral configurations. This is a behaviour completely induced by the environment, with a dynamics dominated by tunnelling.

Finally, in Chapter 5, we presented our modest attempts to study the dynamical properties of quantum clusters. We calculated imaginary-time correlation functions using the PIGS method. The proposed methodology is numerically exact, and does not introduce any bias from the trial wavefunction. Our preliminary results are encouraging. Using a very simple methodology, we were able to calculate the energy of the first totally symmetric excited level and the corresponding matrix element for the hydrogen trimer to an accuracy of 10%. We also took a deeper look at one of the clusters studied in the preceding Chapter. The Pekeris distributions for the excited states of the pure deuterium trimer revealed that excited states are partially stabilized by the hydrogen environment.

6.1 Future Directions

We draw this thesis to a close by suggesting two systems that not only are amenable to a PIGS treatment, but also pose interesting scientific questions.

6.1.1 Mixed Helium-Hydrogen Clusters

The next system that we propose to study is mixed Helium-Hydrogen clusters. This can be considered an extension of our previous studies of Hydrogen-Deuterium clusters. It has been observed [147, 112, 29, 148, 149, 150] that in clusters made of binary isotopic mixtures, the heavier isotope is more likely to be found in the interior of the system. Similarly, in quantum clusters of helium atoms or hydrogen molecules doped with a single heavy (classical) impurity, such as alkali metal atoms, the position of

the dopant depends on the strength of the impurity-environment interaction [151]. If the impurity-environment interaction is weaker than the one between molecules in the pure cluster, the impurity is located at the surface, otherwise it is located close to the centre.

The above observation is not necessarily the case when both components are quantum particles of different masses, along with different interaction strengths. In this case, these two effects compete. In the particular situation of a single hydrogen molecule impurity in a helium cluster, the mass effect is predominant. The hydrogen molecule is delocalized in the cluster [152, 153, 154, 155]. However, if more than one hydrogen molecules are mixed with a helium cluster, a hydrogen molecule, albeit lighter than helium, tends to be located in the interior of the clusters [156].

In the only theoretical study of mixtures of several hydrogen molecules in Helium clusters [156], the authors concluded that at finite temperature, the hydrogen molecules form subclusters inside the helium matrix. The structure of these subsystems was found to be the same as the one observed in their isolated counterpart. This conclusion was drawn based on a rather simplistic inspection of the density profiles of the systems under consideration. We have found [150] that in the case of a deuterium trimer embedded in a hydrogen cluster, the quantum environment has indeed an effect on the structure of the deuterium subsystem. These effects are subtle and an analysis based solely on the density profile of the system has proven to be insufficient to fully characterized similar systems [44, 49, 150]. Therefore, a more complete study of Helium-Hydrogen clusters can potentially reveal unknown structural features and interesting dynamical behaviour.

In this regard we have made modest advances. Preliminary studies show that to calculate accurate ground state energies using PIGS, a trial wavefunction with the correct long-distance behaviour is needed. To reiterate, thus far most of our studies have used a trial wavefunction typical for bulk matter. The robustness of the PIGS method has allowed us to accurately compute the ground state properties of all clusters independent of the trial wavefunction. However, in the particular case of Helium clusters, the very weak interaction between Helium atoms have the undesirable

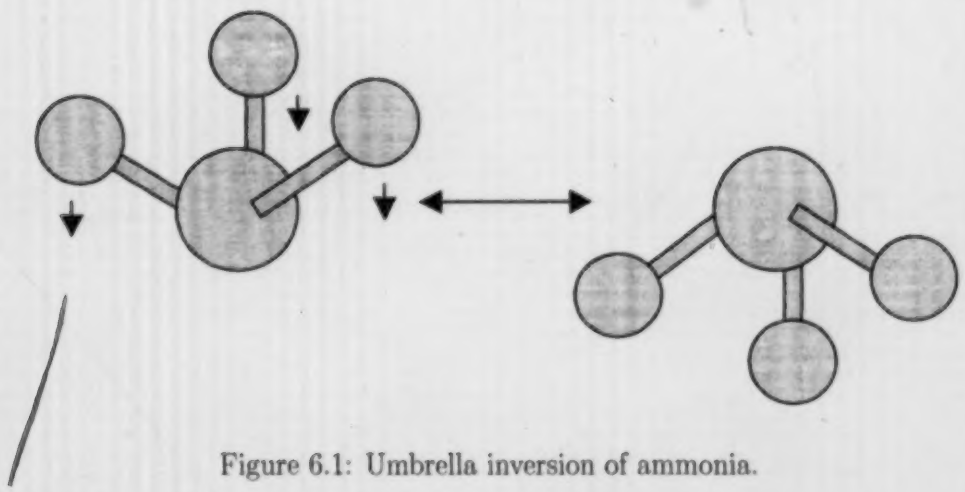

Figure 6.1: Umbrella inversion of ammonia.

effect that small clusters tend to "evaporate" during the simulation. Therefore, confining potentials are needed to hold the cluster together. This problem is particularly important at finite temperature [156]. On the other hand, in the ground state, the use of a square integrable trial wavefunction is sufficient to avoid "evaporation" making the use of confining potentials unnecessary. To our knowledge, no account has been given of the ground state properties of these systems, namely, several hydrogen molecules embedded in helium clusters.

6.1.2 Ammonia embedded in Helium clusters

The motivations behind the proposal of studying this second system are of experimental character. It has been observed that the rotational spectrum of ammonia embedded in helium nanodroplets has very interesting features [157, 158, 159]. The umbrella mode of ammonia (depicted in Fig. 6.1) is affected in a non-trivial way by the Helium environment. This perturbation leads to two distinct effects: a blueshift (when compared to the free ammonia) [157, 158] and a rather peculiar line shape for the spectrum [159], both concerning the vibrational mode that corresponds to the umbrella tunnelling transition. The first of these two observations has been studied from the theoretical point of view in a recent work by Viel *et al.* [143]. In this

work, the authors qualitatively reproduced the experimental observations, namely the aforementioned blueshift and the reduction of the tunnelling splitting in the ground and first vibrational excited states of the molecule. The methodology used in that study was DMC for the ground state calculation and POITSE [141, 142] to compute the tunnelling splitting.

Thus far, theoretical efforts have not been able to fully explain the peculiar shape of the observed spectrum. Additionally, the tunnelling rate of the umbrella inversion has not yet been characterized. These pose interesting challenges for the development of new methodologies related to the work of this thesis.

Bibliography

[1] J. Scoles, D. Bassi, U. Buck, and D. Lainé, *Atomic and Molecular Beam Methods* (Oxford University Press, Oxford, 1988).

[2] N. Halberstadt and K. C. Janda, *Dynamics of Polyatomics van der Waals Complexes* (Plenum, New York, 1990).

[3] A. Proykova and R. S. Berry, J. Phys. B **39**, R167 (2006).

[4] T. A. Weber and F. H. Stillinger, J. Chem. Phys. **81**, 5089 (1984).

[5] A. Proykova, R. S. Berry, and I. P. Daykov, Second- and first-order phase transitions in molecular clusters, in *Adventures in Chemical Physics: A Special Volume in Advances in Chemical Physics, Vol. 132*, edited by R. S. Berry and J. J. S. editor S. A. Rice, page 131, John Wiley and Sons Inc., 2006.

[6] A. L. Mackay, Acta Crystallographica **15**, 916 (1962).

[7] K. H. Kuo, Structural Chemistry **13**, 221 (2002).

[8] J. P. K. Doye, D. J. Wales, and R. S. Berry, J. Chem. Phys. **103**, 4234 (1995).

[9] J. P. K. Doye and D. J. Wales, Chem. Phys. Lett. **247**, 339 (1995).

[10] D. M. Deaven, N. Tit, J. R. Morris, and K. M. Ho, Chem. Phys. Lett. **256**, 195 (1996).

[11] M. R. Hoare and P. Pal, Nature **230**, 5 (1971).

[12] M. R. Hoare and P. Pal, Nature **236**, 35 (1972).

[13] D. L. Freeman and J. D. Doll, J. Chem. Phys. **82**, 462 (1985).

[14] R. H. Leary and J. P. K. Doye, Phys. Rev. E **60**, R6320 (1999).

[15] J. A. Northby, **99**, 6166.

[16] D. J. Wales and J. P. K. Doye, J. Phys. Chem. A **101**, 5111 (1997).

[17] P. A. Frantsuzov and V. A. Mandelshtam, Phys. Rev. E **72**, 037102 (2005).

[18] P. A. Frantsuzov, D. Meluzzi, and V. A. Mandelshtam, Phys. Rev. Lett. **96**, 113401 (2006).

[19] V. A. Mandelshtam and P. A. Frantsuzov, J. Chem. Phys. **124**, 204511 (2006).

[20] L. Tisza, Nature **141**, 913 (1938).

[21] L. Landau, J. Phys. U. S. S. R. **5**, 185 (1941).

[22] E. L. Andronikashivili, J. Phys. U. S. S. R. **10**, 201 (1946).

[23] V. L. Ginsburg and A. A. Sobyanin, JETPLetters **15**, 343 (1972).

[24] P. Sindzingre, M. L. Klein, and D. M. Ceperly, Phys. Rev. Lett. **63**, 1601 (1989).

[25] P. Sindzingre, D. M. Ceperley, and M. L. Klein, Phys. Rev. Lett. **67**, 1871 (1991).

[26] M. V. R. Krishna and K. B. Whaley, Z. Phys. D **20**, 223 (1991).

[27] D. Scharf, M. L. Klein, and G. Martyna, J. Chem. Phys. **97**, 3590 (1992).

[28] M. A. McMahon, R. B. Barnett, and K. B. Whaley, J. Chem. Phys. **99**, 8616 (1993).

[29] C. Chakravarty, Molecular Physics **84**, 845 (1995).

[30] D. M. Ceperley, Rev. Mod. Phys. **67**, 279 (1995).

[31] M. H. Kalos, Phys. Rev. **128**, 1791 (1962).

[32] S. Grenbenev, J. P. Toennies, and A. F. Vilesov, Science **279**, 2083 (1998).

[33] J. Tang, Y. Xu, A. R. W. McKellar, and W. Jäger, Science **297**, 2030 (2002).

[34] S. Grbenev, B. Sartakov, J. P. Toennies, and A. F. Vilesov, Science **289**, 1532 (2000).

[35] J. P. Toennies and A. F. Vilesov, Annu. Rev. Phys. Chem. **49**, 1 (1998).

[36] Y. K. Kwon and K. B. Whaley, Phys. Rev. Lett. **89**, 4108 (1999).

[37] Y. Kwon and K. B. Whaley, Phys. Rev. Lett. **89**, 273401 (2002).

[38] S. Baroni and S. Moroni, ChemPhysChem **6**, 1884 (2005).

[39] Y. Kwon and K. B. Whaley, J. Low Temp. Phys. **134**, 269 (2004).

[40] S. Moroni, N. Blinov, and P.-N. Roy, J. Chem. Phys. **121**, 3577 (2004).

[41] S. Miura, J. Chem. Phys. **126**, 114308 (2007).

[42] S. Miura, J. Chem. Phys. **126**, 114309 (2007).

[43] E. Sola, J. Casulleras, and J. Boronat, J. Low Temp. Phys. **134**, 787 (2004).

[44] J. E. Cuervo and P.-N. Roy, J. Chem. Phys. **125**, 124314 (2006).

[45] R. Guardiola and J. Navarro, Phys. Rev. A **74**, 025201 (2006).

[46] R. Guardiola, O. Kornilov, J. Navarro, and J. P. Toennies, J. Chem. Phys. **124**, 084307 (2006).

[47] R. Guardiola and J. Navarro, Cent. Eur. J. Phys **6**, 33 (2008).

[48] R. Guardiola and J. Navarro, J. Chem. Phys. **128**, 144303 (2008).

[49] J. E. Cuervo and P.-N. Roy, J. Chem. Phys. **128**, 224509 (2008).

[50] S. A. Khairallah, M. B. Sevryuk, D. M. Ceperley, and J. P. Toennies, Phys. Rev. Lett. **98**, 183401 (2007).

[51] F. Mezzacapo and M. Boninsegni, Phys. Rev. Lett. **97**, 045301 (2006).

[52] F. Mezzacapo and M. Boninsegni, Phys. Rev. A **75**, 033201 (2007).

[53] F. Mezzacapo and M. Boninsegni, Phys. Rev. A **76**, 021201 (2007).

[54] F. Mezzacapo and M. Boninsegni, Phys. Rev. Lett. **100**, 145301 (2008).

[55] G. Tejeda, J. M. Fernández, S. Montero, D. Blume, and J. P. Toennies, Phys. Rev. Lett. **92**, 223401 (2004).

[56] A. Sarsa, K. E. Schmidt, and W. R. Magro, J. Chem. Phys. **113**, 1366 (2000).

[57] J. E. Cuervo, P.-N. Roy, and M. Boninsegni, J. Chem. Phys. **122**, 114504 (2005).

[58] M. Born and R. Oppenheimer, Ann. Phys. (Berlin) **84**, 457 (1927).

[59] R. P. Feynman, *Statistical Mechanics: A Set of Lectures* (Addison-Wesley, 1992).

[60] M. Takahashi and M. Imada, J. Phys. Soc. Jpn. **53**, 3765 (1984).

[61] X. P. Li and J. Q. Broughthon, J. Chem. Phys. **86**, 5094 (1987).

[62] H. A. Forbert and S. A. Chin, Phys. Rev. B **63**, 144518 (2001).

[63] O. Ciftja and S. A. Chin, Phys. Rev. B **68**, 134510 (2003).

[64] S. Chiesa, M. Mella, G. Morosi, and D. Bressanini, J. Chem. Phys. **119**, 5601 (2003).

[65] J. B. Anderson, J. Chem. Phys. **63**, 1499 (1975).

[66] P. J. Reynolds, D. M. Ceperley, B. J. Alder, and W. A. Lester, J. Chem. Phys. **77**, 5593 (1982).

[67] C. J. Umrigar, M. P. Nightingale, and K. J. Runge, J. Chem. Phys. **99**, 2865 (1993).

[68] M. A. McMahon and K. B. Whaley, Chem. Phys. **182**, 119 (1994).

[69] S. Baroni and S. Moroni, Phys. Rev. Lett. **82**, 4745 (1999).

[70] M. Carmichael, K. Chenoweth, and C. E. Dykstra, J. Chem. Phys. **108** (2004).

[71] F. A. Gianturco, T. González-Lezana, G. Delgado-Barrio, and P. Villareal, J. Chem. Phys. **122**, 084308 (2005).

[72] J. D. Turnbull and M. Boninsegni, J. Low Temp. Phys. **140**, 269 (2005).

[73] J. D. Turnbull and M. Boninsegni, Phys. Rev. B **71**, 205421 (2005).

[74] R. J. Hinde, Chem. Phys. Lett. **4**, 418 (2006).

[75] I. F. Silvera and V. Goldman, J. Chem. Phys. **69**, 4209 (1978).

[76] U. Buck, F. Huisken, A. Kohlhase, D. Otten, and J. Schaefer, J. Chem. Phys. **78**, 4439 (1983).

[77] L. Brualla, K. Sakkos, J. Boronat, and J. Casurellas, J. Chem. Phys. **121**, 636 (2004).

[78] S. Jang, S. Jang, and G. A. Voth, J. Chem. Phys. **115**, 7832 (2001).

[79] J. C. Light, I. P. Hamilton, and J. V. Lill, J. Chem. Phys. **82**, 1400 (1985).

[80] J. Light and J. T. Carrington, Adv. Chem. Phys. **114**, 263 (2000).

[81] D. T. Colbert and W. H. Miller, J. Chem. Phys. **96**, 1982 (1991).

[82] P.-N. Roy, J. Chem. Phys. **119**, 5437 (2003).

[83] Y. D. Liu and P.-N. Roy, J. Chem. Phys. **121**, 6282 (2004).

[84] M. P. Nightingale and P.-N. Roy, J. Phys. Chem. A **110**, 5391 (2006).

[85] C. L. Pekeris, Phys. Rev. A. **74**, 1649 (1958).

[86] E. R. Davidson, J. Am. Chem. Soc. **99**, 397 (1977).

[87] E. Rabani and J. Jortner, J. Phys. Chem. B **110**, 18893 (2006).

[88] C. Chakravarty, J. Chem. Phys. **116**, 8938 (2002).

[89] S.-N. Luo, A. Strachan, and D. C. Swift, J. Chem. Phys. **122**, 194709 (2005).

[90] C. Chakravarty, P. G. Debenedetti, and F. H. Stillinger, J. Chem. Phys. **126**, 204508 (2007).

[91] P. J. Steinhardt, D. R. Nelson, and M. Ronchetti, Phys. Rev. B **28**, 784 (1983).

[92] Y. T. Wang, S. Teitel, and C. Dellago, J. Chem. Phys. **122**, 214722 (2005).

[93] D. Blume, Private communication.

[94] J. Farges, M. F. D. Feraudy, B. Raoult, and G. Torchet, Surface Science **156**, 370 (1985).

[95] F. Sebastianelli, Y. S. Elmatad, H. Jiang, and Z. Bacic, J. Chem. Phys. **125**, 164313 (2006).

[96] F. A. Lindemann, Phys. Z. **11**, 609 (1910).

[97] L. Zhan, J. Z. Y. Chen, and W.-K. Liu, J. Chem. Phys. **127**, 141101 (2007).

[98] S. Paolini, F. Ancilotto, and F. Toigo, J. Chem. Phys. **126**, 124317 (2007).

[99] S. Goyal, D. L. Schutt, , and G. Scoles, Phys. Rev. Lett. **69**, 933 (1992).

[100] C. Callegari, K. K. Lehmann, R. Schmied, and G. Scoles, J. Chem. Phys. **115**, 10090 (2001).

[101] J. P. Toennies and A. F. Vilesov, Angew. Chem. Int. Ed. **43**, 2622 (2004).

[102] M. Barranco et al., J. Low Temp. Phys. **142**, 1 (2006).

[103] M. Y. Choi et al., Int. Rev. Phys. Chem **25**, 15 (2006).

[104] K. Nauta and R. E. Miller, Science **287**, 293 (2000).

[105] K. Nauta and R. E. Miller, Science **283**, 1895 (1999).

[106] K. Szalewicz, Int. Rev. Phys. Chem. **27**, 273 (2008).

[107] H. Jiang, A. Sarsa, G. Murdachaew, K. Szalewiz, and Z. Bačić, J. Chem. Phys. **122**, 224313 (2005).

[108] D. T. Moore and R. E. Miller, J. Chem. Phys. **107**, 10805 (2003).

[109] J. Tang and A. R. W. McKellar, J. Chem. Phys. **121**, 3087 (2004).

[110] F. Paesani, R. E. Zillich, and K. B. Whaley, J. Chem. Phys. **119**, 11682 (2003).

[111] F. Paesani and K. B. Whaley, J. Chem. Phys. **124**, 234310 (2006).

[112] C. Chakravarty, Phys. Rev. Lett. **75**, 1727 (1995).

[113] C. L. Pekeris, Phys. Rev. **112**, 1649 (1958).

[114] W. Humphrey, A. Dalke, and K. Schulten, Journal of Molecular Graphics **14**, 33 (1996).

[115] R. Zwanzig, *Nonequilibrium Statistical Mechanics* (Oxford University Press, Oxford, 2001).

[116] F. Grossmann, Chem. Phys. Lett. **262**, 470 (1996).

[117] S. Garashchuk and D. Tannor, Chem. Phys. Lett. **262**, 470 (1996).

[118] W. H. Miller, Farad. Discuss. Chem. Soc. **110**, 1 (1998).

[119] B. Harland and P.-N. Roy, J. Chem. Phys. **118**, 4791 (2003).

[120] B. B. Issack and P.-N. Roy, J. Chem. Phys. **123**, 084103 (2005).

[121] B. B. Issack and P.-N. Roy, J. Chem. Phys. **126**, 024111 (2007).

[122] B. B. Issack and P.-N. Roy, J. Chem. Phys. **127**, 054105 (2007).

[123] J. Cao and G. A. Voth, J. Chem. Phys. **100**, 5106 (1994).

[124] S. Jang and G. A. Voth, J. Chem. Phys. **111**, 2357 (1999).

[125] S. Jang and G. A. Voth, J. Chem. Phys. **111**, 2371 (1999).

[126] I. R. Craig and D. E. Manolopoulos, J. Chem. Phys. **121**, 3368 (2004).

[127] G. Krilov and B. J. Berne, J. Chem. Phys. **111**, 9140 (1999).

[128] R. N. Silver, D. S. Sivia, and J. E. Gubernatis, Phys. Rev. B **41**, 2380 (1990).

[129] E. Gallicchio and B. J. Berne, J. Chem. Phys. **101**, 9909 (1994).

[130] G. Krilov and B. J. Berne, J. Chem. Phys. **111**, 9156 (1999).

[131] E. Rabani, D. R. Reichman, G. Krilov, and B. J. Berne, Proc. Natl. Acad. Sci. **99**, 1129 (2002).

[132] E. Rabani, G. Krilov, D. R. Reichman, and B. J. Berne, J. Chem. Phys. **123**, 184506 (2005).

[133] E. Rabani, G. Krilov, and B. J. Berne, J. Chem. Phys. **112**, 2605 (2000).

[134] E. Sim, G. Krilov, and B. J. Berne, J. Phys. Chem. A **105**, 2824 (2001).

[135] A. Golosov, D. R. Reichman, and E. Rabani, J. Chem. Phys. **118**, 457 (2003).

[136] D. M. Ceperley and B. Bernu, J. Chem. Phys. **89**, 6316 (1988).

[137] A. Lüchow et al., J. Phys. Chem. A **107**, 7175 (2003).

[138] D. Blume, M. Lewerenz, and K. B. Whaley, J. Chem. Phys. **107**, 9607 (1997).

[139] S. Moroni, A. Sarsa, S. Fantoni, K. E. Schmidt, and S. Baroni, Phys. Rev. Lett. **90**, 143401 (2003).

[140] T. Škrbić, S. Moroni, and S. Baroni, J. Phys. Chem. A **111**, 12749 (2007).

[141] D. Blume, M. Lewerenz, P. Niyaz, and K. B. Whaley, Phys. Rev. E **55**, 3664 (1997).

[142] D. Blume, M. Mladenović, M. Lewerenz, and K. B. Whaley, J. Chem. Phys. **110**, 5789 (1999).

[143] A. Viel, K. B. Whaley, and R. J. Wheatley, J. Chem. Phys. **127**, 194303 (2007).

[144] W. H. Miller, J. Chem. Phys. **61**, 1823 (1974).

[145] W. H. Miller, S. D. Schwartz, and J. W. Tromp, J. Chem. Phys. **79**, 4889 (1983).

[146] E. Rabani, J. D. Gezelter, and B. J. Berne, Phys. Rev. Lett. **82**, 3649 (1999).

[147] A. Belic, F. Dalfovo, S. Fantoni, and S. Stringari, Phys. Rev. B **49**, 15253 (1994).

[148] S. A. Chin and E. Krotscheck, Phys. Rev. B **52**, 10405 (1995).

[149] M. Barranco, M. Pi, M. Gatica, E. S. Hernandez, and J. Navarro, Phys. Rev. E **56**, 8997 (1997).

[150] J. E. Cuervo and P.-N. Roy, J. Chem. Phys. , Submitted (2008).

[151] D. Scharf, M. L. Klein, and G. Martyna, J. Chem. Phys. **99**, 8997 (1993).

[152] R. N. Barnett and K. B. Whaley, J. Chem. Phys. **96**, 2953 (1992).

[153] R. N. Barnett and K. B. Whaley, Phys. Rev. A **47**, 4082 (1993).

[154] R. N. Barnett and K. B. Whaley, Z. Phys. D. **31**, 1994 (1994).

[155] Y. Kwon, D. M. Ceperley, and K. B. Whaley, J. Chem. Phys. **104**, 2341 (1995).

[156] M. C. Gordillo, Phys. Rev. B **60**, 6790 (1999).

[157] M. Behrens et al., J. Chem. Phys. **109**, 5914 (1998).

[158] M. N. Slipchenko and A. F. VIlesov, Chem. Phys. Lett. **412**, 176 (2005).

[159] R. Lehnig, N. Blinov, and W. Jäger, J. Chem. Phys. **127**, 241101 (2007).